Strain hardening relief and crack initiation delay of Ni-based superalloy Inconel 718 induced by high-density pulsed electric current

Department of Micro-Nano Mechanical Science and Engineering

Nagoya University

Shaojie GU

2022.03

Contents

Chapter 1 Introduction

1.1 Metal forming and formability enhancement by electric current

1.1.1 Metal forming and strain hardening

Metal forming is the metalworking process of components through plastic deformation induced by external forces and stresses exceeding the yield stress of the materials, which is also the so-called deformation process. Typically, the forming processes include stamping, rolling, drawing, extrusion, forging, etc. Since the material is rearranged to produce the shape, instead of cutting away the unwanted regions, the amount of waste can be substantially reduced. However, the formed pieces tend to possess high strength but low ductility, the so-called strain hardening, which requires the high forming forces and weakens the life of equipment and molds.

Moreover, in terms of the temperature during forming, the metal forming is divided into two groups: hot forming and cold forming [1,2]. The hot forming is a temperature-dependent process, as listed in Table 1-1, including forming temperature above the recrystallization temperature and less than the recrystallization temperature.

Table 1-1 Types of metalworking processes regarding the forming temperatures [2].

Category	Temperature	Merits	Drawbacks
Hot forming	Over T_R* ($0.7T_M$* < T < $0.8T_M$)	Soften the strength Enhance the ductility No work-hardening	High investment in equipment Poor surface finish Safety management
	Less than T_R ($0.3\ T_M$ < T < $0.5T_M$)	Partial work-hardening	
Cold forming	Room temperature or less than $0.3\ T_M$	Work-hardening Good finished surfaces High size precision	High forming force

* T_R= recrystallization temperature T_M= melting temperature

During the process at the forming temperature above the recrystallization temperature, the dynamic recrystallization and grain recovery occurred, and hence the

strain hardening has been suppressed. The partial strain hardening remained for the forming temperature less than recrystallization temperature. The relief of strain-hardening during hot forming helps the materials being shaped easily. The challenge is that the use of high temperatures and molten products requires vast furnaces, and an enormous investment is needed to buy the machinery. Most metals experience surface oxidation at elevated temperatures, resulting in a poor surface finish.

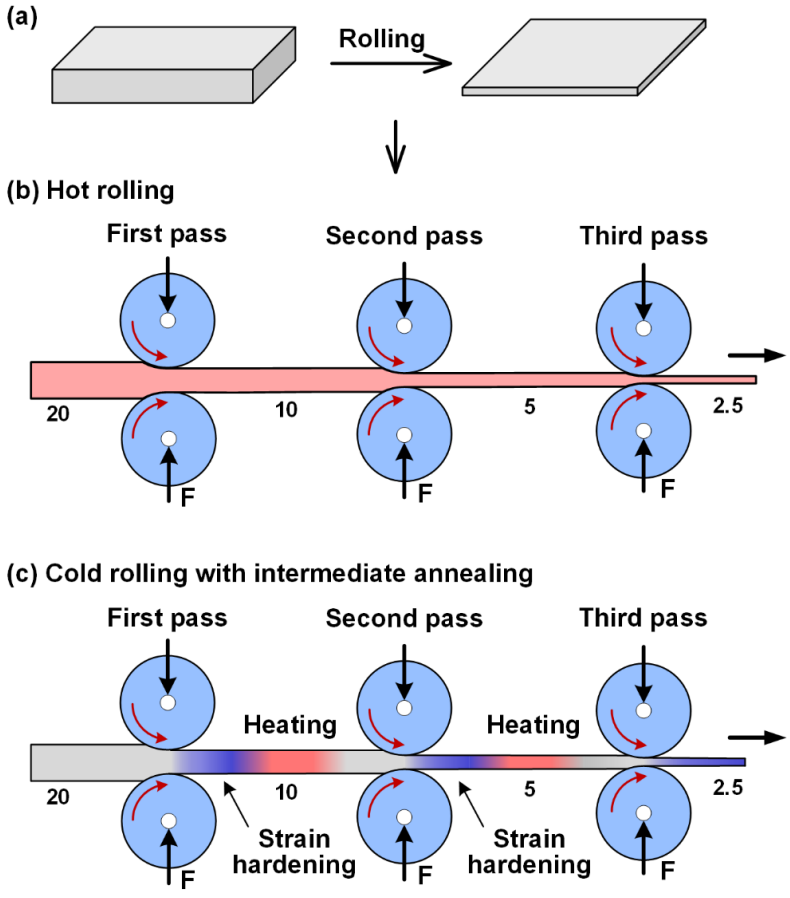

Fig. 1-1 Schematic diagram of multi-step forming. (a) Bulk material rolled to a thin plate, (b) hot rolling, and (c) cold rolling with intermediate annealing.

In contrast, cold forming usually results in better, more attractive finished surfaces with closer tolerances. In addition, cold-formed metals can be stronger than hot-formed metals due to strain hardening. For this reason, cold forming requires greater force and easily causes the failure of molds. Hence, only the materials with good

ductility, such as low carbon steels, austenitic stainless steels, pure titanium, some aluminum alloys, copper alloys, and Inconel alloys, can be cold-formed [2].

For severe deformation cases, multi-step forming is usually used. Fig. 1-1 shows the multi-step rolling from bulk material to a thin plate. For the case of hot forming, due to the good ductility at high temperature, the process can be smoothly performed. For the case of cold forming, intermediate annealing is commonly performed during the processing of a piece to restore the ductility lost through repeat working [1]. After intermediate annealing, the ductility of the work-hardened components is recovered, and it can be formed further without breaking.

Although hot forming and cold forming with intermediate annealing have been enhanced the formability of materials by removing the strain hardening, they also bring some critical problems, such as energy-inefficient, laborious, etc.

1.1.2 Formability enhancement by electric current

Since the 1960s, Troitskii [3–6] and Okazaki [7] and their coworkers have presented a flow stress drop phenomenon during deformation when applying the electric current through the materials. It was therefore termed as the “electroplastic effect” by the authors, and they attributed the electroplasticity to the impact of electrons on dislocations, which promotes the dislocation motion and enhances the ductility. Afterward, plenty of research has been conducted on the electroplasticity of numerous materials. Conrad and coworkers [8–25] found that the electroplasticity occurred in metals, ceramics as well as nanocrystalline materials after applying electric current or electric field. Other researches involving the formability of Al alloys [26–34], Ti alloys [35–43], Mg alloy [44–53], Cu alloys [54–57], and steels [58–60] by electric current were also carried out. Since the electric current is capable of softening the metals and enhancing the formability, this method is now utilized in the manufacturing field, known as the electrically-assisted (EA) forming, which is the

most promising technology with the merits of energy-efficient and short time [61]. The EA-forming involves forging, rolling, drawing, punching, etc., as shown in Fig. 1-2. For the EA-forging, the forgeability was significantly enhanced by electric current, and the overall force was highly decreased [62,63]. Regarding the EA-rolling, Xu et al. [64] and Lu et al. [65] found that the pressure was evidently reduced during rolling, and the deformation ability of the materials was highly enhanced. The EA-drawing was carried out on the materials such as stainless steel [66,67], copper [68], and cast-iron [69], and the results show that the drawing force was decreased and drawing speed was increased. Wang reported [70] that the magnesium alloy cups were successfully formed after applying an electric current due to the dynamic recrystallized grains occurred at a lower temperature, and the EA-punching showed a low energy consumption compared with conventional hot forming.

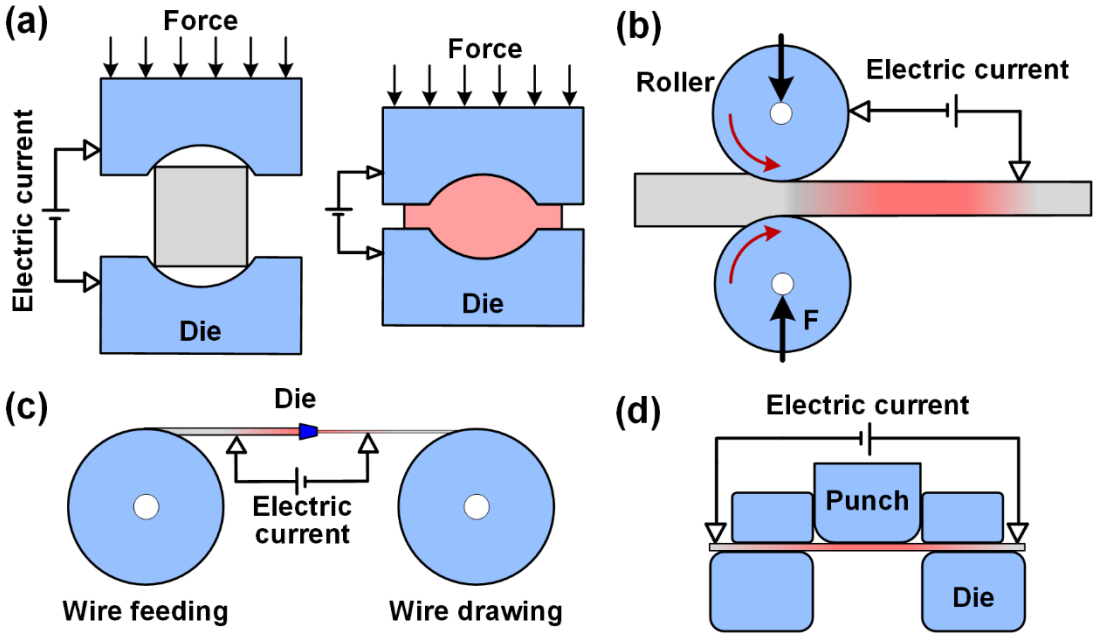

Fig. 1-2 Schematic diagrams of (a) EA-forging, (b) EA-rolling, (c) EA-drawing, and (d) EA-punching.

In brief, due to the efficient dislocation removing and rapid grain recovery, the strain hardening caused by forming was highly relieved by electric current treatment

[23–25,34,36–40,42–57,59,60,71–76]. Consequently, the forming force was decreased evidently, and the forming efficiency was significantly enhanced with a low cost. However, some issues regarding the strain-hardening relief induced by electric current treatment are still unclear. For example, all the studies have found that the microstructure evolution happened after electric current treatment. For example, the dislocation density was reduced, grain was refined, and grain orientation was modified. But still, how these microstructure evolutions affect strain hardening is rarely studied. In other words, the microstructure-mechanical properties relationship of the electric current treated samples was also unclear. Moreover, how the microstructure evolution (e.g., dislocation elimination and grain recovery) improved by the electric current is also seldom studied. Only a few studies found that the dislocation annihilation may be related to the combination of dipole dislocations and entanglement at grain boundaries (GBs) promoted by electric current. Additionally, the defect-free grains were formed after electric current treatment, but how the deformed grains recovered step by step is still not clear. Most importantly, the difference between electric current treatment and the traditional heat treatment in strain-hardening relief need to be clarified.

1.2 Fatigue fracture and fatigue life enhancement by electric current

1.2.1 Fatigue fracture

The fracture of engineered components and structures during fatigue load is a significant phenomenon in materials science. Even though the component or structure works within the safe load, fatigue damage can still occur, which is related to the intrinsic defects (e.g., porosity and impurity) or geometric discontinuity (e.g., joint, notch, and welding) in materials that causes the stress concentration near the defects or discontinuity and initiates the crack and finally causes the failure [77]. The crack initiation is associated with the plastic zone ahead of the defects or discontinuity,

where the dislocation multiplication and slip band are activated, and with the plastic accumulation, the slip bands in the plastic zone provide the site for crack initiation [78], as shown in Fig. 1-3. Actually, there are numerous microscopic cracks nucleated at the very beginning and then developed into one or several main cracks (crack initiation) after continuous fatigue load. Afterward, the primary cracks propagate and then lead to fracture of components. Hence, the fatigue life can be separated into two periods: the crack initiation and propagation period, respectively, as shown in Fig. 1-3, which can be denoted as the crack initiation life N_i and propagation life N_p.

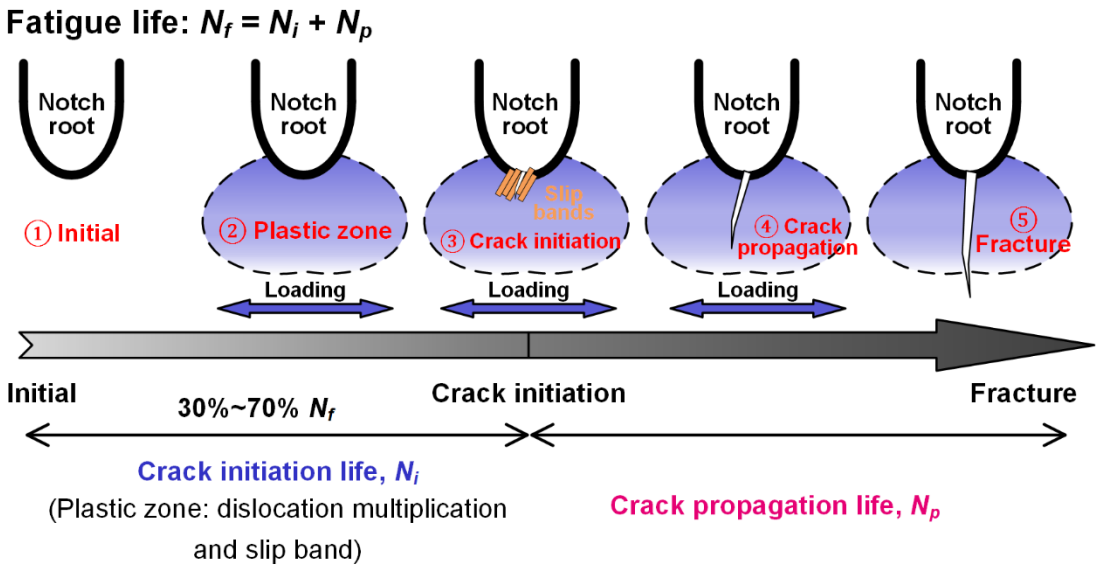

Fig. 1-3 Schematic diagram of fatigue life N_f of notched components with the definition of crack initiation life N_i and crack propagation life N_p.

For the proportion of these two periods, Nishitani et al. [79] found that the crack initiated (~10 μm) at approximately 20% of the fatigue life and the life of crack propagation from 10 μm to 1 mm occupied 70% in an annealed 0.45% C steel. Moreover, Motomichi et al. reported that the crack initiation life (several tens of μm) occupied approximately ~30% of the fatigue life in a Fe–C fully ferritic steel. Some researches were carried out to study the fatigue life of the weld joint, and the results show that the crack initiation life occupied a range from 40% to 70% [80,81].

Therefore, based on the above investigation, crack initiation life occupied approximately 30%-70% of the total fatigue life, which plays an equal role with the crack propagation life.

1.2.2 Fatigue life enhancement by electric current

During the previous several decades, many efforts have been carried out to prevent crack initiation and propagation of engineered materials by mechanical surface treatment, such as shot peening [82,83], laser shock peening [84,85], which introduce the beneficial compressive residual stresses onto the surface of materials. Although these methods are an effective way to improve fatigue life, they also have limitations for the irregular structures with notches or grooves, where the internal surfaces are difficult to treat.

In the last decade, the electric current method has been applied to enhance the fatigue life of metallic materials, and fruitful achievements have been obtained. However, almost all the studies are focused on the fatigue life enhancement in the crack propagation period, namely, aims to restore the crack by electric current treatment and realize the fatigue life enhancement [86–102]. As shown in Fig. 1-4, owing to the detour characteristics of electric flow near the crack, the current tends to concentrate near the crack and raise the local heating (or melting, bridging) and local compressive stress, thereby resulting in the crack closure and healing, as listed in Table 1-2. Although the crack initiation period (occupied 30%~70% of fatigue life) plays an equal role as the crack propagation period, as depicted before, the crack initiation life enhanced by an electric current is still seldom studied. Tang et al. [103,104] found that the residual strain, dislocation density, and micro-hardness within the plastic zone ahead of notch root were reduced by electric current in stainless steel SUS316, thereby realizing the delay of crack initiation. Despite Tang's pioneering work, many issues still need to be clarified. For example, how is the

plastic zone distributed near the notch root, and how does electric current affect the plastic zone? What is the relationship between the plastic zone and the current field? These issues still remain unclear.

Table 1-2 Fatigue life enhancement induced by electric current treatment.

Fatigue life enhancement by electric current treatment	
Crack initiation life N_i enhancement	**Crack propagation life N_p enhancement**
Mechanisms: Dislocation annihilation, slip bands recovery, and plastic deformation recovery. **(Rarely studied)**	**Mechanisms:** crack healing (local heating, melting, bridging, thermal stress, etc.) and dislocation annihilation. **(Well studied)**

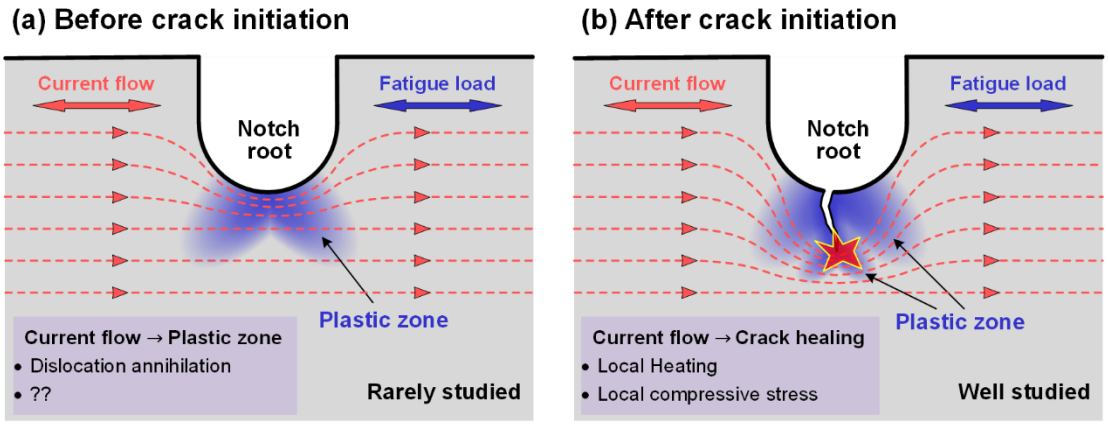

Fig. 1-4 Fatigue life enhancement by electric current treatment. (a) Before crack initiation, and (b) after crack initiation.

1.3 Thermal and athermal effects

Although extensive research regarding strain-hardening relief and fatigue life enhancement improved by electric current has been reported, it still controversies over the mechanisms of how the electric current promotes the microstructure evolution or what is the driving force for dislocation motion.

The previous studies proposed two primary views regarding the mechanisms of

driving force: thermal effect and athermal effect. Thereinto, the thermal effect is related to the Joule heating, while the athermal effect is mainly associated with electron wind force (EWF) due to the impact of electrons on atoms. Since the driven electrons collide with atoms during electric current flowing, the atomic thermal vibration of the treated sample is increased by momentum transfer (thermal effect), the so-called Joule heating, which is non-directional [105]. Firstly, the most significant effect of the thermal is to increase the thermal vibration of the atoms and soften the material. In other words, the thermal effect reduces the resistance force of dislocation motion. In addition, the other significant contribution is to improve dislocation motion (i.e., climb), which provides the driving force for microstructure evolution [106]. Since the dislocation climb is related to the atom or vacancy diffusion, dislocation movement is also non-directional. Moreover, the athermal effect is related to the conducted electrons colliding with the atoms and exerting a force on atoms, the so-called EWF. From the beginning of the discovery of the impact of electric current on materials properties, the mechanism of EWF on driving dislocation motion has received wide interest. Theoretical estimates of EWF on the dislocation motion can be divided into two general equations: (1) the equation concerning the dislocation resistivity [107] and (2) the other one based on quantum mechanics [108]. For details, please see Appendix 1.

Although a lot of research concerned the mechanisms of electric current on materials properties changes was carried out, the results obtained so far are mainly focused on the qualitative analysis, and their contributions are still unclear. Only a few studies have been conducted to evaluate the effect of thermal and athermal on the relief of strain hardening and plastic strain. Jiang et al. [46] studied the effect of electric current treatment on the microstructure change of the strain-hardened magnesium alloy, and the result indicates the athermal effect was the main reason that contributed to the rapid recrystallization. Xu et al. [47] also reported that the athermal effect is more dominant in recrystallization than the thermal effect. Hence, it is not

enough that only seldom studies examine the contributions of these two effects, and only qualitative conclusions are given. Moreover, some studies [109,110] simply add up all of the above effects arithmetically to investigate the effects of electric current treatment on the dislocation motion, regardless of their directions or effects. Hence, in this study, all the effects were considered and clarified.

Moreover, the previous research concluded that the recovery of strain hardening caused by the electric current treatment was attributed to the recrystallization, where the dislocation elimination and nucleation rate was highly promoted by the electric current treatment [23–25,34,36–40,42–57,59,60,71–76]. However, recrystallization is usually a slow process, and generally, it needs to heat the component to an elevated temperature and maintain a long time to realize the microstructure recovery by dislocation climb and the following nucleation and growth. In contrast, the electric current treatment is a more rapid and efficient method for grain recovery, which is different from the recrystallization caused by traditional heat treatment. The previous research has been tried to explain the microstructure healing caused by the electric current treatment via the theory of crystallization kinetic. But it is still unclear how the dislocation is eliminated and how the deformed grain is recovered caused by the electric current treatment. Thus, those issues should be elucidated.

1.4 Research objective

The above sections presented and summarized the research regarding the effect of the electric current treatment on strain-hardening relief and fatigue life enhancement, and also pointed out some potential problems or unclear issues that urgently need to be clarified. Hence, the research objectives of this thesis are presented below:

First of all, for solving the possible forming difficulties in the plastic processing field, this study aims to propose a low-cost and high-efficient method of high-density pulsed electric current (HDPEC) treatment as an alternative method of intermediate

annealing to relieve the strain hardening created by plastic deformation. A systematic and detailed investigation was carried out on the strain-hardening relief of pre-deformed Ni-based superalloy Inconel 718 (IN718) with various HDPEC treatment conditions. The mechanism of strain-hardening relief induced by HDPEC and the microstructure-mechanical properties relationships of HDPEC-treated pieces were clarified, which can guide us to choose suitable HDPEC parameters to modify the microstructure and alter the mechanical properties of strain-hardened pieces.

In addition, for clarifying the unclear issues regarding the microstructure evolution induced by HDPEC, this thesis aims to reveal the microstructure changes induced by HDPEC and figure out the effects of thermal and athermal on the microstructure evolution. The quasi-in-situ EBSD observation before and after HDPEC was carried out to investigate how the microstructure change, such as dislocation motion and GBs evolution. Furthermore, the contributions of thermal and athermal effects on strain-hardening relief by HDPEC treatment were quantitatively analyzed by several equivalent HDPEC-treated and rapidly heated samples. Most importantly, the difference between HDPEC treatment and traditional heat treatment in strain-hardening relief was revealed in this study.

Moreover, as mentioned before, almost all the studies regarding fatigue life focus on crack healing in the crack propagation period by the electric current treatment, and however, the effect of electric current on the plastic zone ahead of defects or discontinuity before crack initiation is still rarely studied. Hence, another research objective of this study is to heal the plastic zone or plastic deformation ahead of the notch before crack initiation and to examine the improvement of crack initiation life of notched samples utilizing HDPEC. Numerous fatigue tests under various HDPEC treatment conditions were conducted to investigate the enhancement of crack initiation life, and the microstructure characterization was also performed to reveal the mechanism.

1.5 Thesis organization

The thesis organization is shown below:

Chapter 1 presents the general introduction of the research background of metal forming and fatigue fracture, while the effect of HDPEC on metallic materials was summarized. The potential problems and unclear issues regarding the effect of HDPEC on strain-hardening relief and microstructure evolution were pointed, and the research objectives of this study were presented.

Chapter 2 introduces the material and experimental method of this study. The experimental conditions of the tensile and fatigue test were presented, and the application conditions of HDPEC were also given. To evaluate the effect of HDPEC on the sample, the finite element method (FEM) simulation involving the electric field analysis, thermal field analysis, and stress field analysis was described. The FEM procedure was self-developed on the commercial software MATLAB, and the graphical user interface (GUI) was also presented. In addition, the evaluation methods of the changes in mechanical properties and microstructure, such as hardness test, residual stress and dislocation density analysis carried out by X-ray diffraction (XRD) measurement, local deformation and crystallographic properties analysis conducted by electron backscatter diffraction (EBSD) measurement, and surface morphology and fractography observation performed by scanning electron microscope (SEM) measurement, were introduced.

In Chapter 3, the effects of HDPEC on the strain-hardening relief of deformed IN718 under various HDPEC treatments were investigated. First of all, the temperature rise of the sample during HDPEC treatment was measured using thermal sensors, and the simulation result was also presented for comparison. The mechanical properties and microstructure evolution of the HDPEC-treated samples were examined. The results show that the strain hardening was successfully eliminated by HDPEC treatment, and the ductility was also recovered. In addition, the dislocation elimination induced by HDPEC was the dominant reason, while grain size and texture

evolution were the side effects in strain-hardening relief. The microstructure characterization indicates that the grain morphology of the HDPEC-treated samples tends to possess random orientation and equiaxed morphology.

Chapter 4 presents some specially-designed experiments to reveal the mechanisms of strain-hardening relief induced by HDPEC. First of all, the quasi-in-situ EBSD observation was conducted in this study to investigate the microstructure evolution caused by HDPEC. The dislocation motion and elimination induced by HDEPC were directly observed. Two ways of dislocation elimination caused by HDPEC as reported in previous studies, i.e., the combination of dipole dislocations and absorption in grain boundaries, were observed and confirmed. In particular, a new way for dislocation elimination, via EWF-driven dislocations entangled at the previous dislocation walls (i.e., sub-grain boundaries) and then forming new grain boundaries, was found in this study. Moreover, a designed experiment with several equivalent samples was also conducted to illuminate the contributions of thermal and athermal effects on strain-hardening relief induced by HDPEC. The results demonstrated that the athermal effect is more significant in strain-hardening relief than the thermal effect. Additionally, the high electric current is more effective in reducing dislocation density and relieving the strain hardening, which attributes to the large EWF (high current density) that helps dislocation overcome resistance to motion and thus realizing the annihilation. Most importantly, the difference between HDPEC treatment and traditional heat treatment in strain-hardening relief was elucidated in this study. Generally, the microstructure recovery induced by traditional heat treatment mainly relies on recrystallization, which involves thermally-activated dislocation climb. In contrast, the effect of HDPEC treatment on strain-hardening relief is related to the EWF-induced dislocation glide, which has been demonstrated to be a more efficient way in dislocation motion.

Chapter 5 presents the enhancement of the crack initiation life of the notched IN718 induced by HDPEC. First of all, the current density field, thermal field, and stress field ahead of the notch are presented using the self-developed FEM procedure.

The enhancement of crack initiation life induced by HDPEC at different stress levels was investigated. The results show that the crack initiation life was highly enhanced by HDPEC treatment, and the maximum increase rate reached 108.3% at the fatigue stress of σ_{max} = 250 MPa after multi-HDPEC treatment. The microstructure characterization shows that the fatigue-introduced plastic zone only affected ~2-grain area ahead of the notch root, and the dislocations at the plastic zone were evidently removed by HDPEC treatment.

Chapter 6 presents the conclusions and original contributions of this dissertation. A summary of future work was proposed.

References

[1] J.T. Black, R.A. Kohser, E.P. DeGarmo, DeGarmo's materials and processes in manufacturing, 11th ed, John Wiley & Sons, Hoboken, NJ, (2012).

[2] A.Y.C. Nee, ed., Handbook of Manufacturing Engineering and Technology, Springer London, London, (2015).

[3] T. O.A., Electromechanical effect in metals, ZhETF Pisma Redaktsiiu, 10 (1969) 18–22.

[4] O.A. Troitskii, Electroplastic deformation of metal, Strength Mater., 8 (1976) 1466–1471.

[5] O.A. Troitskii, V.I. Spitsyn, N.V. Sokolov, V.G. Ryzhkov, Application of high-density current in plastic working of metals, Phys. Stat. Sol., 52 (1979) 85–93.

[6] O.A. Troitskii, Pressure shaping by the application of a high energy, Materials Science and Engineering, 75 (1985) 37–50.

[7] K. Okazaki, M. Kagawa, H. Conrad, A study of the electroplastic effect in metals, Scripta Metallurgica, 12 (1978) 1063–1068.

[8] D. Yang, H. Conrad, Plastic deformation of fine-grained Al2O3 in the presence of an electric field, Scripta Materialia, 41 (1999) 397–401.

[9] H. Conrad, Effects of electric current on solid state phase transformations in metals, Materials Science and Engineering: A, 287 (2000) 227–237.

[10] H. Conrad, Electroplasticity in metals and ceramics, Materials Science and Engineering: A, 287 (2000) 276–287.

[11] H. Conrad, Influence of an electric or magnetic field on the liquid–solid transformation in materials and on the microstructure of the solid, Materials Science and Engineering: A, 287 (2000) 205–212.

[12] H. Conrad, J. Narayan, On the grain size softening in nanocrystalline materials, Scripta Materialia, 42 (2000) 1025–1030.

[13] H. Conrad, D. Yang, Influence of an electric field on the plastic deformation of fine-grained MgO at high homologous temperatures, Acta Materialia, 48 (2000) 4045–4052.

[14] D. Yang, H. Conrad, Exploratory study into the effects of an electric field and of high current density electropulsing on the plastic deformation of TiAl, Intermetallics, 9 (2001) 943–947.

[15] H. Conrad, D. Yang, Effect of an electric field on the plastic deformation kinetics of electrodeposited Cu at low and intermediate temperatures, Acta Materialia, 50 (2002) 2851–2866.

[16] H. Conrad, Thermally activated plastic flow of metals and ceramics with an electric field or current, Materials Science and Engineering: A, 322 (2002) 100–107.

[17] S.D. Antolovich, H. Conrad, The Effects of Electric Currents and Fields on Deformation in Metals, Ceramics, and Ionic Materials: An Interpretive Survey, Materials and Manufacturing Processes, 19 (2004) 587–610.

[18] H. Conrad, K. Jung, Effects of an Electric Field and Current on Phase Transformations in Metals and Ceramics, Materials and Manufacturing Processes, 19 (2004) 573–585.

[19] H. Conrad, D. Yang, Effect of DC electric field on the tensile deformation of

ultrafine-grained 3Y-TZP at 1450–1600°C, Acta Materialia, 55 (2007) 6789–6797.

[20] H. Conrad, D. Yang, P. Becher, Effect of an applied electric field on the flow stress of ultrafine-grained 2.5Y-TZP at high temperatures, Materials Science and Engineering: A, 477 (2008) 358–365.

[21] H. Conrad, D. Yang, Effect of the strength of an AC electric field compared to DC on the sintering rate and related grain size of zirconia (3Y-TZP), Materials Science and Engineering: A, 559 (2013) 591–594.

[22] H. Conrad, J. Wang, Equivalence of AC and DC electric field on retarding grain growth in yttria-stabilized zirconia, Scripta Materialia, 72–73 (2014) 33–34.

[23] H. Conrad, N. Karam, S. Mannan, Effect of electric current pulses on the recrystallization of copper, Scripta Metallurgica, 17 (1983) 411–416.

[24] H. Conrad, N. Karam, S. Mannan, Effect of prior cold work on the influence of electric current pulses on the recrystallization of copper, Scripta Metallurgica, 18 (1984) 275–280.

[25] H. Conrad, N. Karam, S. Mannan, A.F. Sprecher, Effect of electric current pulses on the recrystallization kinetics of copper, Scripta Metallurgica, 22 (1988) 235–238.

[26] M.-J. Kim, K. Lee, K.H. Oh, I.-S. Choi, H.-H. Yu, S.-T. Hong, H.N. Han, Electric current-induced annealing during uniaxial tension of aluminum alloy, Scripta Materialia, 75 (2014) 58–61.

[27] J.-H. Roh, J.-J. Seo, S.-T. Hong, M.-J. Kim, H.N. Han, J.T. Roth, The mechanical behavior of 5052-H32 aluminum alloys under a pulsed electric current, International Journal of Plasticity, 58 (2014) 84–99.

[28] J.Y. Liu, K.F. Zhang, Influence of electric current on superplastic deformation mechanism of 5083 aluminium alloy, Materials Science and Technology, 32 (2016) 540–546.

[29] M.-J. Kim, M.-G. Lee, K. Hariharan, S.-T. Hong, I.-S. Choi, D. Kim, K.H. Oh, H.N. Han, Electric current–assisted deformation behavior of Al-Mg-Si alloy

under uniaxial tension, International Journal of Plasticity, 94 (2017) 148–170.

[30] H. Krishnaswamy, M.J. Kim, S.-T. Hong, D. Kim, J.-H. Song, M.-G. Lee, H.N. Han, Electroplastic behaviour in an aluminium alloy and dislocation density based modelling, Materials & Design, 124 (2017) 131–142.

[31] B.J. Ruszkiewicz, L. Mears, J.T. Roth, Investigation of Heterogeneous Joule Heating as the Explanation for the Transient Electroplastic Stress Drop in Pulsed Tension of 7075-T6 Aluminum, Journal of Manufacturing Science and Engineering, 140 (2018) 091014.

[32] E. Simonetto, S. Bruschi, A. Ghiotti, Electroplastic effect on AA1050 plastic flow behavior in H24 tempered and fully annealed conditions, Procedia Manufacturing, 34 (2019) 83–89.

[33] H. Xu, X. Liu, D. Zhang, X. Zhang, Minimizing serrated flow in Al-Mg alloys by electroplasticity, Journal of Materials Science & Technology, 35 (2019) 1108–1112.

[34] X. Xu, Y. Zhao, B. Ma, J. Zhang, M. Zhang, Rapid grain refinement of 2024 Al alloy through recrystallization induced by electropulsing, Materials Science and Engineering: A, 612 (2014) 223–226.

[35] C.D. Ross, T.J. Kronenberger, J.T. Roth, Effect of dc on the Formability of Ti–6Al–4V, Journal of Engineering Materials and Technology, 131 (2009) 031004.

[36] H. Song, Z. Wang, T. Gao, Effect of high density electropulsing treatment on formability of TC4 titanium alloy sheet, Transactions of Nonferrous Metals Society of China, 17 (2007) 87–92.

[37] Z. Wang, H. Song, Effect of electropulsing on anisotropy behaviour of cold-rolled commercially pure titanium sheet, Transactions of Nonferrous Metals Society of China, 19 (2009) s409–s413.

[38] H. Song, Z. Wang, Improvement of mechanical properties of cold-rolled commercially pure Ti sheet by high density electropulsing, Transactions of Nonferrous Metals Society of China, 22 (2012) 1350–1355.

[39] H. Song, Z. Wang, X. He, Improving in plasticity of orthorhombic Ti2AlNb-based alloys sheet by high density electropulsing, Transactions of Nonferrous Metals Society of China, 23 (2013) 32–37.

[40] H. Shao, D. Shan, K. Wang, G. Zhang, Y. Zhao, Trade-off of rapid recrystallization and mechanical property improvement of Ti-6Al-4V alloy, Results in Physics, 15 (2019) 102722.

[41] S. Zhao, R. Zhang, Y. Chong, X. Li, A. Abu-Odeh, E. Rothchild, D.C. Chrzan, M. Asta, J.W. Morris, A.M. Minor, Defect reconfiguration in a Ti–Al alloy via electroplasticity, Nat. Mater., (2020).

[42] H. Song, Z.-J. Wang, Microcrack healing and local recrystallization in pre-deformed sheet by high density electropulsing, Materials Science and Engineering: A, 490 (2008) 1–6.

[43] H. Song, Z. Wang, Grain refinement by means of phase transformation and recrystallization induced by electropulsing, Transactions of Nonferrous Metals Society of China, 21 (2011) s353–s357.

[44] Z. Xu, G. Tang, S. Tian, F. Ding, H. Tian, Research of electroplastic rolling of AZ31 Mg alloy strip, Journal of Materials Processing Technology, 182 (2007) 128–133.

[45] Y. Jiang, L. Guan, G. Tang, C. Shek, Z. Zhang, Influence of electropulsing treatment on microstructure and mechanical properties of cold-rolled Mg–9Al–1Zn alloy strip, Materials Science and Engineering: A, 528 (2011) 5627–5635.

[46] Y. Jiang, G. Tang, C. Shek, W. Liu, Microstructure and texture evolution of the cold-rolled AZ91 magnesium alloy strip under electropulsing treatment, Journal of Alloys and Compounds, 509 (2011) 4308–4313.

[47] Q. Xu, G. Tang, Y. Jiang, Thermal and electromigration effects of electropulsing on dynamic recrystallization in Mg–3Al–1Zn alloy, Materials Science and Engineering: A, 528 (2011) 4431–4436.

[48] J.D. Guo, X.L. Wang, W.B. Dai, Microstructure evolution in metals induced by

high density electric current pulses, Materials Science and Technology, 31 (2015) 1545–1554.

[49] M. Gzyl, A. Rosochowski, S. Boczkal, L. Olejnik, The role of microstructure and texture in controlling mechanical properties of AZ31B magnesium alloy processed by I-ECAP, Materials Science and Engineering: A, 638 (2015) 20–29.

[50] Y. Jiang, L. Guan, G. Tang, Z. Zhang, Improved mechanical properties of Mg–9Al–1Zn alloy by the combination of aging, cold-rolling and electropulsing treatment, Journal of Alloys and Compounds, 626 (2015) 297–303.

[51] W. Jin, J. Fan, H. Zhang, Y. Liu, H. Dong, B. Xu, Microstructure, mechanical properties and static recrystallization behavior of the rolled ZK60 magnesium alloy sheets processed by electropulsing treatment, Journal of Alloys and Compounds, 646 (2015) 1–9.

[52] R. Zhang, X. Li, J. Kuang, X. Li, G. Tang, Texture modification of magnesium alloys during electropulse treatment, Materials Science and Technology, 33 (2017) 1421–1427.

[53] X. Li, X. Li, S.-Z. Kure-Chu, G. Tang, A Comparative Study on the Static Recrystallization Behavior of Cold-Rolled Mg-3Al-1Zn Alloy Stimulated by Electropulse Treatment and Conventional Heat Treatment, Metall and Mat Trans A., 49 (2018) 613–627.

[54] Y. Zhou, W. Zhang, B. Wang, J. Guo, Ultrafine-grained microstructure in a Cu–Zn alloy produced by electropulsing treatment, J. Mater. Res., 18 (2003) 1991–1997.

[55] Y. Zhou, S. Xiao, J. Guo, Recrystallized microstructure in cold worked brass produced by electropulsing treatment, Materials Letters, 58 (2004) 1948–1951.

[56] X. Wang, W. Dai, C. Ma, X. Zhao, Effect of electric current direction on recrystallization rate and texture of a Cu–Zn alloy, J. Mater. Res., 28 (2013) 1378–1385.

[57] J. Zhu, S. Liu, Y. Lin, G. Wang, Effect of Electropulsing on Microstructure and

Properties of Severely Plastically Deformed Pure Copper Sheet, J. of Materi Eng and Perform, 29 (2020) 841–848.

[58] C. Gennari, L. Pezzato, E. Simonetto, R. Gobbo, M. Forzan, I. Calliari, Investigation of Electroplastic Effect on Four Grades of Duplex Stainless Steels, Materials, 12 (2019) 1911.

[59] Y. Zhou, W. Zhang, B. Wang, G. He, J. Guo, Grain refinement and formation of ultrafine-grained microstructure in a low-carbon steel under electropulsing, J. Mater. Res., 17 (2002) 2105–2111.

[60] G. Hu, Y. Zhu, G. Tang, C. Shek, J. Liu, Effect of Electropulsing on Recrystallization and Mechanical Properties of Silicon Steel Strips, Journal of Materials Science & Technology, 27 (2011) 1034–1038.

[61] W.A. Salandro, J.J. Jones, C. Bunget, L. Mears, J.T. Roth, Electrically Assisted Forming, Springer International Publishing, Cham, (2015).

[62] C.D. Ross, T.J. Kronenberger, J.T. Roth, Effect of dc on the Formability of Ti–6Al–4V, Journal of Engineering Materials and Technology, 131 (2009) 031004.

[63] J.J. Jones, L. Mears, J.T. Roth, Electrically-Assisted Forming of Magnesium AZ31: Effect of Current Magnitude and Deformation Rate on Forgeability, Journal of Manufacturing Science and Engineering, 134 (2012) 034504.

[64] Z. Xu, G. Tang, S. Tian, F. Ding, H. Tian, Research of electroplastic rolling of AZ31 Mg alloy strip, Journal of Materials Processing Technology, 182 (2007) 128–133.

[65] Y. Lu, T. Qu, P. Zeng, L. Lei, G. Fang, J. Sun, The influence of electroplastic rolling on the mechanical deformation and phase evolution of Bi-2223/Ag tapes, J Mater Sci., 45 (2010) 3514–3519.

[66] G. Tang, J. Zhang, M. Zheng, J. Zhang, W. Fang, Q. Li, Experimental study of electroplastic effect on stainless steel wire 304L, Materials Science and Engineering: A, 281 (2000) 263–267.

[67] G. Tang, J. Zhang, Y. Yan, H. Zhou, W. Fang, The engineering application of the

electroplastic effect in the cold-drawing of stainless steel wire, Journal of Materials Processing Technology, 137 (2003) 96–99.

[68] Z. Zimniak, G. Radkiewicz, The electroplastic effect in the cold-drawing of copper wires for the automotive industry, Archiv.Civ.Mech.Eng., 8 (2008) 173–179.

[69] V.I. Stashenko, O.A. Troitskii, N.N. Novikova, Electroplastic drawing of a cast-iron wire, J. Mach. Manuf. Reliab., 38 (2009) 182–184.

[70] W. Shaozuo, Effect of Electric Pulses on Drawability and Corrosion Property of AZ31 Magnesium Alloy, Master's thesis, Tsinghua University, (2009).

[71] C. Li, H. Tan, W.M. Wu, S. Zhao, H.B. Zhang, Effect of electropulsing treatment on microstructure and tensile fracture behavior of nanocrystalline Ni foil, Materials Science and Engineering: A, 657 (2016) 347–352.

[72] K. Li, F. Gao, Heterogeneity of grain refinement and texture formation during pulsed electric current sintering of conductive powder: A case study in copper powder, Advanced Powder Technology, 29 (2018) 3385–3393.

[73] Y. Sheng, Y. Hua, X. Wang, X. Zhao, L. Chen, H. Zhou, J. Wang, C. Berndt, W. Li, Application of High-Density Electropulsing to Improve the Performance of Metallic Materials: Mechanisms, Microstructure and Properties, Materials, 11 (2018) 185.

[74] H.S. Maharana, B. Bishoyi, A. Basu, Current density dependent microstructure and texture evolution and related effects on properties of electrodeposited Ni-Al coating, Journal of Alloys and Compounds, 787 (2019) 483–494.

[75] H.-J. Jeong, M.-J. Kim, S.-J. Choi, J.-W. Park, H. Choi, V.T. Luu, S.-T. Hong, H.N. Han, Microstructure reset-based self-healing method using sub-second electric pulsing for metallic materials, Applied Materials Today, 20 (2020) 100755.

[76] D. Waryoba, Z. Islam, B. Wang, A. Haque, Recrystallization mechanisms of Zircaloy-4 alloy annealed by electric current, Journal of Alloys and Compounds,

820 (2020) 153409.

[77] D. Gross, T. Seelig, Fracture Mechanics, Springer Berlin Heidelberg, Berlin, Heidelberg, (2011).

[78] J. Schijve, Fatigue of Structures and Materials, 2nd ed., Springer Netherlands, (2009).

[79] N. Hironobu, G. Masahiro, K. Norio, A small-crack growth law and its related phenomena, Engineering Fracture Mechanics, 41 (1992) 499–513.

[80] F.V. Lawrence, W.H. Munse, Fatigue Crack Propagation in Butt Welds Containing Joint Penetration Defects, 52 (1973) 5.

[81] N. Lautrou, D. Thevenet, J.-Y. Cognard, Fatigue crack initiation life estimation in a steel welded joint by the use of a two-scale damage model, Fatigue & Fracture of Engineering Materials & Structures, 32 (2009) 403–417.

[82] E. Delosrios, A. Walley, M. Milan, G. Hammersley, Fatigue crack initiation and propagation on shot-peened surfaces in A316 stainless steel, International Journal of Fatigue, 17 (1995) 493–499.

[83] K. Oguri, Fatigue life enhancement of aluminum alloy for aircraft by Fine Particle Shot Peening (FPSP), Journal of Materials Processing Technology, 211 (2011) 1395–1399.

[84] P. Ganesh, R. Sundar, H. Kumar, R. Kaul, K. Ranganathan, P. Hedaoo, G. Raghavendra, S. Anand Kumar, P. Tiwari, D.C. Nagpure, K.S. Bindra, L.M. Kukreja, S.M. Oak, Studies on fatigue life enhancement of pre-fatigued spring steel specimens using laser shock peening, Materials & Design, 54 (2014) 734–741.

[85] A.G. Sanchez, C. You, M. Leering, D. Glaser, D. Furfari, M.E. Fitzpatrick, J. Wharton, P.A.S. Reed, Effects of laser shock peening on the mechanisms of fatigue short crack initiation and propagation of AA7075-T651, International Journal of Fatigue, 143 (2021) 106025.

[86] H. Conrad, J. White, W.D. Cao, X.P. Lu, A.F. Sprecher, Effect of electric current

pulses on fatigue characteristics of polycrystalline copper, Materials Science and Engineering: A, 145 (1991) 1–12.

[87] Y. Zhou, R. Qin, S. Xiao, G. He, B. Zhou, Reversing effect of electropulsing on damage of 1045 steel, J. Mater. Res., 15 (2000) 1056–1061.

[88] Z. Yizhou, Z. You, H. Guanhu, Z. Benlian, The healing of quenched crack in 1045 steel under electropulsing, J. Mater. Res., 16 (2001) 17–19.

[89] R. Qin, S. Su, Thermodynamics of crack healing under electropulsing, J. Mater. Res., 17 (2002) 5.

[90] Y. Zhou, J. Guo, M. Gao, G. He, Crack healing in a steel by using electropulsing technique, Materials Letters, 58 (2004) 1732–1736.

[91] H. Song, Z.-J. Wang, Microcrack healing and local recrystallization in pre-deformed sheet by high density electropulsing, Materials Science and Engineering: A, 490 (2008) 1–6.

[92] A. Hosoi, T. Nagahama, Y. Ju, Fatigue crack healing by a controlled high density electric current field, Materials Science and Engineering: A, 533 (2012) 38–42.

[93] X.G. Zheng, Y.-N. Shi, K. Lu, Electro-healing cracks in nickel, Materials Science and Engineering: A, 561 (2013) 52–59.

[94] A. Hosoi, T. Yano, Y. Morita, Y. Ju, Quantitative evaluation of the displacement distribution and stress intensity factor of fatigue cracks healed by a controlled high-density electric current field: QUANTITATIVE EVALUATION OF FATIGUE CRACK HEALED BY ELECTRIC CURRENT, Fatigue Fract Engng Mater Struct., 37 (2014) 1025–1033.

[95] S. Wei, G. Wang, D. Deng, Y. Rong, Microstructure characterization and thermal behavior around crack tip under electropulsing, Appl. Phys. A., 121 (2015) 69–76.

[96] J. Jung, Y. Ju, Y. Morita, Y. Toku, Y. Uematsu, Delaying Effect of High-Density Electric Current on Fatigue Crack Growth in A6061-T6 Aluminum Alloy, Mater. Trans., 57 (2016) 2104–2109.

[97] T. Yu, D. Deng, G. Wang, H. Zhang, Crack healing in SUS304 stainless steel by

electropulsing treatment, Journal of Cleaner Production, 113 (2016) 989–994.

[98] J. Jung, Y. Ju, Y. Morita, Y. Toku, Enhancement of fatigue life of aluminum alloy affected by the density of pulsed electric current, International Journal of Fatigue, 103 (2017) 419–425.

[99] H. Song, Z. Wang, X. He, J. Duan, Self-healing of damage inside metals triggered by electropulsing stimuli, Sci Rep., 7 (2017) 7097.

[100] A. Kumar, S.K. Paul, Healing of fatigue crack in steel with the application of pulsed electric current, Materialia, 14 (2020) 100906.

[101] S. Yoon, Y. Cui, Y. Kimura, S. Gu, Y. Toku, Y. Ju, Improvement of low-cycle fatigue life of austenitic stainless steel by multiple high-density pulsed electric currents, International Journal of Fatigue, (2021) 106639.

[102] S. Yoon, Y. Kimura, Y. Cui, Y. Toku, Y. Ju, Evaluation of Electric Current-Induced Improvement of Fracture Characteristics in SUS316, Mater. Trans., 62 (2021) 748–755.

[103] Y. Tang, A. Hosoi, Y. Iwase, Y. Ju, Effect of High-Density Electric Current on the Microstructure and Fatigue Crack Initiation of Stainless Steel, Mater. Trans., 54 (2013) 2085–2092.

[104] Y. Tang, A. Hosoi, Y. Morita, Y. Ju, Restoration of fatigue damage in stainless steel by high-density electric current, International Journal of Fatigue, 56 (2013) 69–74.

[105] H. Conrad, A.F. Sprecher, The electroplastic effect in metals, in: Dislocations in Solids, Elsevier, (1989): pp. 497–541.

[106] J.-S. Zhang, High Temperature Deformation and Fracture of Materials, 1st edition, Woodhead Publishing, Oxford, (2010).

[107] F.R.N. Nabarro, Theory of Crystal Dislocations, Clarendon Press, Oxford, (1967).

[108] V.Y. Kravchenko, Effect of directed electron beam on moving dislocations, Journal of Experimental and Theoretical Physics, 24 (1967) 1135–1142.

[109] X. Suhong, Z. Yizhou, G. Jingdong, W. Shiding, Y. Ge, L. Shouxin, H. Guanhu, Z. Benlian, The effect of high current pulsing on persistent slip bands in fatigued copper single crystals, Materials Science and Engineering: A, 332 (2002) 351–355.

[110] S. Zhao, R. Zhang, Y. Chong, X. Li, A. Abu-Odeh, E. Rothchild, D.C. Chrzan, M. Asta, J.W. Morris, A.M. Minor, Defect reconfiguration in a Ti–Al alloy via electroplasticity, Nat. Mater. (2020).

Chapter 2 Material and experimental method

2.1 Material and sample geometry

The Inconel 718 (IN718) is a nickel-iron base superalloy containing mainly chromium, niobium, molybdenum, small amounts of aluminum and titanium, and the chemical composition is given in Table 2-1. Owing to the superior mechanical properties and creep resistance at elevated temperatures to 650°C, IN718 is the widely used Ni-based superalloy (around 50% occupation) in the aerospace industry, power plant, etc.

Table 2-1 Chemical composition (wt.%) of IN718.

Ni	C	Mn	Fe	Cu	Cr	Al	Ti	Co	Mo	Nb	P	S
Bal.	0.03	0.10	17.67	0.12	18.59	0.55	0.93	0.19	2.88	5.07	0.009	0.001

For the tensile test, a dumbbell-shaped sample with an 18 mm gauge length and a cross-section area of 3.5×1.6 mm^2 was prepared by wire-cutting, as shown in Fig. 2-1. After machining, the solution heat treatment (954°C for 1 hour and then air cooling) was applied to remove the residual strain in the samples and obtain the uniform microstructure. Furthermore, to examine the material properties of the as-annealed sample, the tensile and hardness tests were used, and the mechanical properties of the as-annealed sample were obtained, as shown in Table 2-2. For the fatigue test, a dumbbell-shaped sample with a notch was processed, and the sample geometry was shown in Fig. 2-2.

After heat treatment, the samples were grinded by emery papers at the grades of #240, #400, #600, #800, #1200, #1500, and #2000, and polished to a mirror-like surface with 3μm water-based diamond suspension on a polishing machine (LaboPol-20, Struers) for 15 mins. For EBSD observation, the final polishing with a mixed solution of 80% OP-S alcohol-silica suspension solution, 10% Hydrogen Peroxide

solution (H_2O_2, 30%), and 10% Ammonium hydroxide solution (NH_4OH, 25%) was used to remove the remained minor deformed layer. The hardness test, X-ray diffraction test, and surface morphology observation were carried out on the final polished samples to avoid the test results being influenced by the surface conditions.

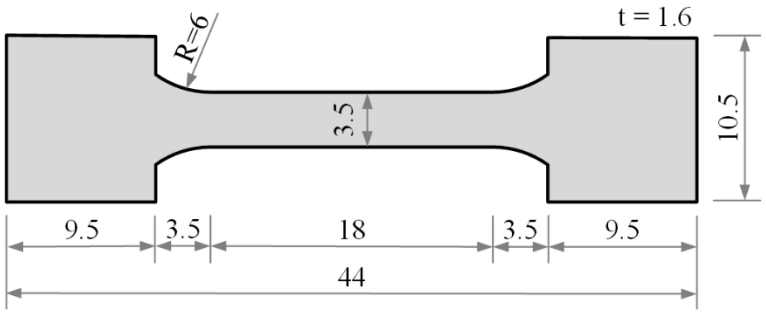

Fig. 2-1 Sample geometry of the tensile test (unit: mm).

Table 2-2 Mechanical properties of solution treated IN718.

Yield stress / MPa	Ultimate stress / MPa	Elongation / %	Young's modulus / GPa	Hardness / HV
623±21	1127±18	41.3±0.9	201	207±3

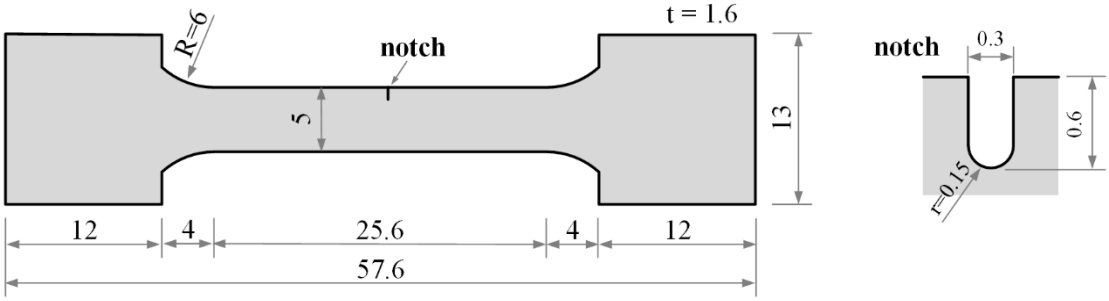

Fig. 2-2 Sample geometry of the fatigue test with a notch (unit: mm).

2.2 Tensile and fatigue test

The tensile test was performed on a hydraulic-driven equipment (SFL-50kN-B, SHIMAZU) at ambient temperature (25°C) with a tension speed of 0.03 mm/s. For studying the effect of high-density pulsed electric current on the strain-hardening relief in IN718, the pre-strain was introduced using tensile stretch. In this study, the pre-strain of 20.5% (50% of ε_p the plastic strain at the breaking point) was applied.

The fatigue test was performed on the same machine at ambient temperature. The three stress levels of σ_{max}=250 MPa, 300 MPa, and 350 MPs were conducted under the stress ratio R=0.1 with a loading frequency f=25Hz. For evaluating the crack initiation, an optical microscope (VH-2100R, KEYENCE) was used. The limitation of crack length for the crack initiation was chosen as ~30 μm (~2 times of grain size) in this study. The interrupted fatigue test (e.g., at every 5000 cycles for σ_{max}=250 MPa cases) was performed to check the length of the initiated crack.

2.3 Application of high-density pulsed electric current and temperature measurement

The application of HDPEC was conducted on fusing welding power supply MDA-8000B (MIYACHI) and IS-300A (MIYACHI). The previous equipment is used for the relatively high current density cases (~300 A/mm^2), while the latter one is for the cases of low current density (~100 A/mm^2). Since the duration time of each pulse is also limited (MDA-8000B, ~20 ms, and IS-300A, ~1000 ms), the multi-pulse was applied. The schematic and actual images of the HDPEC application are presented in Fig. 2-3 and 2-4, respectively.

In this study, two non-contact infrared temperature measurement sensors (GTL-3ML-CF4, 50~400°C, and GTL-2MH-FF, 385~1600°C) were used to measure the temperature of the samples during the HDPEC treatment, as shown in Fig. 2-4. The

resolution of them is up to 0.1°, and the sampling frequency is 1000 Hz. After the data collection of the two sensors simultaneously, the two sets of data can be joined and combined into a single data using MATLAB.

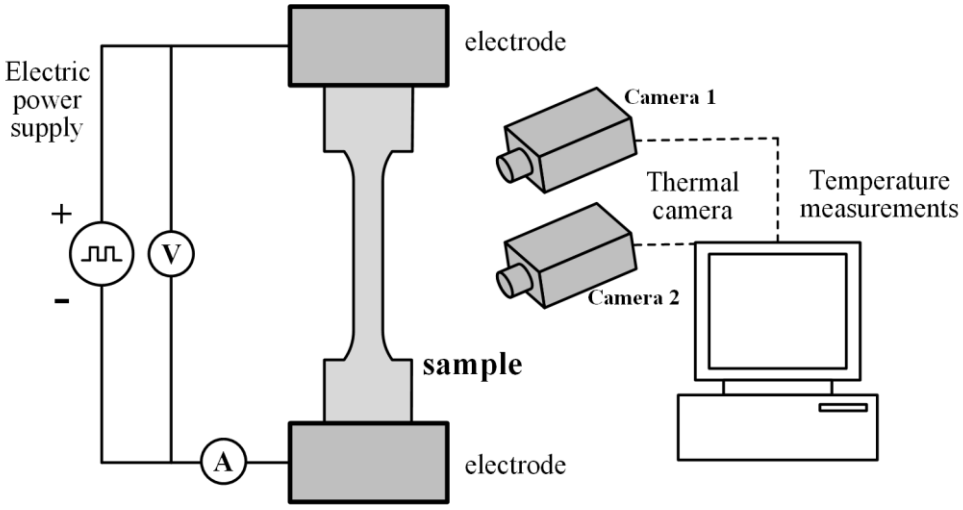

Fig. 2-3 Schematic diagram of the HDPEC application and temperature measurement.

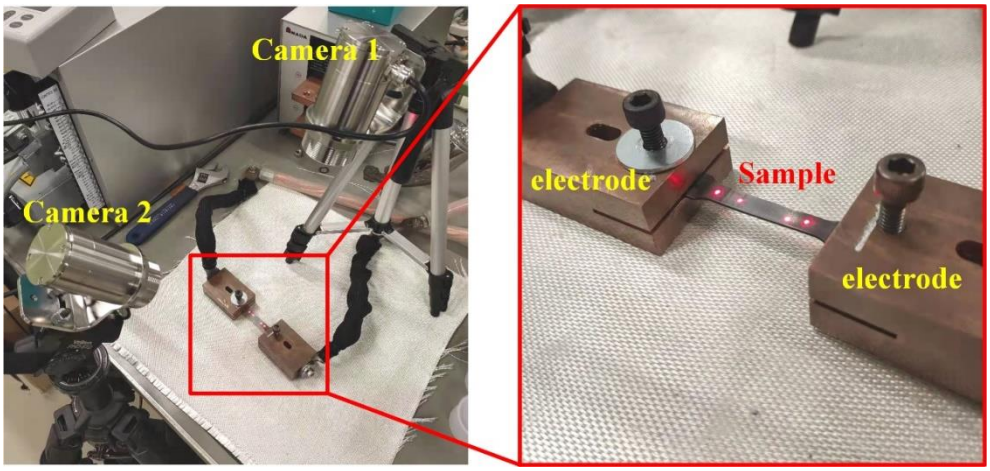

Fig. 2-4 The actual images of the HDPEC application.

2.4 Finite element method

To examine the current, temperature, and stress fields in the sample during HDPEC treatment, the finite element method (FEM) was conducted in this study. Especially for the notched sample, where the dramatic changes in the distribution of the current field near the notch root, the FEM simulation is necessary.

The concept of FEM was first proposed by Clough [1] in the early 1960s to solve the plane stress problem. After nearly 60 years of development, especially in the last 30 years, the theory and method of FEM have become very mature and now is widely used for solving differential equations arising in the fields of engineering, mathematics, and physics. The idea of FEM can be briefly described as follows: the FEM first allows the continuous object to be discretized into many parts (or elements), which is implemented by the construction of a mesh of the object. Each element is controlled by linear equations via the nodes to transfer displacement, force, heat flow, current flow, etc. After assembling the discretized elements, the problem is transferred to solve a large number of linear equations. It is just as well that with the advances in computer technology and numerical methods, the FEM has been rapidly developed in applied science and engineering.

In terms of the sample geometry and experimental conditions in this study, the model can be reduced to the 2-dimensional plane stress problem. Since the current flow can arouse thermal and thermal stress, the simulation contains three parts. The first part is the electrostatic field analysis since the model is subjected to an electric potential. The second part is the thermal field analysis because the Joule heating occurred during electric current flow. The last part is the stress field analysis, which is caused by the inhomogeneous thermal expansion. Two kinds of element types, triangular elements and quadrilateral elements, were utilized in this study to discretize the model. The quadrilateral elements have a higher degree of accuracy than the triangular elements while lack of flexibility and adaptability for meshing irregular models. Hence, the quadrilateral elements were applied to the tensile sample (regular

geometry without notch or crack) in this study, and the fatigue sample used the triangular elements for discretization. Here need to mention, an open-source MATLAB code DistMesh [2,3] was used for the triangular meshes of the model. The quadrilateral discretization is performed using the author's self-developed procedures with methods of model partitioning and sweeping. The sample geometry and FEM model of tensile test with quadrilateral elements are shown in Fig. 2-5. Finally, the procedure was developed on commercial software MATLAB based on the FEM theory and method. Moreover, the graphical user interface (GUI) was also presented for easy access. For details, please see Appendix 2.

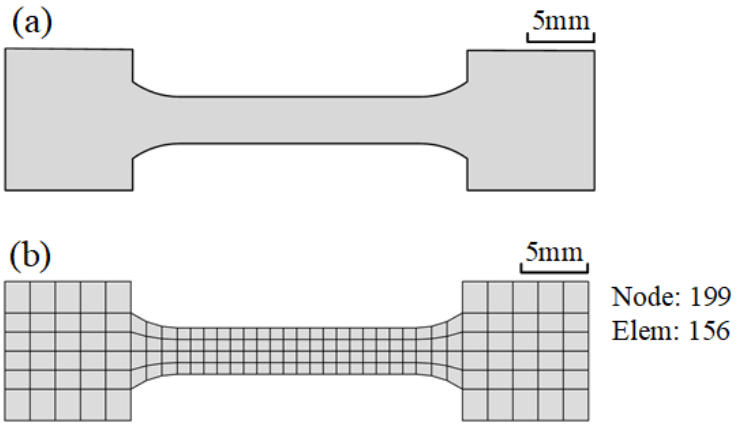

Fig. 2-5 (a) Sample geometry of tensile test and (b) FEM model with quadrilateral elements.

2.5 Evaluation methods of mechanical properties and microstructure

2.5.1 Measurement of hardness

Hardness testing is a well-accepted method of evaluating the mechanical properties of engineered materials. Based on theoretical analyses and experimental results, an approximate relationship between hardness and strength of $HV \approx 3\sigma_y$ is widely known [4,5] in material science. Hence, the hardness test is widely used for strength

evaluation due to its simplicity, convenience, and nearly non-destructiveness.

The hardness test was performed on a micro-hardness Vickers indenter (HWV-G-XY-D, SHIMADZU) under a load of 4.9 N holding for 10 s. An average hardness value has been determined based on the measured data from 3×3 matrix pattern indentations. The distance of each indentation was 300 μm to prevent interaction between the work-hardened regions.

2.5.2 Residual stress and dislocation density analysis

1. Residual stress estimated by XRD

X-ray diffraction (XRD) method was applied to measure the surface residual stress of the pre-strained or HDPEC-treated samples. The measurement was carried out on an X-ray stress analyzer by the Cu-K_α radiation at 30 kV (10 mA) to obtain {220} diffraction peak at around 74.5°. To prevent the detection of banding created due to the presence of Cu-K_β radiation, a nickel foil was used to filter the detected radiation beams. The multi-segment baseline correction method was used to remove the background of the raw data, and the least-squares fit method proposed by Savitzky and Golay [6] was also applied to smooth the data. Moreover, Lorenz function fitting was used to divide each peak into the profiles caused by Cu-$K_{\alpha1}$ and Cu-$K_{\alpha2}$ radiation, and only the profiles obtained by Cu-$K_{\alpha1}$ are necessary. The 2θ-$\sin^2\psi$ method involving 9 tilt angles with ψ=0, ±14.48, ±20.7, ±25.66, ±30° was performed to calculate the surface residual stress. The negative and positive tilt angles used here avoided the 'ψ-splitting' of the results. The equation is written as [7,8]:

$$A_\Psi^+ = \frac{1}{2}(2\theta_{\Psi>0} + 2\theta_{\Psi<0}) \qquad (2-1)$$

$$\sigma = \frac{1}{K_2}\frac{\partial(A_\Psi^+)}{\partial(\sin^2\Psi)} \qquad (2-2)$$

where ψ is the tilt angle. $2\theta_{\psi>0}$ and $2\theta_{\psi<0}$ are the 2θ diffraction angles at positive and

negative ψ angles, respectively. K_2 is the x-ray elastic constant.

According to Eq. (2-2), a plot of A^+_ψ versus $\sin^2\psi$ was fit a line using a least-squares linear regression algorithm. Then, based on the obtained slope of the regression line and elastic constant K_2, the residual stress was obtained. The elastic constant of IN718 at the chosen diffraction peak {220} is K_2=-1984 MPa [7].

2. Dislocation density estimated by XRD

The line profile analysis of the XRD patterns was performed to evaluate the dislocation density, which can promulgate the average macroscopic value of the lattice defect. The same X-ray analyzer was also used, and the scanning angle ranged from 2θ=40~95° with a scanning step of 0.02° to obtain the diffraction peaks of (111), (200), (220), and (311). The same processes, such as background removing and noise smoothing, as mentioned before, were also performed on the raw pattern profile data. The value of full width at half maximum (FWHM) of each peak was obtained after eliminating the profiles caused by Cu-$K_{\alpha 2}$. The dislocation density was evaluated by the modified Williamson-Hall method [9-11]. The equation is written as,

$$\Delta K \cong \frac{0.9}{D} + \left(\frac{\pi M^2 b^2}{2}\right)^{\frac{1}{2}} \rho^{\frac{1}{2}} K \bar{C}^{\frac{1}{2}} + o(K^2\bar{C}) \qquad (2-3)$$

where ΔK=2cos$\theta(\Delta\theta)/\lambda$ and K=2sinθ/λ. Parameter $\Delta\theta$ is the length of FWHM, θ diffraction angle, λ the wavelength of the X-ray, D the mean grain size, ρ the dislocation density of the sample, b the Burgers vector, M is a constant. Symbol o represents the higher-order term of $K^2\ \bar{C}$. Eq. (2-3) can be deduced into the following equation with neglect the term of $o(K^2\ \bar{C})$, shown as:

$$\frac{(\Delta K)^2 - \alpha}{K^2} \cong \beta \bar{C} \qquad (2-4)$$

where α=$(0.9/D)^2$ and $\beta=\pi M^2 b^2 \rho/2$. $\bar{C}$ can be expressed as $\bar{C}=\ \bar{C}_{h00}(1-qH^2)$, which is related to the mean contrast of different dislocations. $\bar{C}_{h00}$ is a constant regarding the lattice structure and the material properties. For the Ni-based alloy IN718 used in

the present study, $\bar{C}_{h00}$=0.2456 [12]. Parameter q is related to the dislocation types. $H^2=(h^2k^2+h^2l^2+k^2l^2)/(h^2+k^2+l^2)$, where ($hkl$) is the Miller indices of cubic lattice.

The relationship of α-H^2 can be determined at a series of H^2 by Eq. (2-4), and the linear fitting can be obtained. Parameter q is related to the slope of the fitting line, and the value can be calculated. Hence, the value of $\bar{C}$ can be obtained.

Moreover,

$$\ln A(L) \cong \ln A^S(L) - \rho \frac{\pi b^2}{2} L^2 \ln\left(\frac{R_e}{L}\right)(K^2\bar{C}) \qquad (2-5)$$

where $A(L)$ is the real part of the Fourier transform of each XRD peak, L is the Fourier variable, $L=n\lambda/\{2(\sin\theta_2-\sin\theta_1)\}$, and parameter $\ln A^S(L)$ represents the size of the crystal. R_e is the effective outer cut-off radius of dislocations.

As shown in the above equation, the relationship between $\ln A(L)$ and $K^2\bar{C}$ can be obtained at different L, hence, the coefficient of $Y = \rho \frac{\pi b^2}{2} L^2 \ln\left(\frac{R_e}{L}\right)$ was determined. Rewritten as:

$$\frac{Y}{L^2} = \rho \frac{\pi b^2}{2} \ln(R_e) - \rho \frac{\pi b^2}{2} \ln(L) \qquad (2-6)$$

Hence, the value of dislocation density ρ is evaluated from the slope of the regression line between Y/L^2 and $\ln(L)$.

2.5.3 Local deformation and crystallographic properties evaluation

EBSD method was applied to estimate the grain-scale deformation in this study. Crystal orientations were measured using HKL Channel 5 (Oxford Instruments) on an EBSD detector (NordlysNano, Oxford) interfaced on an SEM (SU8230, HITACHI). The data processing was performed on the commercial software MATLAB with an open-source toolbox MTEX. Furthermore, the in-situ EBSD observation was also carried out on the sample before and after HDPEC treatment. The oxidation layer caused by HDPEC treatment was removed by Ar^+ ion milling with the acceleration

voltage of 6 kV for 15 min on IM4000PLUS (HITACHI).

1. Kernel averaged misorientation analysis

The kernel averaged misorientation (KAM) is related to the local crystal orientation change, which is commonly used to imply the grain-scale plastic strain [13,14]. The value of KAM is a mean value between the measured point with the surrounded points in one grain, and the mode of the square grid was used in this study, as shown in Fig. 2-6. The misorientation of the fixed point p_0 can be obtained using equations (2-7, 2-8) at the inner grains or near the grain boundary. The details are shown in Ref. [15,16].

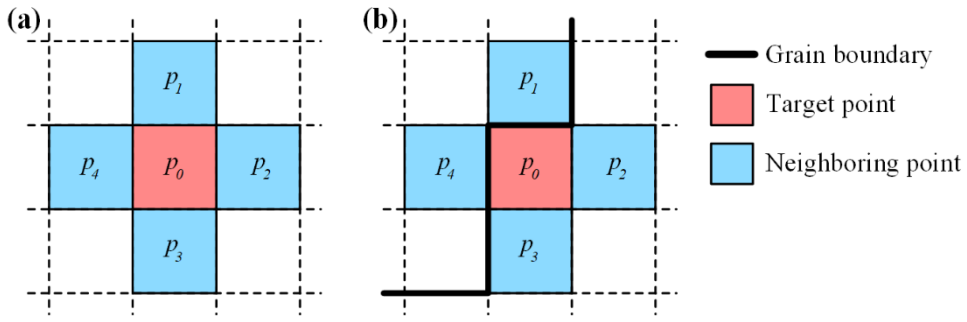

Fig. 2-6 Definition of local misorientation. The target point is (a) far from and (b) near the grain boundary.

$$M_L(p_0) = \frac{1}{4}\{\theta(p_0,p_1) + \theta(p_0,p_2) + \theta(p_0,p_3) + \theta(p_0,p_4)\} \qquad (2-7)$$

$$M_L(p_0) = \frac{1}{2}\{\theta(p_0,p_2) + \theta(p_0,p_3)\} \qquad (2-8)$$

where $M_L(p_0)$ is the local misorientation at the point p_0. $\theta(p_0,p_i)$ represents the orientation change between the measured point p_0 and the surrounding points p_i in one grain.

2. Geometrically necessary dislocation analysis

In general, dislocations can usually be divided into two categories depending on whether they promote lattice curvature (or lattice torsion): statistically-stored dislocations (SSDs) and geometrically-necessary dislocations (GNDs). SSDs have no contributions to lattice torsion and often occur in pairs, as shown in Fig. 2-7. In contrast, GNDs are related to the lattice torsion and cause lattice misorientation, which was first proposed by Nye [17]. The density of GND is related to the misorientation, which can estimate by a simple equation based on the strain gradient model [18-20], as shown,

$$\rho_{GND} = \frac{2M_L}{bx_0} \qquad (2-9)$$

where b is the Burgers vector, x_o the scan step size.

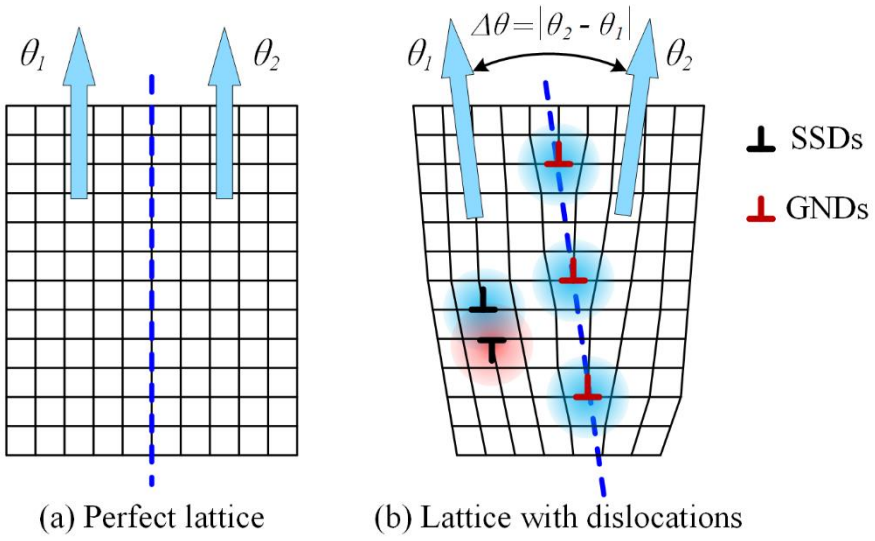

Fig. 2-7 Schematic diagram of lattice (a) without and (b) with dislocations.

The general precision of the EBSD is approximately ~1° for measuring the crystal orientation, which will lead to an overestimation of the GNDs density. Kamaya [16] reported an effective method for evaluating the noise of the EBSD measurement. The first to fifth-order local misorientations were presented, denoted by M_L^1, M_L^2, M_L^3,

$M_L^{4,}$ and M_L^5, as shown in Fig. 2-8. If the disorientation gradient is constant, the value of local misorientation should be proportional to the distance of the considered neighbors. The regression line of the local misorientation versus kernel radius can be obtained, and the intercept at x=0 is the measurement noise. Then the gradient of the crystal orientation G_L, is defined as,

$$G_L = \frac{\partial M_L}{\partial x} \qquad (2-10)$$

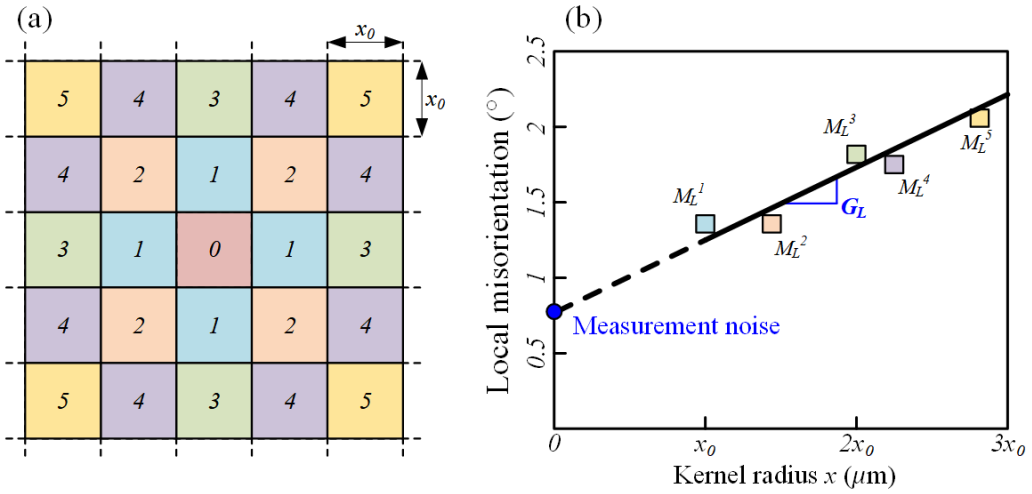

Fig. 2-8 Noise evaluation of orientation measurement by EBSD. (a) The first to fifth ordered misorientation, and (b) local misorientation versus the kernel radius, where x_0 is the scanning step size.

Substituting M_L/x_0 in Eq. (2-9) with $G_L=\partial M_L/\partial x$, we can obtain the Eq. (2-11), where the value of ρ_{GND} is unaffected by the noise.

$$\rho_{GND} = \frac{2G_L}{b} \qquad (2-11)$$

Recently, a more refined analysis of GND [21, 22] has been proposed by the calculation of the lattice curvature tensor k_{ij}, as shown:

$$k_{ij} = \begin{bmatrix} k_{11} & k_{12} & k_{13} \\ k_{12} & k_{22} & k_{23} \\ k_{31} & k_{32} & k_{33} \end{bmatrix} \qquad (2-12)$$

$$k_{ij} = \frac{\partial \theta_i}{\partial x_j} \cong \frac{\Delta \theta_i}{\Delta x_j} \qquad (2-13)$$

where $\Delta\theta$ is the difference in lattice orientation vector between measured points, which can be obtained from the EBSD data (Euler angles) and Δx the measured distance (step size). The components of k_{i3} is not accessible due to the 2D EBSD measurement, where $j = 3$ is out of the plane (surface).

Hence, only five components of Ney's dislocation tensor, a_{ij}, can be derived based on the six accessible lattice curvature tensor k_{ij}, as,

$$a_{ij} = \begin{bmatrix} a_{11} & a_{12} & a_{13} \\ a_{21} & a_{22} & a_{23} \\ a_{31} & a_{32} & a_{33} \end{bmatrix} = \begin{bmatrix} - & k_{21} & k_{31} \\ k_{12} & - & k_{32} \\ - & - & -k_{11} - k_{22} \end{bmatrix} \qquad (2-14)$$

The dislocation density tensor denotes the deformed states caused by all possible types in the crystalline lattice, shown below [17],

$$a_{ij} = \sum_{t=1}^{N} \rho_G^t b_i^t l_j^t \qquad (2-15)$$

where, b_i^t the Burgers vector, and l_j^t the line vector of the dislocation type *t*. *N* the total type of dislocations, and there are 36 dislocation configurations (24 edge dislocations and 12 screw dislocations) in the FCC lattice.

Since only five components of a_{ij}, as shown in Eq. (2-14), are accessible, the 36 unknown parameters ρ_G^t are becomes underdetermined. Hence, more constraints are needed. Pantleon [21] assume that dislocation slip in the most suitable way (5 most prevalent dislocation configurations), which caused the energy costs are minimum, as: $\rho_G = \sum_{t=1}^{36} \rho_G^t \approx min \sum_{t=1}^{5} \rho_G^t$. Therefore, the GND density was estimated.

3. Grain orientation spread analysis

To examine the effect of HDPEC on the crystalline characteristics of each sample, the grain orientation spread (GOS) method was used [23]. GOS is a numerical value representing the mean orientation change of each point in one grain, as shown in Eq.

(2-16). The schematic diagram is shown in Fig. 2-9.

$$GOS = \frac{\sum_{i,j=1}^{n} \theta(p_i, p_j)(i \neq j)}{n(n-1)} \qquad (2-16)$$

where $\theta(p_i,p_j)$ represents the misorientation between p_i and p_j within one grain. n the number of the measured points in one grain.

Hence, the GOS value of a recrystallized grain is lower than that of a deformed grain. In this study, we select 1° as the threshold value, which means the GOS value of one grain below 1° is considered the recrystallized or undeformed grain, while larger than 1° represents the deformed grain.

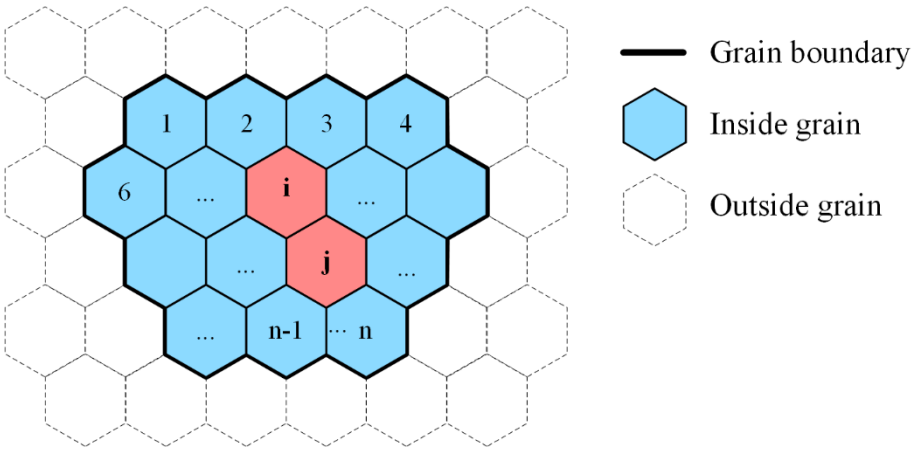

Fig. 2-9 Definition of grain orientation spread.

4. Taylor factor analysis

Taylor factor is frequently used to evaluate the flow stress in polycrystal materials regarding the critical resolved shear stress τ_{CRSS}. It is an average value that relies on the preferred orientations (texture) of materials on the assumed slip systems, which plays a vital role in examining the effect of crystalline orientation on the mechanical properties of materials [24-26].

Taylor proposed a minimum virtual plasticity energy dW_{min} and defined the Taylor factor M as [24]:

$$dW_{min} = \tau_{CRSS} \sum_{s} |\boldsymbol{\gamma}^{s}| = \sum_{i,j=1}^{3} \left|\boldsymbol{\sigma}_{ij}^{ex} \boldsymbol{\varepsilon}_{ij}^{ex}\right| = \sum_{k=1}^{3} |\boldsymbol{\sigma}_{k} \boldsymbol{\varepsilon}_{k}| \qquad (2-17)$$

$$M = \frac{dW_{min}}{|\varepsilon_1| \tau_{CRSS}} \qquad (2-18)$$

where, $\boldsymbol{\gamma}^{s}$ represents the shear strain tensor on the slip system, $\boldsymbol{\sigma}_{ij}^{ex}$ and $\boldsymbol{\varepsilon}_{ij}^{ex}$ are the stress and strain tensors of external forces, $\boldsymbol{\sigma}_{k}$ and $\boldsymbol{\varepsilon}_{k}$ denoted as the principal stress and strain tensors of the external forces, and ε_1 is the maximum principal strain.

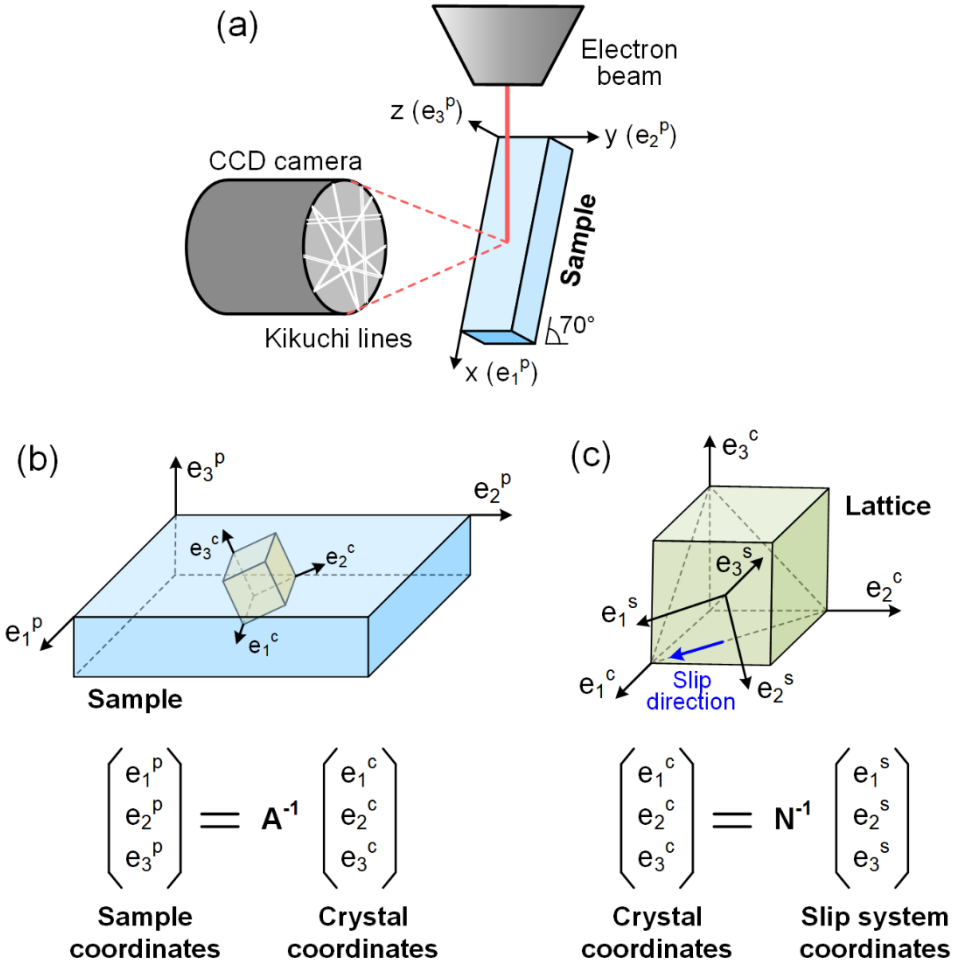

Fig. 2-10 Coordinates conversion. (a) Position of sample in EBSD system, (b) relationship between sample and lattice coordinates, and (c) relationship between lattice and slip system coordinates, where *A* and *N* represent the conversion matrix from crystal to sample coordinates and slip system to crystal coordinates.

The calculation of dW_{min} involves multi-conversion between coordinate systems, such as sample coordinates (e_1^p, e_2^p, e_3^p), crystal coordinates (e_1^c, e_2^c, e_3^c), and slip system coordinates (e_1^s, e_2^s, e_3^s). The relationship between those coordinates and coordinates conversion is shown in Fig. 2-10, where A and N represent the conversion matrix from crystal coordinates to sample coordinates and slip system coordinates to crystal coordinates, respectively. The conversion matrix A can be presented using Euler angles (φ_1, Φ, φ_2), by Eq. (2-19) shown below:

$$A = \begin{bmatrix} cos\varphi_1 cos\varphi_2 - sin\varphi_1 sin\varphi_2 cos\Phi & cos\varphi_2 sin\varphi_1 + sin\varphi_2 cos\varphi_1 cos\Phi & sin\varphi_2 sin\Phi \\ -cos\varphi_1 sin\varphi_2 - sin\varphi_1 cos\varphi_2 cos\phi & -sin\varphi_2 sin\varphi_1 + cos\varphi_2 cos\varphi_1 cos\Phi & cos\varphi_2 sin\Phi \\ sin\varphi_1 sin\Phi & -cos\varphi_1 sin\Phi & cos\Phi \end{bmatrix} \quad (2-19)$$

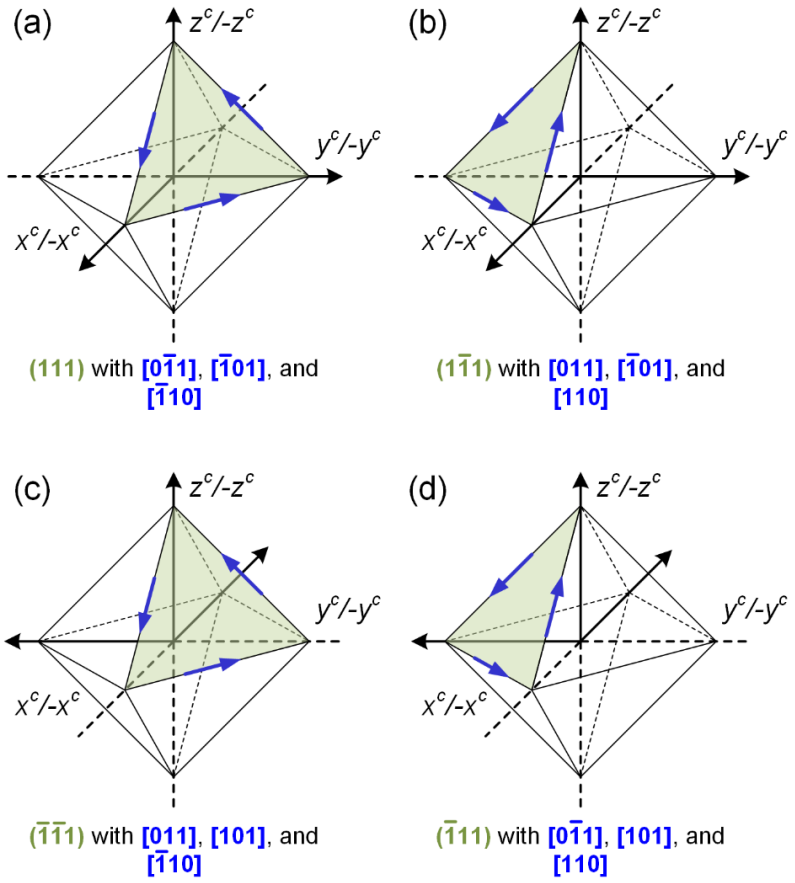

Fig. 2-11 Coordinates of 12 slip systems in FCC lattice. (a) (111) plane with the directions of [0$\bar{1}$1], [$\bar{1}$01] and [$\bar{1}$10], (b) (1$\bar{1}$1) plane with the directions of [011], [$\bar{1}$01] and [110], (c) ($\bar{1}\bar{1}$1) plane with the directions of [011], [101] and [$\bar{1}$10], and (d) ($\bar{1}$11) plane with the directions of [0$\bar{1}$1], [101] and [110], where x^c, y^c, z^c represent the crystal coordinates.

Moreover, the conversion matrix from slip system coordinates to crystal coordinates *N* relates to slip systems in the special lattice. The material used in this study is IN718, which possesses a faced-centered cubic (FCC) lattice structure and 12 slip systems of {111} and <101> that can be activated during deformation, as shown in Fig. 2-11. The conversion matrix *N* can be given:

$$N = \begin{bmatrix} n_{11} & n_{12} & n_{13} \\ n_{21} & n_{22} & n_{23} \\ n_{31} & n_{32} & n_{33} \end{bmatrix} \qquad (2-20)$$

where the coefficients n_{ij} $(i,j = 1\sim3)$ are listed in Table 2-3.

Therefore, after obtaining the minimum virtual plasticity energy dW_{min} and the maximum principal strain ε_1, the Taylor factor can be calculated using Eq. (2-18).

Table 2-3 The coefficients n_{ij} $(i,j = 1\sim3)$ for 12 slip systems in FCC lattice.

n_{ij}	**Plane (111)**			**Plane (1$\bar{1}$1)**			**Plane ($\bar{1}\bar{1}$1)**			**Plane ($\bar{1}$11)**		
	[0$\bar{1}$1]	[$\bar{1}$01]	[$\bar{1}$10]	[011]	[$\bar{1}$01]	[110]	[011]	[101]	[$\bar{1}$10]	[0$\bar{1}$1]	[101]	[110]
n_{11}	0	$-\frac{1}{\sqrt{2}}$	$-\frac{1}{\sqrt{2}}$	0	$-\frac{1}{\sqrt{2}}$	$\frac{1}{\sqrt{2}}$	0	$\frac{1}{\sqrt{2}}$	$-\frac{1}{\sqrt{2}}$	0	$\frac{1}{\sqrt{2}}$	$\frac{1}{\sqrt{2}}$
n_{12}	$-\frac{1}{\sqrt{2}}$	0	$\frac{1}{\sqrt{2}}$	$\frac{1}{\sqrt{2}}$	0	$\frac{1}{\sqrt{2}}$	$\frac{1}{\sqrt{2}}$	0	$\frac{1}{\sqrt{2}}$	$-\frac{1}{\sqrt{2}}$	0	$\frac{1}{\sqrt{2}}$
n_{13}	$\frac{1}{\sqrt{2}}$	$\frac{1}{\sqrt{2}}$	0	$\frac{1}{\sqrt{2}}$	$\frac{1}{\sqrt{2}}$	0	$\frac{1}{\sqrt{2}}$	$\frac{1}{\sqrt{2}}$	0	$\frac{1}{\sqrt{2}}$	$\frac{1}{\sqrt{2}}$	0
n_{21}	$\frac{2}{\sqrt{6}}$	$\frac{1}{\sqrt{6}}$	$-\frac{1}{\sqrt{6}}$	$-\frac{2}{\sqrt{6}}$	$-\frac{1}{\sqrt{6}}$	$-\frac{1}{\sqrt{6}}$	$-\frac{2}{\sqrt{6}}$	$-\frac{1}{\sqrt{6}}$	$-\frac{1}{\sqrt{6}}$	$\frac{2}{\sqrt{6}}$	$\frac{1}{\sqrt{6}}$	$-\frac{1}{\sqrt{6}}$
n_{22}	$-\frac{1}{\sqrt{6}}$	$-\frac{2}{\sqrt{6}}$	$-\frac{1}{\sqrt{6}}$	$-\frac{1}{\sqrt{6}}$	$-\frac{2}{\sqrt{6}}$	$\frac{1}{\sqrt{6}}$	$\frac{1}{\sqrt{6}}$	$\frac{2}{\sqrt{6}}$	$-\frac{1}{\sqrt{6}}$	$\frac{1}{\sqrt{6}}$	$\frac{2}{\sqrt{6}}$	$\frac{1}{\sqrt{6}}$
n_{23}	$-\frac{1}{\sqrt{6}}$	$\frac{1}{\sqrt{6}}$	$\frac{2}{\sqrt{6}}$	$\frac{1}{\sqrt{6}}$	$-\frac{1}{\sqrt{6}}$	$\frac{2}{\sqrt{6}}$	$-\frac{1}{\sqrt{6}}$	$\frac{1}{\sqrt{6}}$	$-\frac{2}{\sqrt{6}}$	$\frac{1}{\sqrt{6}}$	$-\frac{1}{\sqrt{6}}$	$-\frac{2}{\sqrt{6}}$
n_{31}	$\frac{1}{\sqrt{3}}$	$\frac{1}{\sqrt{3}}$	$\frac{1}{\sqrt{3}}$	$\frac{1}{\sqrt{3}}$	$\frac{1}{\sqrt{3}}$	$\frac{1}{\sqrt{3}}$	$-\frac{1}{\sqrt{3}}$	$-\frac{1}{\sqrt{3}}$	$-\frac{1}{\sqrt{3}}$	$-\frac{1}{\sqrt{3}}$	$-\frac{1}{\sqrt{3}}$	$-\frac{1}{\sqrt{3}}$
n_{32}	$\frac{1}{\sqrt{3}}$	$\frac{1}{\sqrt{3}}$	$\frac{1}{\sqrt{3}}$	$-\frac{1}{\sqrt{3}}$	$-\frac{1}{\sqrt{3}}$	$-\frac{1}{\sqrt{3}}$	$-\frac{1}{\sqrt{3}}$	$-\frac{1}{\sqrt{3}}$	$-\frac{1}{\sqrt{3}}$	$\frac{1}{\sqrt{3}}$	$\frac{1}{\sqrt{3}}$	$\frac{1}{\sqrt{3}}$
n_{33}	$\frac{1}{\sqrt{3}}$	$\frac{1}{\sqrt{3}}$	$\frac{1}{\sqrt{3}}$	$\frac{1}{\sqrt{3}}$	$\frac{1}{\sqrt{3}}$	$\frac{1}{\sqrt{3}}$	$\frac{1}{\sqrt{3}}$	$\frac{1}{\sqrt{3}}$	$\frac{1}{\sqrt{3}}$	$\frac{1}{\sqrt{3}}$	$\frac{1}{\sqrt{3}}$	$\frac{1}{\sqrt{3}}$

2.5.4 Surface morphology evolution and fractography

The surface morphology observation was performed on a scanning electron microscope (SEM, JSM-7200F, JEOL). The energy-dispersive X-ray spectroscopy (EDS) method was used to identify the particles in IN718, such as δ-phase, NbC particles, TiN particles, etc. The SEM backscattered electron (BSE) images were used to facilitate the observation of the particles. The BSE image is typically used to reveal different phases and provide crystallography information, relying on the different contrasts of heavy and light atoms (heavy atoms in bright and light atoms in dark colors). Hence, the particles were highlighted in the BSE images, and evolutions of which were easily being detected. Besides, the fractographic observation was also carried out on SEM.

References

[1] Clough RW, The Finite Element Method in Plane Stress Analysis, Proceedings of American Society of Civil Engineers, 23 (1960) 345-37.

[2] P.-O. Persson, G. Strang, A Simple Mesh Generator in MATLAB, SIAM Review, 46 (2004) 329-345.

[3] P.-O. Persson, Mesh Generation for Implicit Geometries, Ph.D. thesis, Department of Mathematics, MIT, (2004).

[4] D. Tabor, G.I. Taylor, A simple theory of static and dynamic hardness, Proceedings of the Royal Society of London. Series A. Mathematical and Physical Sciences, 192 (1948) 247–274.

[5] P. Zhang, S.X. Li, Z.F. Zhang, General relationship between strength and hardness, Materials Science and Engineering: A, 529 (2011) 62–73.

[6] Abraham. Savitzky, M.J.E. Golay, Smoothing and Differentiation of Data by Simplified Least Squares Procedures., Anal. Chem., 36 (1964) 1627–1639.

[7] B. Eigenmann, E. Macherauch. X-ray investigation of stress states in materials. Mat. -wiss. u. Werkstofftech. 27, 426–437, 491-501 (1996).

[8] Hauk V. Structural and residual stress analysis by nondestructive methods, Elsevier, 139-152, (1997).

[9] Ungar T, Ott S, Sanders PG, Brobely A, Acta Mater., 46 (1998) 3693-9.

[10] Ungar T, Dragomir I, Revesz A, Borbely A. J Appl Cryst., 32 (1999) 992-1002.

[11] Takashi Shintani, Yoshinori Murata. Evaluation of the dislocation density and dislocation character in cold rolled Type 304 steel determined by profile analysis of X-ray diffraction, Acta Materialia, 59 (2011) 4314-4322.

[12] T. Ungár, I. Dragomir, Á. Révész and A. Borbély. The contrast factors of dislocations in cubic crystals: the dislocation model of strain anisotropy in practice. JOURNAL OF APPLIED CRYSTALLOGRAPHY, 32 (1999) 992-1002.

[13] M. Kamaya, A.J. Wilkinson, J.M. Titchmarsh, Measurement of plastic strain of polycrystalline material by electron backscatter diffraction, Nuclear Engineering and Design, 235 (2005) 713–725.

[14] L.N. Brewer, M.A. Othon, L.M. Young, T.M. Angeliu, Misorientation mapping for visualization of plastic deformation via electron back-scattered diffraction, Microscopy and Microanalysis, 12 (2006) 85–91.

[15] M. Kamaya, Measurement of local plastic strain distribution of stainless steel by electron backscatter diffraction, Material Characterization, 60 (2009) 125–132.

[16] Masayuki Kamaya. Assessment of local deformation using EBSD: Quantification of accuracy of measurement and definition of local gradient. Ultramicroscopy, 111 (2011) 1189–1199.

[17] Nye, J.F. Some geometrical relations in dislocated crystals. Acta Metallurgica, 1(2) (1953) 153–162.

[18] Gao H, Huang Y, Nix W D, J. Mech. Phys. Solids, 47 (1999) 1239.

[19] Kubin L and Mortensen A, Scripta Mater., 48 (2003) 119.

[20] Liu Q, Juul Jensen D, Hansen N, Acta Mater., 46 (1998) 5819.

[21] W. Pantleon, Resolving the geometrically necessary dislocation content by conventional electron backscattering diffraction, Scripta Materialia, 58 (2008) 994–997.

[22] O. Muránsky, L. Balogh, M. Tran, C.J. Hamelin, J.-S. Park, M.R. Daymond, On the measurement of dislocations and dislocation substructures using EBSD and HRSD techniques, Acta Materialia, 175 (2019) 297–313.

[23] F.J. Humphreys, Grain and subgrain characterisation by electron backscatter diffraction, J. Mater. Sci., 36 (2001) 3833–3854.

[24] T. G.I., Plastic strain in metals, Journal of the Institute of Metals, 62 (1938) 307–324.

[25] H.J. Bunge, Some applications of the Taylor theory of polycrystal plasticity, Krist. Techn., 5 (1970) 145–175.

[26] H. Mecking, U.F. Kocks, C. Hartig, Taylor factors in materials with many deformation modest, Scripta Materialia, 35 (1996) 465–471.

Chapter 3 Effect of HDPEC on strain-hardening relief in deformed IN718

3.1 Introduction

This chapter aims to investigate the effect of HDPEC on the strain hardening of pre-deformed IN718 and examine the microstructure evolution of the strain-hardening relief induced by HDPEC treatment. A systematic and detailed investigation was carried out on the strain-hardening relief of pre-deformed IN718 with various HDPEC treatments, and the reason for strain-hardening relief induced by HDPEC was clarified. Finally, a discussion of strain-hardening relief and microstructure evolution caused by HDPEC was carried out, and the summary of this chapter was given.

3.2 Experimental approach

First of all, the tensile test was used to introduce a pre-strain, as an example, 20.5% (about 50% of the plastic strain at the breaking point, denoted by 50% ε_p) into the samples. Then, the HDPEC treatment was performed on the pre-strained samples, and as a comparison with the HDPEC-treated samples, the fully annealing case was also carried out. The research plan of this chapter is listed in Table 3-1. The sample INT represents the initial case without pre-strain and HDPEC treatment, and the S0 is the pre-strained sample. The samples S1-S3 are first pre-strained and then HDPEC-treated at the condition of 300 A/mm^2 with 3 pulses, and the duration times of each pulse are 13.33 ms, 16.67 ms, and 20 ms, respectively. Hence, the total treatment times of each sample are 40 ms, 50 ms, and 60 ms. The time interval t_{int} between each pulse is 1 s. The sample FA is the fully annealed sample, which is considered for the comparative case.

The temperature changes during the HDPEC treatment were investigated by

thermal sensors and FEM simulation. The mechanical properties (e.g., strength, ductility, and hardness) were measured to estimate the effects caused by HDPEC. Furthermore, the evolution of residual stress and dislocation density was studied using the XRD measurement. The investigation of microstructure evolution of each sample was carried out using the EBSD technique, and the surface morphology and fractography were observed by SEM. Moreover, the strain-hardening characteristics of IN718 were investigated, and the relief of strain hardening induced by HDPEC treatment was presented.

Table 3-1 Samples and treatment conditions used in this chapter.

Sample	Pre-strain	Conditions of HDPEC treatment
INT	--	--
S0	50% ε_p	--
S1	50% ε_p	300 A/mm^2, 13.33 ms × 3 pulses, t_{int} = 1 s
S2	50% ε_p	300 A/mm^2, 16.67 ms × 3 pulses, t_{int} = 1 s
S3	50% ε_p	300 A/mm^2, 20 ms × 3 pulses, t_{int} = 1 s
FA	50% ε_p	Fully annealing (954 ℃, 1 hour, Air cooling)

3.3 Temperature results by measurement and FEM simulation

The measured and simulated temperature curves of the HDPEC-treated samples are presented in Fig. 3-1. The HDPEC treatment of each sample contains 3 pulses with a different duration time of 13.33 ms, 16.67 ms, and 20 ms, respectively, as presented in Fig. 3-1(a). The temperature curves by measuring and simulating were illustrated in Fig. 3-1(b), and the enlarged image was given in Fig. 3-1(c). The simulated curves show the same tendency as the measured results, but there are still some differences. Firstly, for samples S1 and S2, the maximum temperature at each pulse matched and reached approximately 900°C and 1050°C, respectively. In contrast, sample S3 shows a large discrepancy between measurement and simulation results in the last pulse, as

shown in Fig. 3-1(c) and Table 3-2, where the maximum temperature by simulation reached 1238°C and only 1143°C for the measurement. The measured temperature tends to be lower than the simulated result in sample S3, which may be caused by the microstructure evolution during the treatment of the HDPEC. The microstructure evolution may lead to the change of electrical and thermal properties, which have been confirmed by subsequent studies. In addition, the cooling rate of the measured results was more rapid than the simulated results, which means the thermal is dissipated more quickly. The reason may be attributed to the FEM model ignoring the heat dissipation due to the thermal radiation.

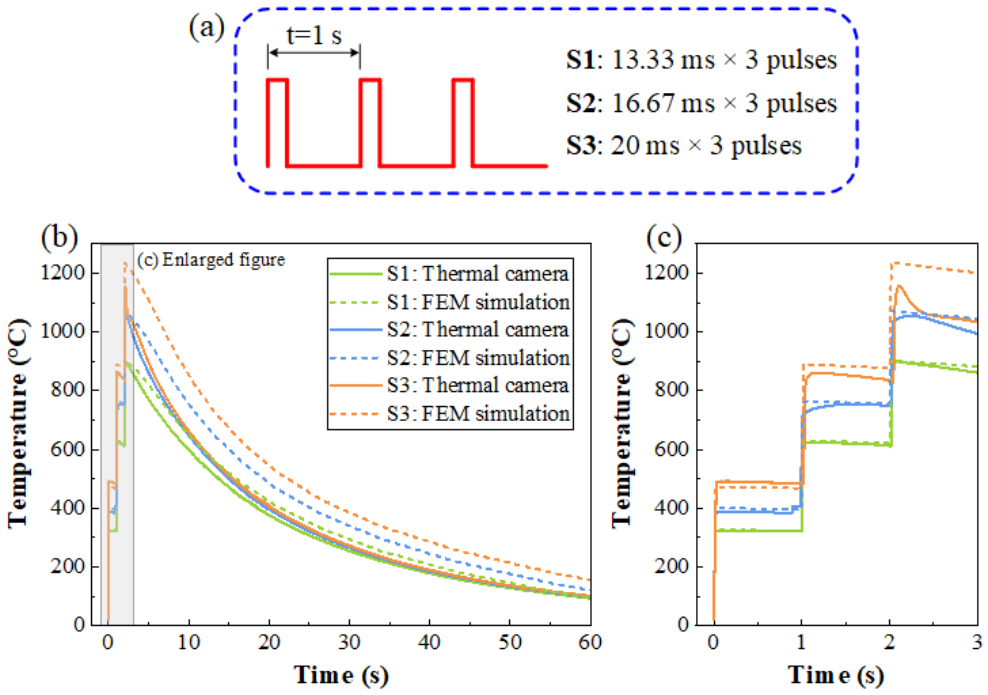

Fig. 3-1 Temperature measurement of HDPEC-treated samples. (a) Schematic diagram of pulsed current, (b) temperature curves by thermal sensors and FEM simulation, (c) enlarged figure in (b).

Moreover, the maps of FEM simulation results, including the FEM model, current density field, and temperature field, were presented in Fig. 3-2. The quadrilateral element was applied to the tensile sample, and the FEM model contains 199 Nodes

and 156 Elements. The maximum current density appeared in the tensile part with a maximum value of 300 A/mm^2. Correspondingly, the maximum temperature occurred at the center part of the sample with the maximum temperature of 901°C, 1071°C, and 1238°C, respectively. The FEM model and temperature fields of each sample are presented in Fig. 3-2.

Table 3-2 The measured and simulated temperature (°C) at the end of each pulse of all HDPEC-treated samples.

	First pulse		**Second pulse**		**Third pulse**	
	Measured T_0	Simulated T_0	Measured T_0	Simulated T_0	Measured T_0	Simulated T_0
S1	322	328	621	630	885	901
S2	384	401	720	765	1055	1071
S3	489	473	849	890	1143	1238

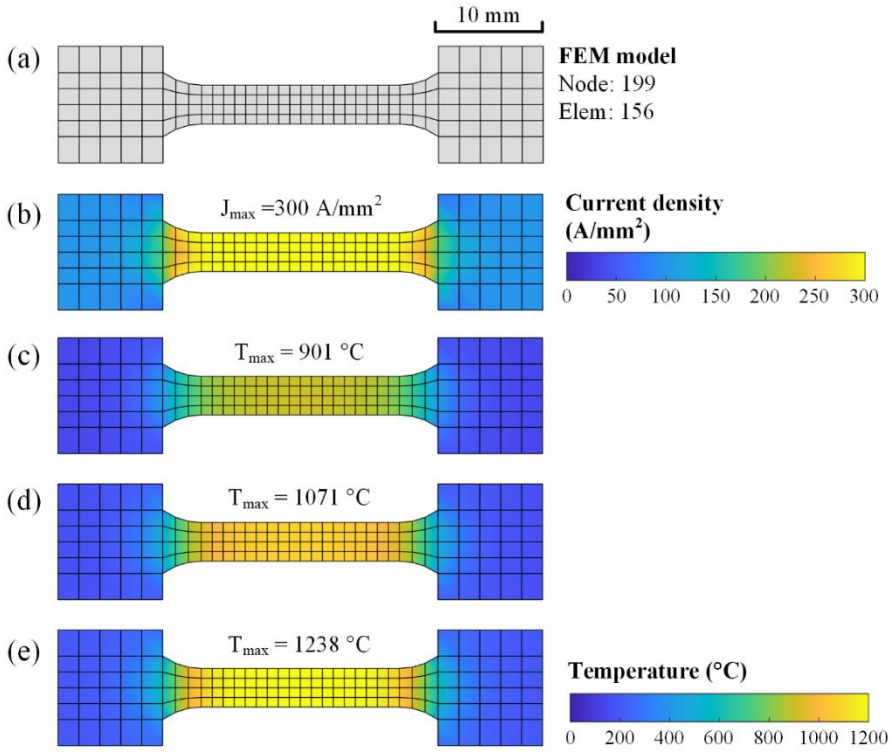

Fig. 3-2 FEM results of each sample. (a) FEM model, (b) current density field, and (c-e) temperature fields of samples S1-S3 at the maximum temperature.

3.4 Mechanical properties and residual stress

The engineering and true stress-strain curves of each sample at various treatments (the conditions of each sample are listed in Table 3-1) are shown in Fig. 3-3(a, b), and the mechanical properties of each sample are plotted in Fig. 3-3(c, d). The initial sample INT presents a good ductility of ε_f = 41.3% and yield stress of σ_y = 623 MPa. In contrast, the pre-strained sample S0 shows an evident strain-hardening with a high yield strength of σ_y = 1235 MPa but a weak elongation of ε_f = 21.3%. For HDPEC-treated samples S1-S3, the strength is restored gradually, and the elongation increases with increasing the duration time of the pulsed electric current. Thereinto, the strain hardening of HDPEC-treated sample S1 was slightly recovered, whereas sample S2 was recovered entirely, as shown in Fig. 3-3(a, b). Sample S3 shows the highest elongation, but the strength was weakened compared with sample INT. For the fully annealed sample FA, the complete recovery was obtained with a yield stress of 615 MPa and an elongation of 39.7%. The hardness shows the same tendency with the strength, as shown in Fig. 3-3(d). After pre-strain, the hardness is rapidly increased from 2.24 GPa to 3.33 GPa, and the hardness is declined gradually under the treatment of HDPEC. For the fully annealed sample FA, the hardness is decreased to 2.26 GPa.

The XRD-calculated residual stress and dislocation density of each sample is shown in Fig. 3-4. For pre-straining to around 50% ε_p strain of sample S0, the residual stress was enhanced from a relatively low value of 23 MPa to 389 MPa. And, correspondingly, the dislocation density was increased from 1.4×10^{14} to 11.4×10^{14} m^{-2}. After the HDPEC treatments, the residual stress was gradually relieved, and the dislocation density decreased correspondingly. For the current condition of 300 A/mm^2 with different treatment times of 50 ms and 60 ms of samples S2 and S3, the residual stress was almost reduced, and the dislocation density was declined to a low level. Sample FA shows the complete eliminating in residual stress and dislocation density after fully annealing.

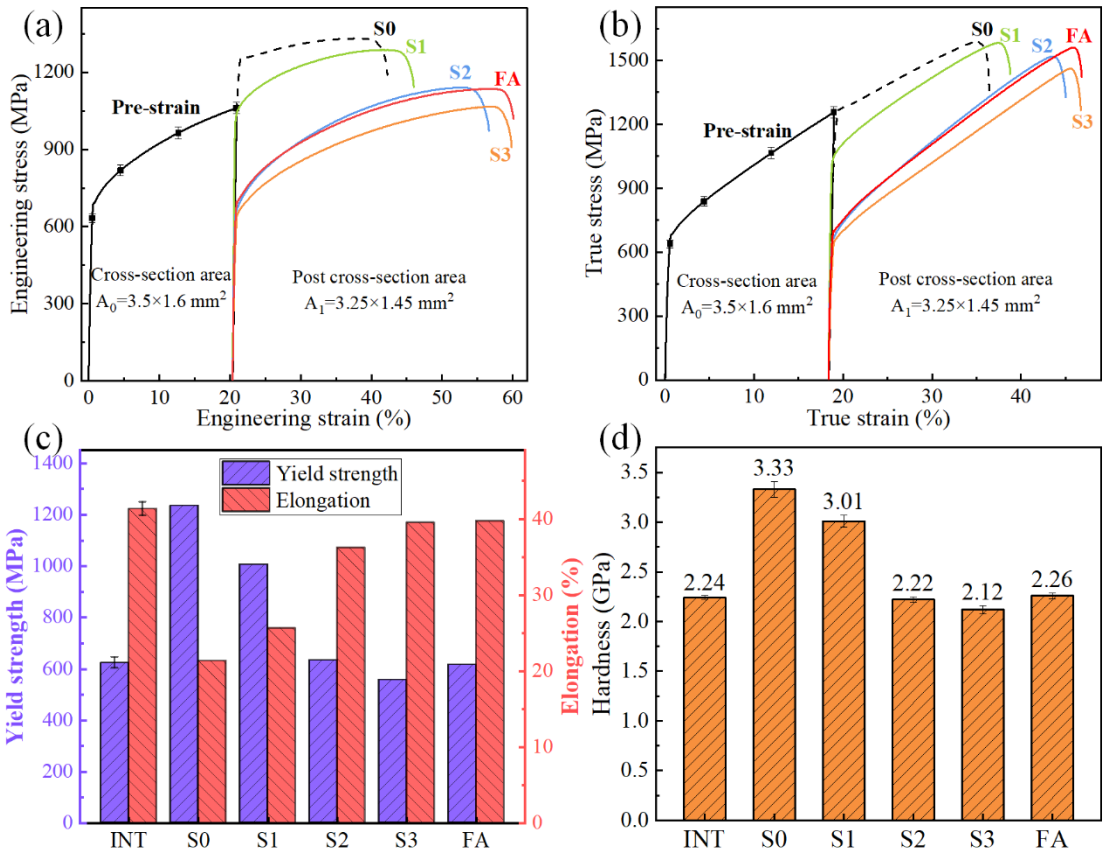

Fig. 3-3 Mechanical properties of each sample. (a) Engineering stress-strain curves and (b) true stress-strain curves of each sample, (c) plots of yield stress and elongation, and (d) plots of hardness.

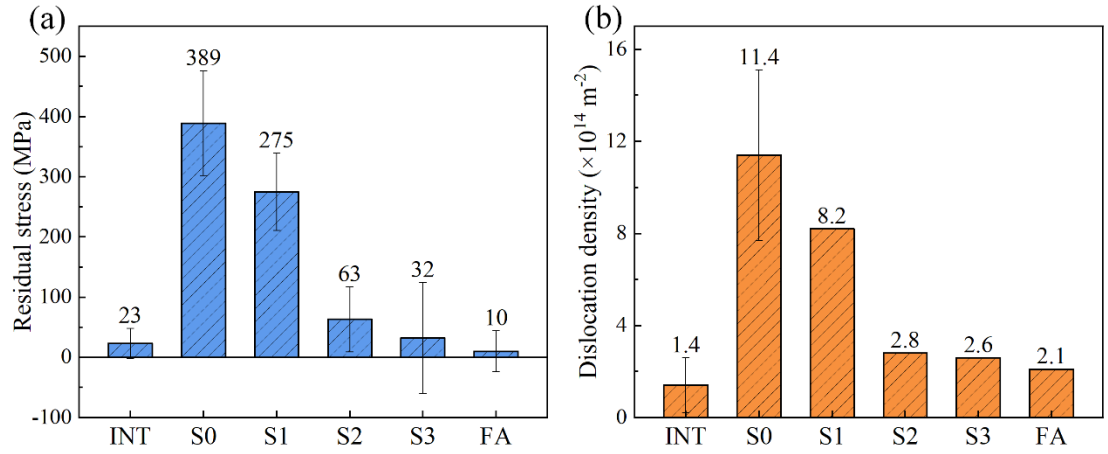

Fig. 3-4 Plots of (a) residual stress and (b) dislocation density of each sample calculated by XRD measurement.

3.5 Microstructure evolution

3.5.1 EBSD orientation maps and grain size distributions

The EBSD inverse pole figures of all samples are shown in Fig. 3-5, and the corresponding distributions of grain size with Weibull fitting [1] are also presented. The bar diagram of the mean grain size and grain aspect ratio of each sample are shown in Fig. 3-5(g-h). For the initial sample INT, the uniform grain morphology was obtained with mean grain size and grain aspect ratio of 14.5 μm and 1.86, respectively, as shown in Fig. 3-5(a). After pre-strain at the strain of 20.5% of sample S0, the elongated grains were observed with an almost unchanged grain size of 14.2 μm and an increased grain aspect ratio of 2.28, as shown in Fig. 3-5(b). After HDPEC treatment of sample S1, the deformed grain morphology was almost retained, while the grain size was refined to 11.5 μm due to some new small grains being formed, as shown in Fig. 3-5(c). Once increasing the duration time to 50 ms (sample S2), all the deformed grains were replaced by the refined and equiaxed grains with a mean grain size of 13.3 μm and an aspect ratio of 1.66, as illustrated in Fig. 3-5(d). After increasing the duration time further to 60 ms (sample S3), similar to sample S2, the uniformed and equiaxed grains were formed, while the mean grain size was increased to 15.5 μm due to the grain growth, as presented in Fig. 3-5(e). The results show that the HDPEC can gradually lead to the grain morphology evolution of deformed IN718 from local recovery to complete recovery and finally result in grain growth. For the fully annealed sample FA, the grain morphology was almost restored to the initial state of sample INT with an average grain size of 14.4 μm and grain aspect ratio of 1.85.

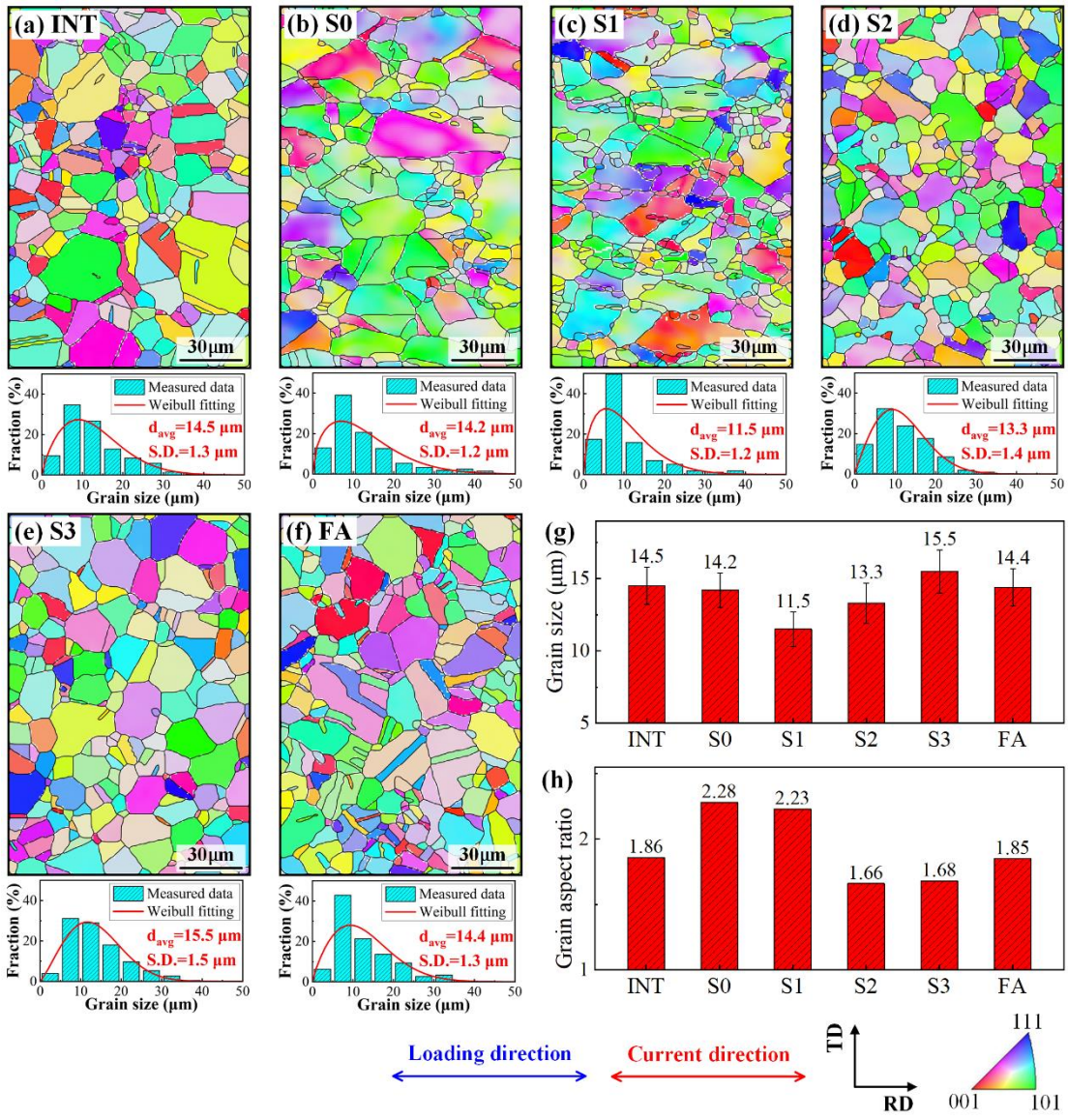

Fig. 3-5 EBSD orientation maps and grain size distributions of (a) INT, (b) S0, (c) S1, (d) S2, (e) S3, (f) FA. Mean (g) grain size and (h) grain aspect ratio of each sample. The loading and current directions are towards the horizontal. RD and TD represent the rolling and transverse directions. The EBSD maps covered a range of 120×180 μm^2 with a scanning step size of 1 μm.

3.5.2 Band contrast maps and grain boundary characteristics

The band contrast (BC) maps and grain boundary characteristics (GBC) distributions were commonly used to examine the crystalline characteristics of materials [2,3], where low angle grain boundaries (LAGBs, 3~15°) are drawn in red lines, high angle grain boundaries (HAGBs, 15°~) in black lines, and twin boundaries (TBs, 60±5°) in yellow lines. The BC maps with GBC distributions of all samples are illustrated in Fig. 3-6, and the length of each boundary is also presented.

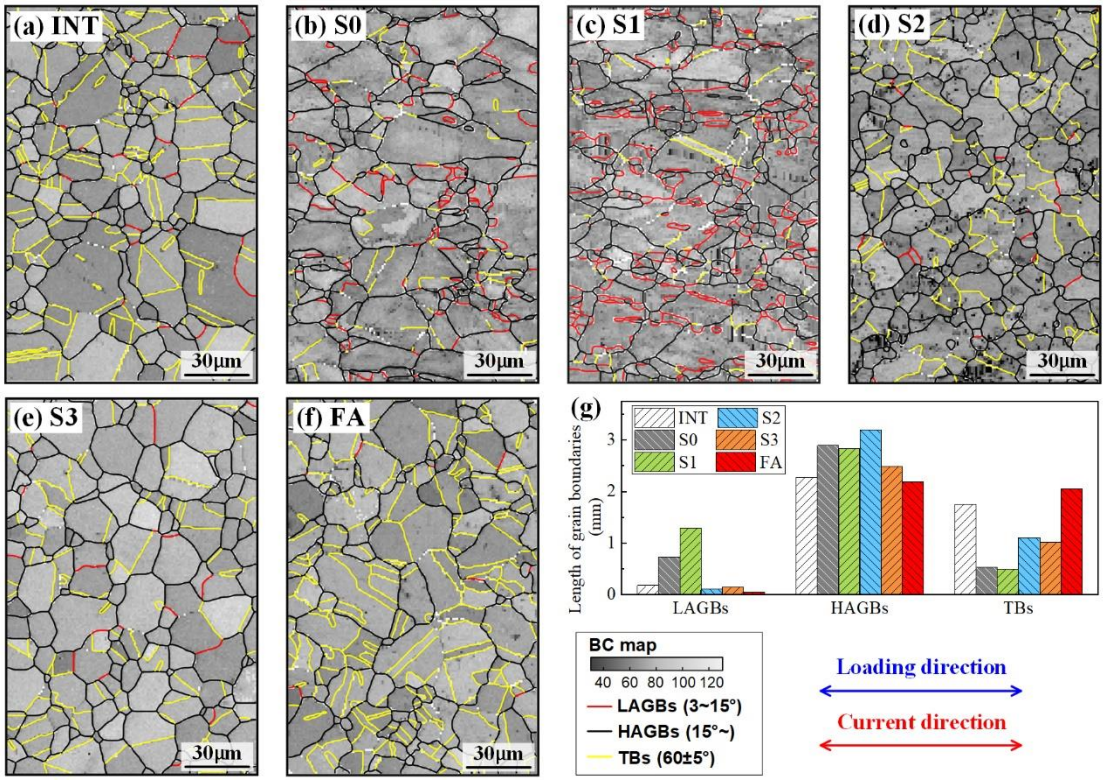

Fig. 3-6 BC maps and GBC distributions of (a) INT, (b) S0, (c) S1, (d) S2, (e) S3, (f) FA, where LAGBs are shown as red lines, HAGBs shown as black, and TBs as yellow. (g) The length of LAGBs, HAGBs, and TBs of each sample.

Sample INT shows a clear and bright BC map, as shown in Fig. 3-6(a), implying the perfect microstructure without defects was obtained due to the annealing treatment. However, the dark and blurry BC map was exhibited in sample S0 after deformation.

The darkness in the BC map is related to the low contrast of the Kikuchi bands caused by defects (e.g., dislocations) in the lattice. Since the deformation was introduced in sample S0, numerous dislocations were multiplicated and entangled and formed plenty of LAGBs [4]. Meanwhile, the TBs tend to transform to HAGBs due to dislocation entanglement, as shown in Fig. 3-6(g), where the length of TBs was decreased with the increase of HAGBs. Furthermore, after HDPEC treatment at 300 A/mm^2 and 40 ms of sample S1, the dark BC map remained, and the LAGBs were increased with the barely changes in HAGBs and TBs, as presented in Fig. 3-6(c). It is the additional LAGBs that lead to grain refinement in sample S1, as shown in Fig. 3-5. Moreover, the bright BC maps of samples S2 and S3 were observed after HDPEC treatment at 50 and 60 ms, as shown in Fig. 3-6(d,e), indicating the dislocations were eliminated by HDPEC. The length of LAGBs of samples S2 and S3 was decreased evidently, and the length of HAGBs and TBs was recovery. However, more HAGBs were observed in sample S2, indicating the grain refinement was achieved. After fully annealing, a similar microstructure was obtained in sample FA with the initial sample INT.

3.5.3 Texture and XRD spectra profiles

The {001}, {101} and {111} EBSD pole figures of each sample corresponding to the EBSD maps are presented in Fig. 3-7, and the intensity of each pole figure is shown in Fig. 3-8. Fig. 3-7 shows that all the samples present a strong {101} texture, but weak {001} and {111} orientations. The initial sample INT and pre-strained sample S0 show a strong {101} texture with a maximum intensity of 2.9 and 3.2, respectively. For the HDPEC-treated sample S1 at the current condition of 300 A/mm^2 and 40 ms, the {101} texture tends to intensify of 3.8. While for the samples S2 and S3, the {101} texture was highly alleviated with an intensity of 2.4 and 2.2, respectively. At the same time, the {001} and {111} texture of which was recovered in some degree. For

the fully annealed sample FA, the {101} texture was also relaxed to the intensity of 2.8, but the effects were weaker than the HDPEC-treated samples S2 and S3. XRD spectra profiles were shown in Fig. 3-9, and the powder diffraction of IN718, commonly considered as random orientation, was also presented. Compared with the powder diffraction, samples INT and S0 show a high (220) peak but weak (111) and (200) peaks relatively, indicating the strong {101} texture but weak {111} and {001} texture. The results show the same tendency as the EBSD results. After the HDPEC treatment, the (220) peak was gradually decreased with the increase of (111) and (200) peaks, implying the {101} texture was released. The fully annealed sample FA also shows the same tendency, while the effects were still weaker than the HDPEC-treated samples S2 and S3.

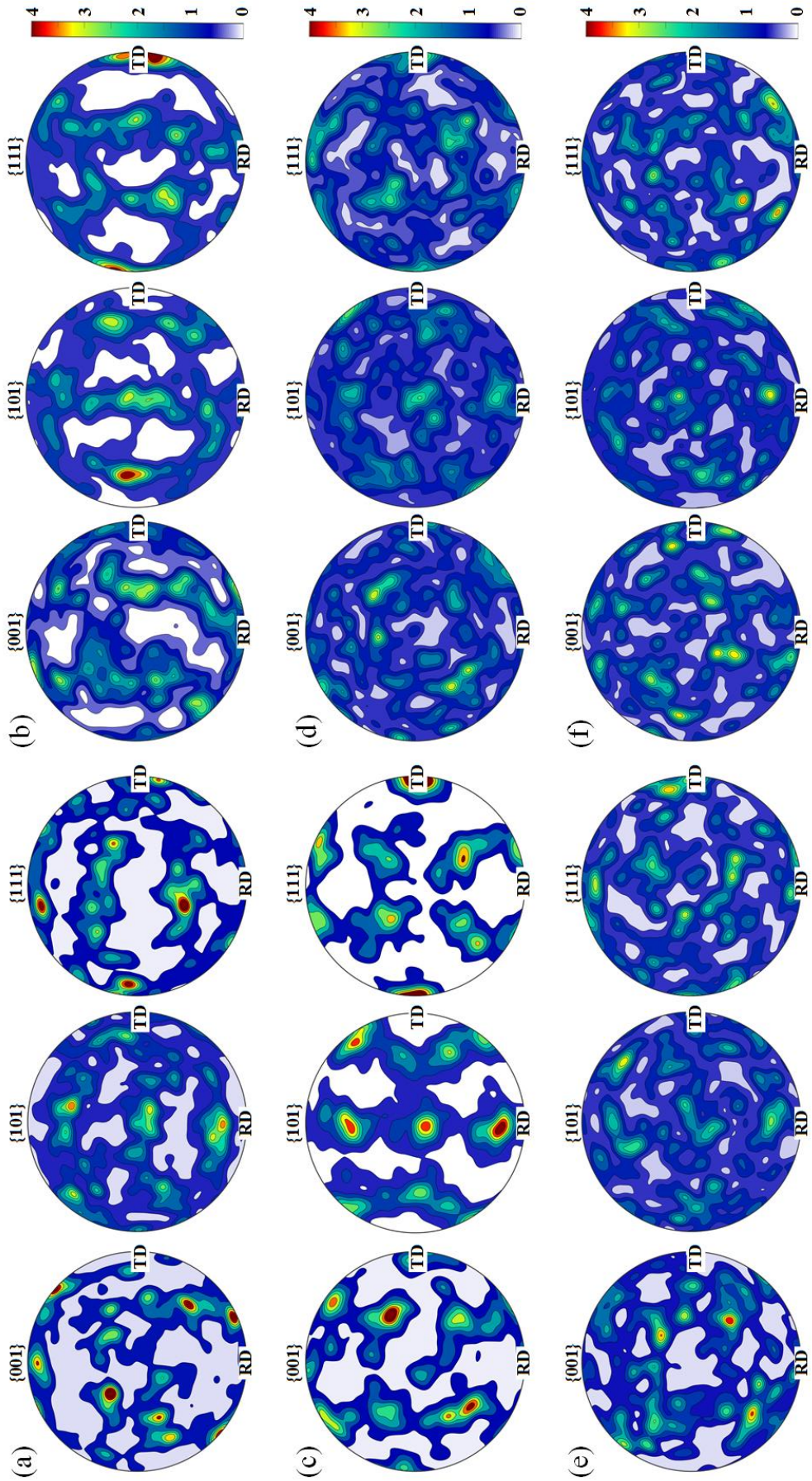

Fig. 3-7 {001}, {101} and {111} EBSD pole figures of (a) INT, (b) S0, (c) S1, (d) S2, (e) S3, and (f) FA.

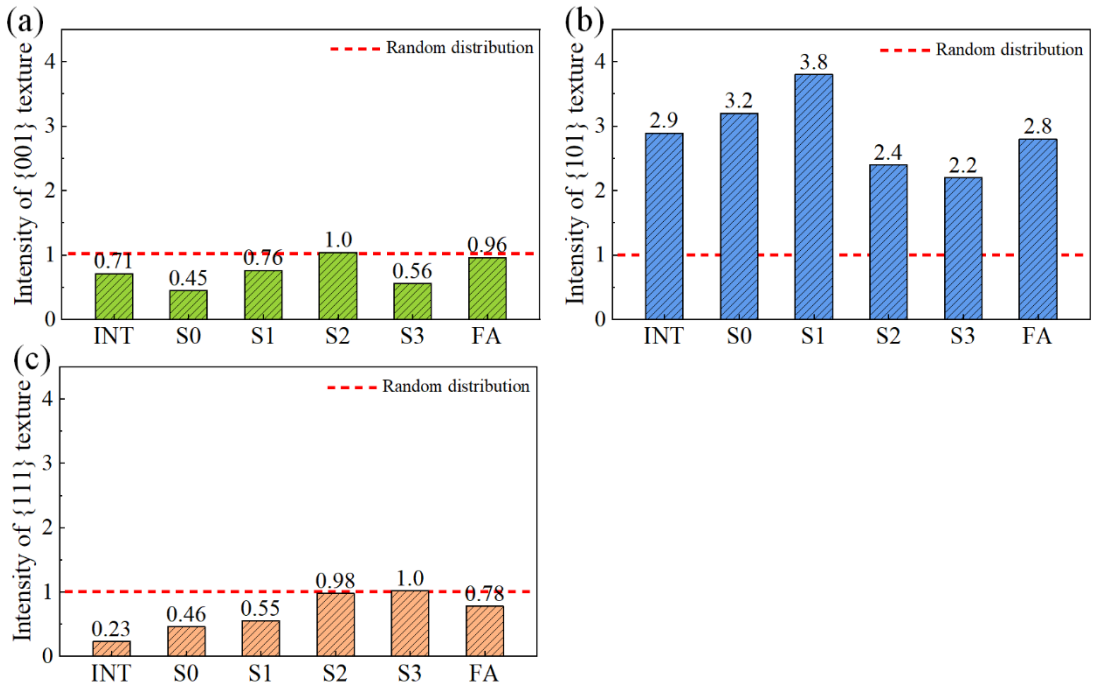

Fig. 3-8 Intensity of (a) {001}, (b) {101}, and (c) {111} texture.

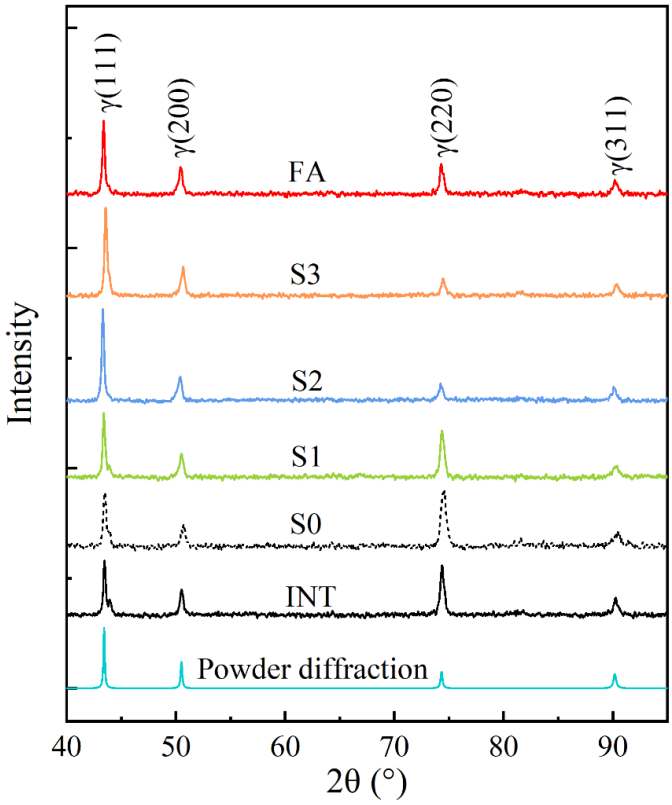

Fig. 3-9 Normalized XRD profiles of each sample.

3.5.4 Kernel averaged misorientation maps

The KAM maps of each sample corresponding to EBSD orientation maps are shown in Fig. 3-10, and the misorientation distributions of each case are also presented. The mean KAM value of each sample is shown in Fig. 3-10(g).

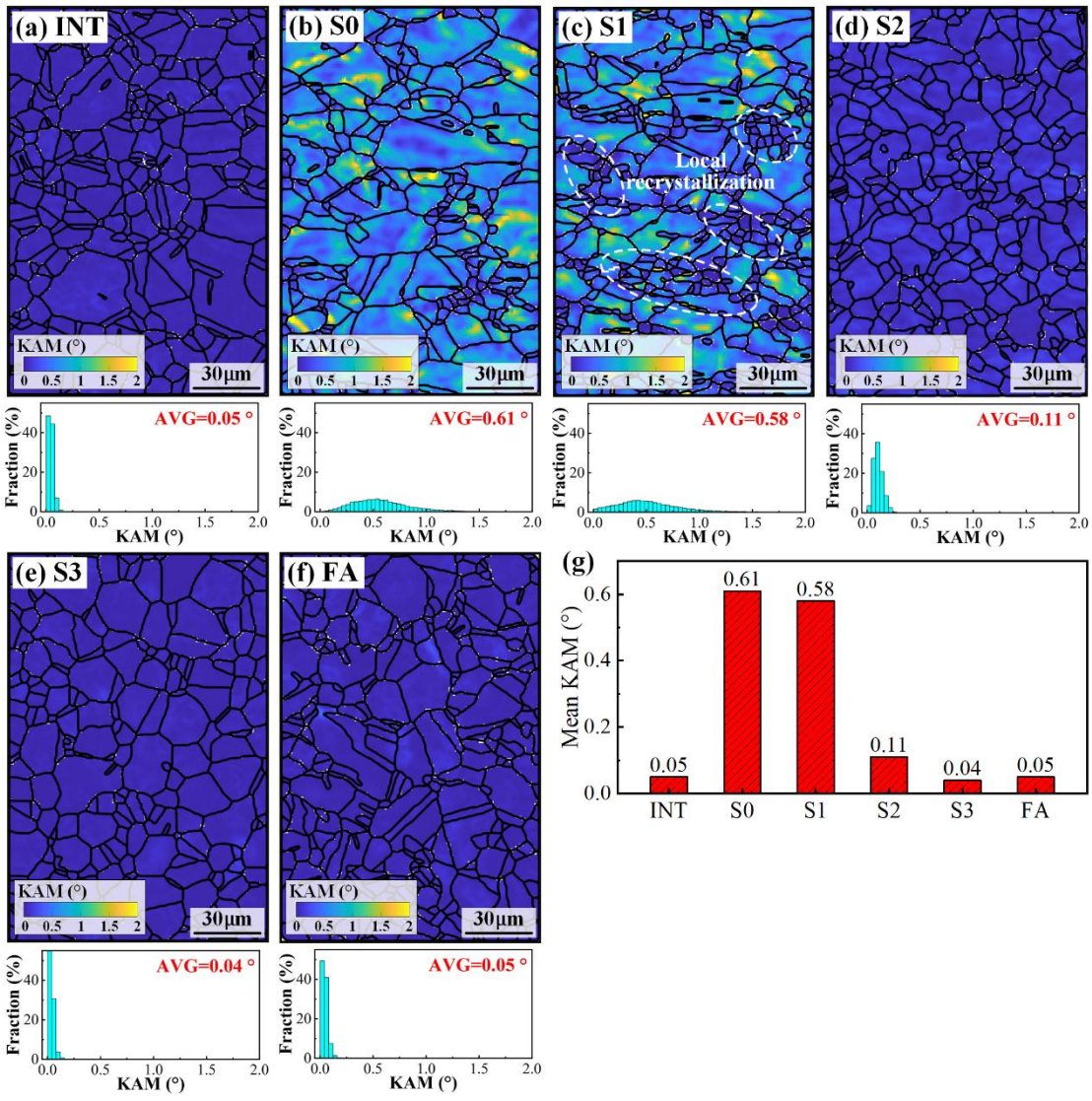

Fig. 3-10 KAM maps and corresponding misorientation distributions of (a) INT, (b) S0, (c) S1, (d) S2, (e) S3, (f) FA, and (g) mean KAM value of each sample.

Due to annealing treatment, sample INT presents a low KAM distribution with a mean value of 0.05°, indicating the uniformed grain morphology was obtained with

low defects, as shown in Fig. 3-10(a). In contrast, the colored KAM map and broadened distribution in sample S0 were observed with a mean KAM value of 0.61° due to the pre-strain with plenty of dislocations introduced, as shown in Fig. 3-10(b). After HDPEC treatment at a low duration time of 40 ms (sample S1), it was found that some small grains with blue color (low KAM value) formed, which led to the mean KAM value decreased to 0.58°, as shown in Fig. 3-10(c). Once increasing the duration time of HDPEC to 50 ms and 60 ms (samples S2 and S3), the uniformed grains with a low KAM value were observed, as shown in Fig. 3-10(d, e), indicating the dislocations were removed entirely. For the fully annealed sample FA, the same result was obtained that the KAM value was decreased to the initial level, implying the deformation was recovered completely, as shown in Fig. 3-10(f).

3.5.5 Geometrically necessary dislocation maps

Fig. 3-11 shows the GND maps and their distributions of each sample corresponding to the EBSD orientation maps. The change in the GND density of each sample presents the same tendency as the KAM results. The initial sample shows a uniform GND map with a low mean value of 0.09×10^{14} m^{-2}, while for sample S0, the colored map and broadened distribution were obtained with a mean GND density of 1.48×10^{14} m^{-2} after tensile stretch. After the HDPEC treatment of sample S1-S3, the GND density was gradually decreased to 1.37×10^{14}, 0.24×10^{14}, and 0.08×10^{14} m^{-2}, respectively. For the fully heated sample FA, the GNDs were almost removed with a mean density of 0.10×10^{14} m^{-2}.

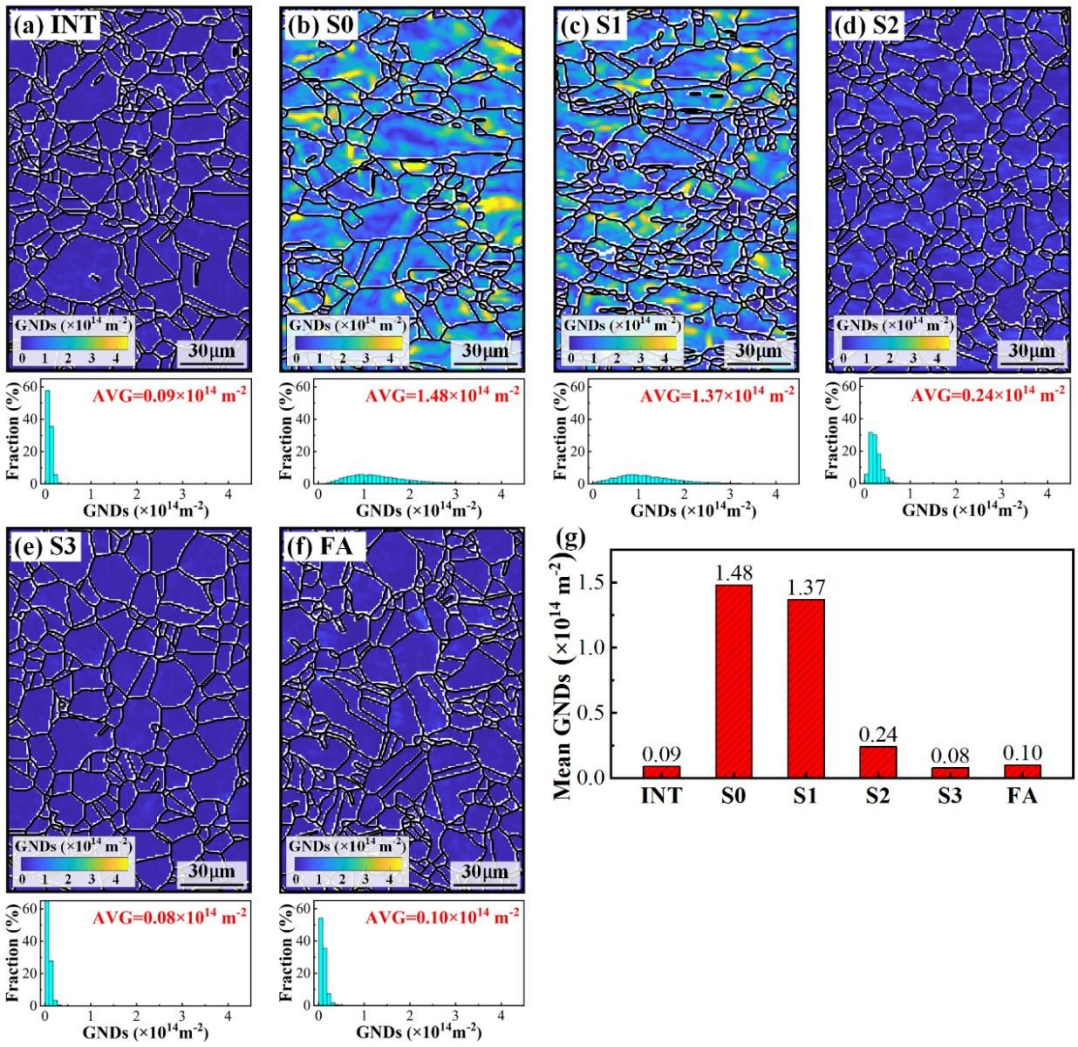

Fig. 3-11 GND maps and corresponding distributions of (a) INT, (b) S0, (c) S1, (d) S2, (e) S3, (f) FA, and (g) bar diagram of mean GND density of each sample.

3.5.6 Grain orientation spread maps

The GOS maps and the corresponding distributions of each sample are shown in Fig. 3-12, and the recovery rate of each case is also presented. In this study, one grain with a GOS value less than 1° is considered as an undeformed or defect-free grain, while the value larger than 1° represents a deformed grain. As shown in Fig. 3-12(a), the GOS map of sample INT shows a uniform blue color (low GOS value) with a recovery rate of 100%. After the tensile stretch, more than 90% of grains are deformed with a colored GOS map in sample S0, as shown in Fig. 3-12(b). However, it still has a rate of 9.8% grains that were undeformed, which may be due to the

dynamic recovery process during deformation [5]. After HDPEC treatment of sample S1, the recovery rate was increased to 22.2% with the formation of some small defect-free grains, as shown in Fig. 3-12(c). After increasing the duration time of HDPEC to 50 ms and 60 ms (samples S2 and S3), the complete recovery was obtained, as shown in Fig. 3-12(d,e). Sample FA also shows the same results that all the deformation was removed by fully annealing, as shown in Fig. 3-12(f).

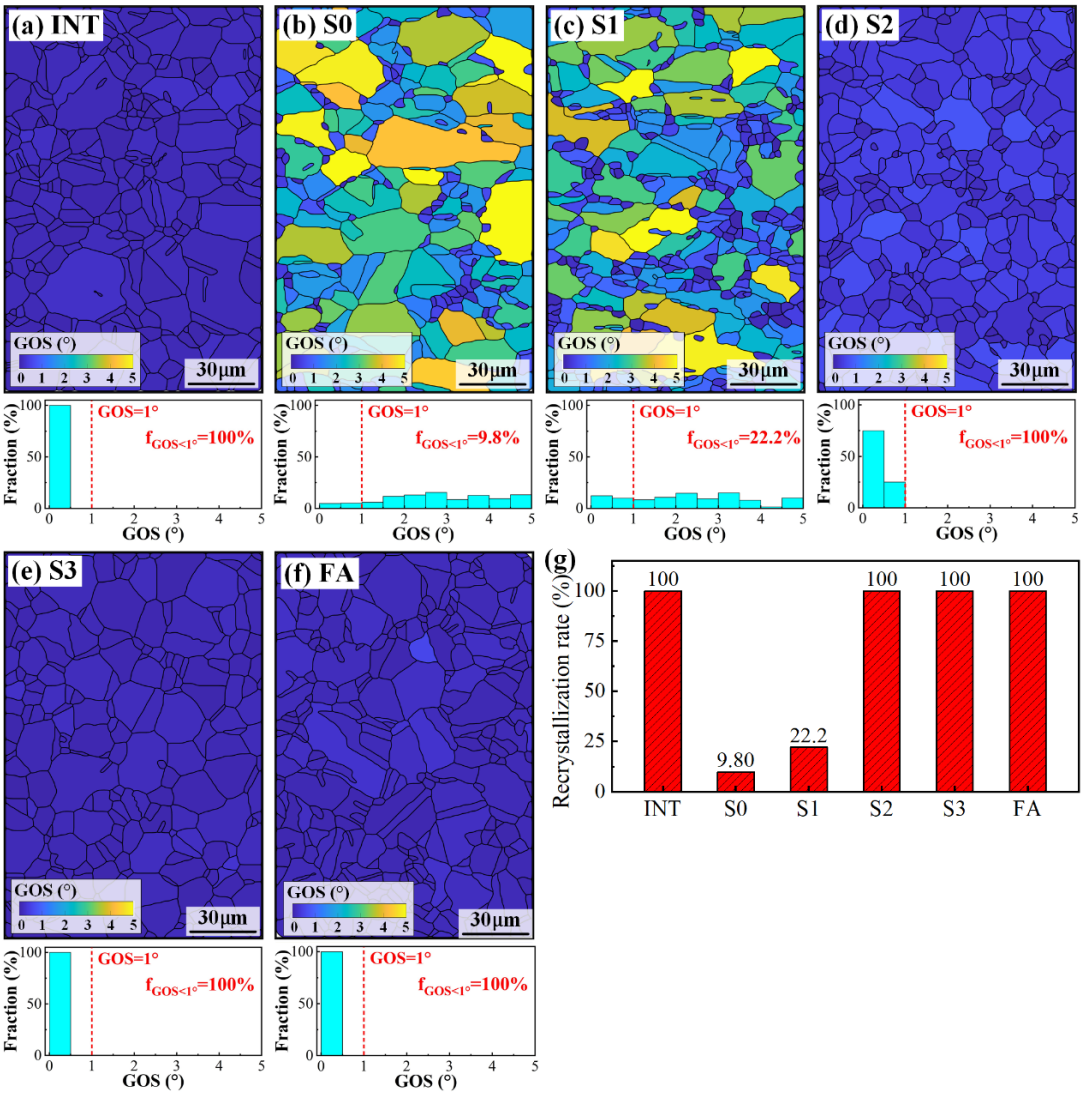

Fig. 3-12 GOS maps and the corresponding distributions of (a) INT, (b) S0, (c) S1, (d) S2, (e) S3, (f) FA, and (g) area fraction of defect-free grains of each sample, where the GOS value of one grain less than 1° is considered as the defect-free grain, and larger than 1° is deformed grain.

3.5.7 Taylor factor maps

The maps of the Taylor factor corresponding to the EBSD maps are shown in Fig. 3-13. The tensile direction towards the horizontal was used to calculate the Taylor factor. For the pre-strained sample S0, the mean Taylor factor was barely changed from 3.09 (sample INT) to 3.08. For the minor HDPEC-treated sample S1, the Taylor factor was increased to 3.13, while the value was decreased to 3.04 and 3.07 for samples S2 and S3. The mean Taylor factor of sample FA was around 3.05.

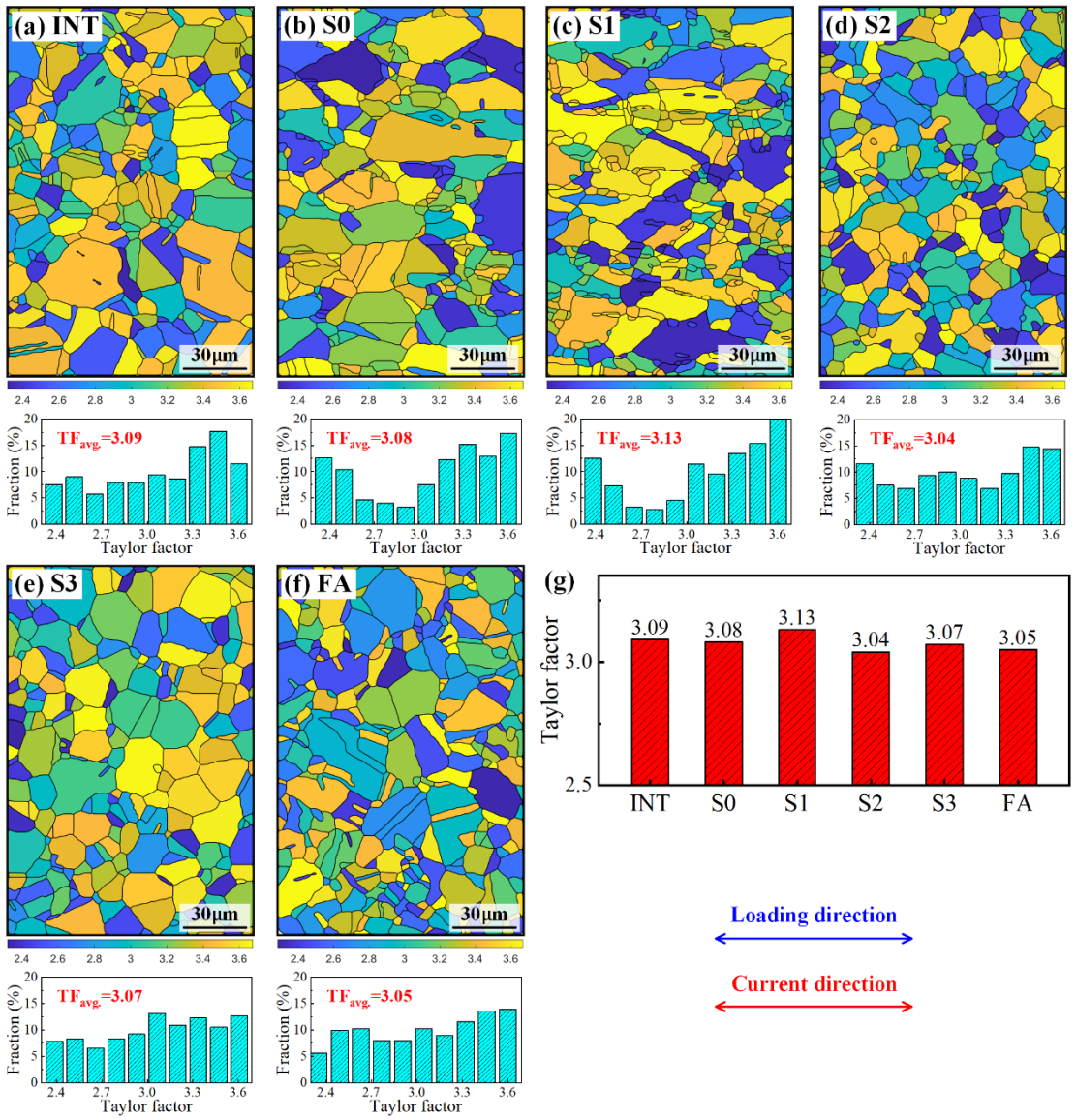

Fig. 3-13 Taylor factor maps and distributions of (a) INT, (b) S0, (c) S1, (d) S2, (e) S3, (f) FA, and (g) mean Taylor factor of each sample.

3.6 Surface morphology evolution and fractography

3.6.1 Surface morphology evolution

Fig. 3-14 shows the surface images of each sample to investigate the changes in surface morphology using the SEM backscattered electron (BSE) method. The BSE image is typically used to reveal different phases and provide crystallography information, relying on the different contrasts of heavy and light atoms (heavy atoms in bright and light atoms in dark colors).

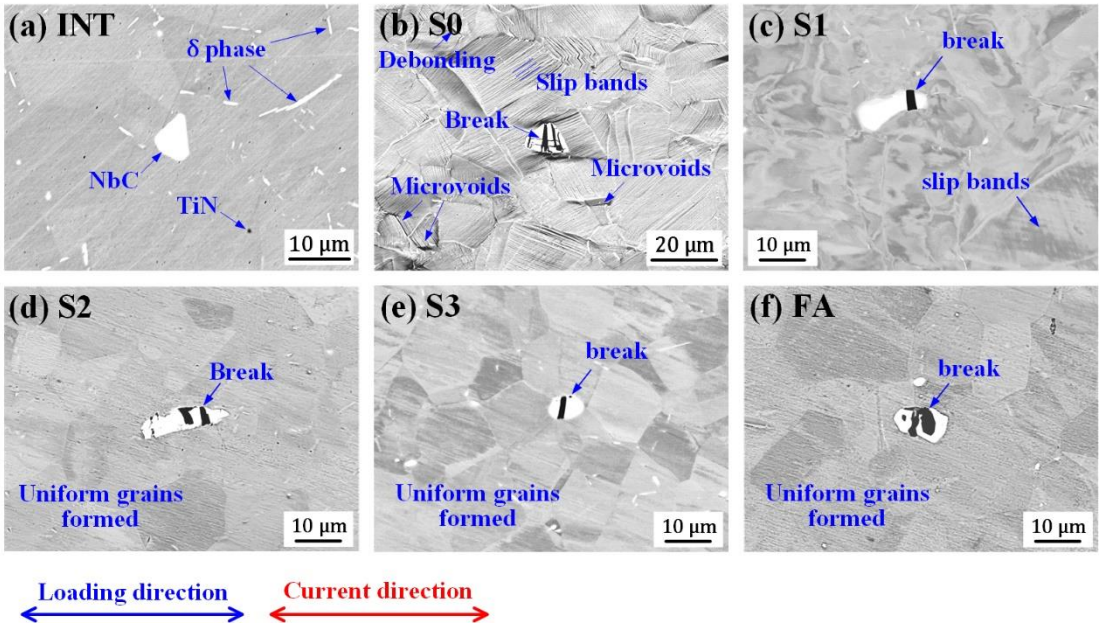

Fig. 3-14 Backscattered electron (BSE) images of (a) INT, (b) S0, (c) S1, (d) S2, (e) S3, and (f) FA. The bright particles are NbC carbide, the needle-shaped white phase δ-phase (Ni_3Nb), and the tiny dark spot the TiN particle. The directions of loading and current are towards the horizontal.

As shown in Fig. 3-14(a), the initial sample INT shows a uniform grain morphology and second-particles, which contains needle-shaped δ-phase (Ni_3Nb), NbC particles, and tiny TiN particles, identified by energy-dispersive X-ray spectroscopy (EDS). Since the element Nb is heavier than Ni and Ti is lighter than Ni,

δ-phase and NbC particles are bright while TiN particles are dark in the BSE image. After deformation, the slip bands are observed in sample S0, as shown in Fig. 3-14(b). Moreover, due to the incongruity of deformation between second-phase particles and grains, the intergranular microvoids, debonding, and broken carbides occur, as indicated in Fig. 3-14(b) using blue arrows. After applying the HDPEC at 300 A/mm^2 for 40 ms of sample S1, the broken NbC particle remained, and some slip bands are also observed, as presented in Fig. 3-14(c). After enhancing the duration time of HDPEC to 50 ms and 60 ms (samples S2 and S3), the uniformed grain morphology was obtained, as shown in Fig. 3-14(d, e). Meanwhile, the broken NbC carbides remain unhealed, and the microvoids and debonding are restored. Sample FA shows the same trend with samples S2 and S3, and the uniformed grains were formed while the broken NbC particles remained, as shown in Fig. 3-14(f).

3.6.2 Fractography

The observation of fracture characteristics of each sample is shown in Fig. 3-15. The feature of ductile fracture with plenty of dimples was observed in each sample. The size of dimples in each sample was estimated on an open-source program, ImageJ, and the bar diagram of the mean dimple size of each sample was plotted in Fig. 3-15(f). The tensile fracture surface of sample S0 presents a lot of dimples, as shown in Fig. 3-15(a), and the mean dimple diameter is 4.2 μm approximately. For sample S1 after the HDPEC treatment, the inhomogeneous dimples were surrounded by many smaller dimples, as shown in Fig. 3-15(b). Correspondingly, the averaged dimple diameter was slightly decreased to 4.0 μm. When increasing the duration time of HDPEC to 50 ms (sample S2), the homogeneous large dimples were obtained with a mean size of 6.1 μm, indicating better ductility than that of the pre-strained sample S0, as shown in Fig. 3-15(c). After increasing the duration time to 60 ms (sample S3), the average size of the dimples was increased to 7.4 μm, as shown in Fig. 3-15(d). For the

fully annealed sample FA, the homogeneous small dimples were obtained with an average value of 4.0 μm, as shown in Fig. 3-15(e).

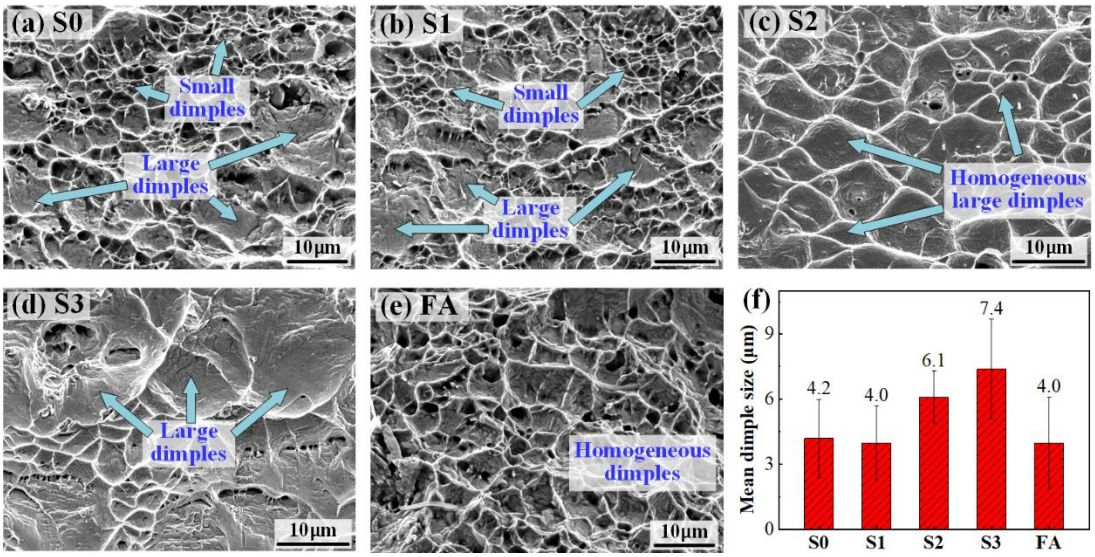

Fig. 3-15 SEM fractography of (a) S0, (b) S1, (c) S2, (d) S3, (e) FA, and (f) mean dimple diameter of each sample.

3.7 Strain-hardening relief by HDPEC

3.7.1 Strain-hardening properties of IN718

To examine the strain-hardening properties of the present material, Inconel 718, the deformed samples at the different strains of 0%, 4.1%, 12.3%, 20.5%, 28.7% and 32.8% (0%, 10%, 30%, 50%, 70% and 80% of the elongation at the breakpoint) were investigated. The flow stress and dislocation density at each strain level was shown in Fig. 3-16(a). The dislocations are rapidly multiplied at low plastic strain and mitigated when the plastic strain surpasses 50% of the total plastic strain. Since the sample needs to obey the strain rate initially, plenty of mobile dislocations are rapidly multiplied at lower strains, whereas the dislocation density maintains a stable level owing to the dislocation annihilation phenomenon [6, 7].

The plot of strength versus the square root of dislocation density was shown in Fig. 3-16(b) and marked in blue squares. The relationship between dislocation density and strength, $\sigma \propto \rho^{1/2}$, is well established by both experimental and theoretical studies. The Taylor equation is the most common equation to study the flow stress with the dislocation density [8]. After a series of deductive [9, 10], the Taylor equation can be rewritten as,

$$\sigma_y = \sigma_0 + \alpha M G b \sqrt{\rho} \qquad (3-1)$$

where σ_y and σ_0 are the yield stresses with and without initial dislocations, M is the Taylor factor, usually chosen as 3.1 for FCC metals [11], α is a constant, G is the shear modulus, taken as 74 GPa, b is the Burgers vector, taken as 0.255 nm (IN718, $\boldsymbol{b}(\mathrm{FCC}) = \frac{a}{2} < 110 >$) and ρ is the dislocation density. Figure 3-16(b) shows the plots of the strength versus dislocation density, and a regression line can be obtained in terms of Eq. (3-1) and drawn in a dashed black line. Therefore, the value of σ_0 is evaluated as 88.3 MPa, and α is 0.63, which is within a reasonable range from 0.05 to 2.6 [12].

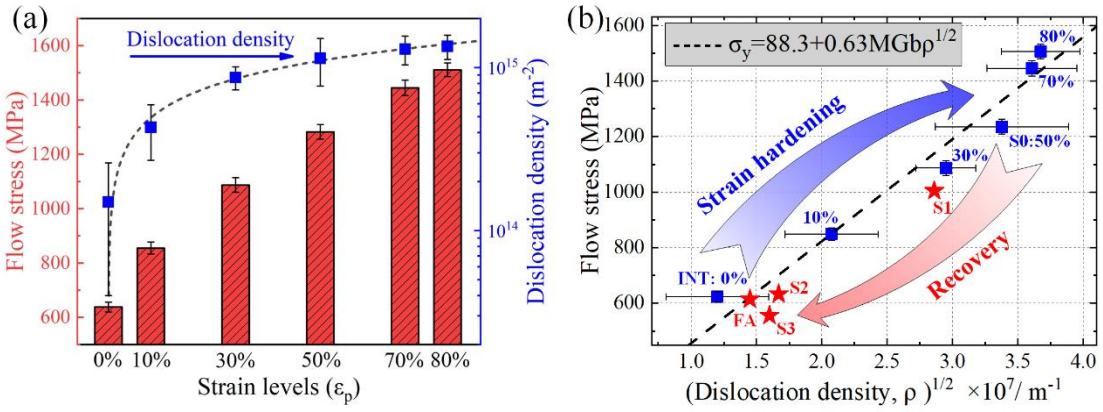

Fig. 3-16 (a) Flow stress and dislocation density change at different strain levels, and (b) plot of strength with dislocation density.

3.7.2 Relief of strain hardening by HDPEC treatment

The relationships between strength and dislocation density of the HDPEC-treated sample S1-S3 and fully annealed sample FA were also plotted in Fig. 3-16(b) and marked in red stars. The plots show that the treated samples are highly relevant to the regression lines. As shown in Fig. 3-16(b), sample S1 shows a partial relief of strain hardening, while the complete recovery is achieved for samples S2, S3, and FA.

It is well known that there are four common strategies for the strengthening of materials: strain hardening (dislocation strengthening) [8-10], solid solution strengthening [13], precipitation strengthening [14], and fine-grain strengthening [15, 16]. Moreover, material properties can also be highly affected by texture, which can lead to anisotropic properties [17-19]. In terms of the results shown above in the previous analysis, the strength change of the treated samples was related to the dislocation density, grain size, and texture, which can be described by,

$$\Delta\sigma = \Delta\sigma_d + \Delta\sigma_g + \Delta\sigma_t \qquad (3-2)$$

where $\Delta\sigma$ denotes the change of strength. The parameters $\Delta\sigma_d$, $\Delta\sigma_g$, and $\Delta\sigma_t$, are the strength changes due to dislocation density, grain size, and texture.

First of all, the strength change related to dislocation, $\Delta\sigma_d$, can be evaluated simply using the Taylor hardening law [8-10] as,

$$\Delta\sigma_d = \alpha MGb\left(\sqrt{\rho_2} - \sqrt{\rho_1}\right) \qquad (3-3)$$

where parameter α is chosen as 0.63, which is obtained from the linear fitting, shown in Fig. 3-16(b). Parameters M, G, and b are taken as 3.1 [11], 74 GPa, and 0.255 nm, respectively. The ρ_1 is the dislocation density before treatment, and ρ_2 is the value after treatment. For the case of sample S2, the dislocation density before and after HDPEC treatment are 1.14×10^{15} m^{-2} and 2.8×10^{14} m^{-2}, as shown in Fig. 3-4(b). Hence, the strength reduction due to dislocation elimination, $\Delta\sigma_d$, is approximately -628 MPa according to Eq. (3-3).

In addition, the contribution of grain size on strength change, $\Delta\sigma_g$, is estimated using the Hall-Petch relationship [15, 16],

$$\Delta\sigma_g = k\left(d_2^{-1/2} - d_1^{-1/2}\right) \quad (3-4)$$

where k is a constant, which can take 1175.93 MPa·μm$^{1/2}$ [20], and d_1 and d_2 are the grain sizes. For the case of sample S2, the grain sizes before and after the HDPEC treatment are approximately 14.2 μm and 13.3 μm, as presented in Fig. 3-5. Hence, the contribution of grain size, $\Delta\sigma_g$, is approximately 10 MPa.

Moreover, the influence of texture on the strength evolution $\Delta\sigma_t$ is expressed [19],

$$\Delta\sigma_t = (M_2 - M_1)\tau_{CRSS} \quad (3-5)$$

where M_1 and M_2 are the average values of the Taylor factor before and after HDPEC treatment. Parameter τ_{CRSS} is the critical shear stress of IN718. It can simply estimate the critical shear stress by $\tau_{CRSS}=\sigma_y/M$=201 MPa, where σ_y was taken as 623 MPa of sample INT, as shown in Fig. 3-3, and M was taken as 3.1. The Taylor factor maps and distributions of each sample are shown in Fig. 3-13. The average Taylor factor of samples S0 and S2 (before and after HDPEC treatment) were 3.08 and 3.04, respectively. Then, the decreasing value of $\Delta\sigma_t$ is -8 MPa.

The strength change caused by dislocation density and grain size were quantitatively investigated in the above text, whose contributions for sample S2 were -628 MPa, 10 MPa, and -8 MPa, and hence, the reduction in strength was 626 MPa. Moreover, the yield stress of sample S2 was reduced from 1235 MPa (sample S0) to 633 MPa according to the experimental results, as shown in Fig. 3-3(c), and the reduction is about 602 MPa, which plays a good agreement with the quantitative analysis. Hence, the strength change due to grain size and texture was small, compared with the contribution by dislocation density. Besides, the grain size was not changed heavily after the HDPEC treatment, as shown in Fig. 3-5, and so as the Taylor factor (texture evolution), as shown in Fig. 3-13. Thus, dislocation strengthening should be the dominant reason in strain hardening relief, while grain

size only has some side effects. The strength change due to dislocation density, grain size, and texture of all samples was listed in Table 3-3.

Moreover, the relief of hardness by HDPEC treatment, as shown in Fig. 3-3(d), was also related to the dislocation density, grain size, and texture. Since the tight relationship between strength and hardness, $HV \approx 3\sigma_y$, which is widely used in material science based on theoretical analyses and experimental results [21, 22]. Hence, the relief of hardness should mainly be due to the elimination of dislocation by HDPEC treatment, while the evolution of grain size and texture was the side effect.

The recovery of ductility after HDPEC treatment was mainly related to dislocation density. The pre-existed dislocations in sample S0 after deformation will impede the dislocation motion and evidently decrease the length of the free path of dislocations and thereby damage the ductility. After HDPEC treatment, all of the dislocations were removed in samples S2 and S3, and hence, the ductility was recovered.

Table 3-3 The strength changes in all samples regarding the dislocation density, grain size, and texture after HDPEC treatment.

	$\Delta\sigma_d$ /MPa	$\Delta\sigma_g$ /MPa	$\Delta\sigma_t$ /MPa	Theoretical reduction (MPa) $\Delta\sigma_d + \Delta\sigma_g + \Delta\sigma_t$	Experimental reduction (MPa)
S0	--	--	--	--	--
S1	-189	35	10	-144	-230
S2	-628	10	-8	-626	-602
S3	-650	-13	-2	-665	-679
FA	-710	-2	-6	-718	-620

The residual stress was also relieved by HDPEC treatment, as shown in Fig. 3-4(a), which may also be attributed to the dislocation removal. It is well known that the dislocations can cause the local distortion/strain of the lattice and further generate the micro residual stress. Due to residual stress originating from misfits between different regions, then they can be categorized by characteristic length: Type-1 macro-stresses vary over large dimensions of the component; Type-2 micro-stresses span grain-scale;

Type-3 form at the atomic scale [23, 24], and the equations as shown below [25],

$$\sigma_r^1 = \frac{1}{V^1}\int_{V^1} \sigma_r(x) dV^1 \quad (3-6)$$

$$\sigma_r^2 = \frac{1}{V^2}\int_{V^2} \sigma_r(x) dV^2 - \sigma_r^1 \quad (3-7)$$

$$\sigma_r^3 = \sigma_r(x) - \sigma_r^2 - \sigma_r^1 \quad (3-8)$$

where σ_r^1, σ_r^2, and σ_r^3 represent the macro, mesoscopic and micro residual stress, respectively. V^1 and V^2 denote the volumes over large dimensions of the region and grain-scale area. $\sigma_r(x)$ is the local stress.

The Eq. (3-6, 3-7, 3-8) clear depict that dislocation can raise the micro, mesoscopic and macro residual stress progressively. Hence, the high residual stress in sample S0 was due to the pre-strain that introduced high dislocation density into the sample. The residual stress was partially or fully relieved of HDPEC-treated and heat-treated samples, which may be associated with the reduction in dislocation density.

3.8 Discussion

3.8.1 Dislocation elimination and grain morphology evolution

It is well investigated theoretically and experimentally that electric current can exert a force, electron wind force (EWF), on the atoms by momentum transfer, and thereby induce the movement of dislocations [26]. Nam et al. [27] observed that the dislocation was moved enhanced by electric current in a single-crystalline nanowire by a real-time TEM observation. Furthermore, Zhang et al. [28] reported that the dislocation morphology was rearranged by an electric current with paralleling to the current direction in a quenched steel, and meanwhile, some dislocations were curved by obstacles due to the Frank-Read effect. Hence, with the promotion of EWF, the

dislocation elimination was enhanced through the combination of dipole dislocations [29] and entangled at or absorbed by grain boundaries [28, 30-32].

In this chapter, the dislocation density was eliminated gradually by HDPEC treatment, as shown in Fig. 3-4(b), measured by XRD. Moreover, the GND maps show the same tendency, as presented in Fig. 3-11, indicating that the dislocation was eliminated by HDPEC. Furthermore, the formed defect-free grains in the local area under the minor HDPEC treatment (sample S1) tend to possess the feature of LAGBs, as shown in Fig. 3-5 and 3-6, which may be related to the enhanced dislocation motion and entanglement that accumulated into LAGBs. Once the treatment time of HDPEC increased further in samples S2 and S3, all the dislocations were eliminated, as shown in Fig. 3-11, resulting in the formation of perfect grains without defects. Consequently, sample S2 shows that all the dislocations were removed, and grain refinement was achieved. In contrast, sample S3 exhibits an increase in grain size, which may be attributed to the mergence of grain boundary induced by HDPEC.

Moreover, the grains after HDPEC treatment tend to possess the random orientation and equiaxed morphology, as presented in Sections 3.5.1 and 3.5.3. The grain orientation change and equiaxed morphology may be attributed to the dislocation elimination and grain evolution promoted by HDPEC.

3.8.2 Micro-defects healing and fractographic evolution

The slip bands, microvoids, and debonding were healed by HDPEC treatment, as shown in Fig. 3-14. Since the slip band is related to the slip plane where dislocation is glided on, its healing could be due to the dislocation removal enhanced by HDPEC. Moreover, the healing of microvoids and debonding may attribute to the concentration characteristics of electric flow near the defects, which causes the local heating and local compressive force near the defects that heal and close the microvoids and debonding. Song et al. [33, 34] and Yang et al. [35] also reported that the micro-voids

or cracks introduced by pre-deformation were restored entirely after electric current treatment, and they attribute the damage-healing effect to local heating and local compressive stress around the defects according to the simulation results. Besides, the break in NbC particles remained after HDPEC treatment, which could be due to the large sizes of NbC particles and the stubborn properties of NbC.

It is well known that the dimples are associated with void and void merge during deformation[36, 37]. Due to the inconsistent deformation of matrix and particles, the microvoids and debonding may be initiated, as shown in Fig. 3-14. After continued deformation, the voids tend to merge and then cause the fracture. Qin et al. [38] reported that the dimple size is related to the grain size. Hence, more small dimples were observed in sample S1 compared with sample S0, as shown in Fig. 3-15, which may be due to the local refinement in sample S1 after HDPEC treatment, as shown in Fig. 3-5. The homogeneous and large dimples were observed in sample S2, which may be attributed to the obtained equiaxed grains after HDPEC treatment, implying the ductility was recovered. The relatively large dimples in sample S3, which may be associated with the large uniformed grains induced by HDPEC.

3.9 Summary

In this chapter, the effect of HDPEC on strain-hardening relief of deformed IN718 was investigated, and the corresponding changes in microstructure were studied. The conclusions are summarized below:

1. The strain hardening was rapidly and effectively eliminated by HDPEC treatment, and meanwhile, the ductility was recovered. Additionally, the elimination of dislocation induced by HDPEC treatment was the dominant reason, while grain size and texture evolution were the side effects in strain-hardening relief.
2. Since the dislocation was removed by HDPEC treatment, the residual stress was also alleviated.

3. The microstructure evolution caused by HDPEC first happened with some refined defect-free grains in the local area (sample S1 treated at 300 A/mm^2, 40 ms) with partial dislocation elimination. The grain boundary characteristics show that the LAGBs increased evidently in sample S1, which may be attributed to the enhanced dislocation entanglement by HDPEC. Furthermore, after increasing the treatment time to 50 and 60 ms, complete dislocation elimination was achieved with a significant decrease in LAGBs and a recovery of TBs.
4. The grain morphology of the HDPEC-treated samples tends to possess random orientation and equiaxed morphology.
5. Homogeneous dimples were obtained after HDPEC treatment in the tensile-fractured sample, and the slip bands, microvoids, and debonding were also restored.

Despite the detailed and comprehensive results obtained in this chapter, there are still several aspects of ambiguity in terms of the mechanisms. First of all, how the dislocations disappear induced by HDPEC and how the GBs evolution created, e.g., the LAGBs first increased by HDPEC and then decreased with a longer treatment time. Since the mechanical properties and microstructure of the deformed IN718 undergo dramatic changes between the treatment time from 40 ms (sample S1) to 50 ms (sample S2), the microstructure evolution induced by HDPEC is not clearly demonstrated. Hence, in Chapter 4, the quasi-in-situ EBSD observation of the microstructure evolution induced by HDPEC at the treatment time between 40 ms to 50 ms was carried out, and a detailed analysis was presented. Moreover, the unavoidable issue of how the thermal and athermal effects influence strain-hardening and which one is the dominant reason is not presented in this chapter. Since the maximum temperatures of samples S1-S3 during HDPEC treatment were varied from 800~1200°C due to the Joule Heating, as shown in Section 3.3, the thermal effect should not be ignored. Hence, this issue will also be analyzed in detail in Chapter 4.

References

[1] W. Weibull, A Statistical Distribution Function of Wide Applicability, Journal of Applied Mechanics, (1951) 293–297.

[2] S.H. Kang, H.-H. Jin, J. Jang, Y.S. Choi, K.H. Oh, D.C. Foley, X. Zhang, A Quantitative Evaluation of Microstructure by Electron Back-Scattered Diffraction Pattern Quality Variations, Microsc Microanal, 19 (2013) 83–88.

[3] Y. Wang, J. Hua, M. Kong, Y. Zeng, J. Liu, Z. Liu, Quantitative analysis of martensite and bainite microstructures using electron backscatter diffraction: MARTENSITE AND BAINITE MICROSTRUCTURES, Microsc. Res. Tech., 79 (2016) 814–819.

[4] J.A. Muñoz, R.E. Bolmaro, A.M. Jorge, A. Zhilyaev, J.M. Cabrera, Prediction of Generation of High- and Low-Angle Grain Boundaries (HAGB and LAGB) During Severe Plastic Deformation, Metall Mater Trans A. (2020).

[5] S.W. Cheong, H. Weiland, Understanding a microstructure using gos (grain orientation spread) and its application to recrystallization study of hot deformed al-cu-mg alloys, MSF. 558–559 (2007) 153–158.

[6] H. Adachi, Y. Miyajima, M. Sato, N. Tsuji, Evaluation of Dislocation Density for 1100 Aluminum with Different Grain Size during Tensile Deformation by Using In-Situ X-ray Diffraction Technique, Mater. Trans., 56 (2015) 671–678.

[7] J.C. Nieto-Fuentes, D. Rittel, S. Osovski, On a dislocation-based constitutive model and dynamic thermomechanical considerations, International Journal of Plasticity, 108 (2018) 55–69.

[8] G.I. Taylor, The mechanism of plastic deformation of crystals. Part I.—Theoretical, Proceedings of the Royal Society of London. Series A, Containing Papers of a Mathematical and Physical Character, 145 (1934) 362–387.

[9] P. Rodriguez, Sixty years of dislocations, Bull. Mater. Sci., 19 (1996) 857–872.

[10] K.M. Davoudi, J.J. Vlassak, Dislocation evolution during plastic deformation: Equations vs. discrete dislocation dynamics study, Journal of Applied Physics,

123 (2018) 085302.

[11] D. Hull, Introduction to Dislocations, 5th ed., Butterworth-Heinemann, Amsterdam, (2011).

[12] F.F. Lavrentev, The type of dislocation interaction as the factor determining work hardening, Materials Science and Engineering, 46 (1980) 191–208.

[13] J. Pelleg, Mechanical Properties of Materials, Springer Netherlands, (2013).

[14] T.H. Courtney, Mechanical Behavior of Materials: Second Edition, Waveland Press, (2005).

[15] E.O. Hall, The deformation and ageing of mild steel: III Discussion of results, Proceedings of the Physical Society. Section B, 64 (1951) 747–753.

[16] N.J. Petch, The cleavage strength of polycrystals, Journal of the Iron and Steel Institute, 174 (1953) 25.

[17] D.C. Foley, M. Al-Maharbi, K.T. Hartwig, I. Karaman, L.J. Kecskes, S.N. Mathaudhu, Grain refinement vs. crystallographic texture: Mechanical anisotropy in a magnesium alloy, Scripta Materialia, 64 (2011) 193–196.

[18] Y. Kok, X.P. Tan, P. Wang, M.L.S. Nai, N.H. Loh, E. Liu, S.B. Tor, Anisotropy and heterogeneity of microstructure and mechanical properties in metal additive manufacturing: A critical review, Materials & Design, 139 (2018) 565–586.

[19] S. Ya. Betsofen, A. A. Ilyin, V. V. Plikhunov, A. D. Plotnikov, and A. A. Filatov. Texture and Anisotropy in the Mechanical Properties of Titanium Alloys Caused by the Mechanism of Plastic Deformation. Russian Metallurgy (Metally), 2007(5), (2007) 387–393.

[20] C. Pei, D. Shi, H. Yuan, H. Li, Assessment of mechanical properties and fatigue performance of a selective laser melted nickel-base superalloy Inconel 718, Materials Science and Engineering: A, 759 (2019) 278–287.

[21] D. Tabor, G.I. Taylor, A simple theory of static and dynamic hardness, Proceedings of the Royal Society of London. Series A. Mathematical and Physical Sciences, 192 (1948) 247–274.

[22] P. Zhang, S.X. Li, Z.F. Zhang, General relationship between strength and hardness, Materials Science and Engineering: A, 529 (2011) 62–73.

[23] P.J. Withers, H.K.D.H. Bhadeshia, Residual stress. Part 1 – Measurement techniques, Materials Science and Technology, 17 (2001) 355–365.

[24] P.J. Withers, H.K.D.H. Bhadeshia, Residual stress. Part 2 – Nature and origins, Materials Science and Technology, 17 (2001) 366–375.

[25] E. Macherauch, V. Hauk, Residual Stresses in Science and Technology, DGM Informationsgesellschaft Verlag, (1987).

[26] H. Conrad, Electroplasticity in metals and ceramics, Mater. Sci. Eng. A., 287 (2000) 276–287.

[27] S.-W. Nam, H.-S. Chung, Y.C. Lo, L. Qi, J. Li, Y. Lu, A.T.C. Johnson, Y. Jung, P. Nukala, R. Agarwal, Electrical Wind Force-Driven and Dislocation-Templated Amorphization in Phase-Change Nanowires, Science, 336 (2012) 1561–1566.

[28] S. Xiang, X. Zhang, Dislocation structure evolution under electroplastic effect, Mater. Sci. Eng. A., 761 (2019) 138026.

[29] Y. Tang, A. Hosoi, Y. Iwase, Y. Ju, Effect of High-Density Electric Current on the Microstructure and Fatigue Crack Initiation of Stainless Steel, Mater. Trans., 54 (2013) 2085–2092.

[30] D. Waryoba, Z. Islam, B. Wang, A. Haque, Recrystallization mechanisms of Zircaloy-4 alloy annealed by electric current, J. Alloys Compd., 820 (2020) 153409.

[31] Y.H. Zhu, S. To, W.B. Lee, X.M. Liu, Y.B. Jiang, G.Y. Tang, Effects of dynamic electropulsing on microstructure and elongation of a Zn–Al alloy, Mater. Sci. Eng. A, 501 (2009) 125–132.

[32] L. Pan, W. He, B. Gu, Effects of electric current pulses on mechanical properties and microstructures of as-quenched medium carbon steel, Mater. Sci. Eng. A, 662 (2016) 404–411.

[33] Song H, Wang Z-J. Microcrack healing and local recrystallization in pre-

deformed sheet by high density electropulsing. Materials Science and Engineering: A, 490 (2008) 1–6.

[34] Song H, Wang Z, He X, Duan J. Self-healing of damage inside metals triggered by electropulsing stimuli. Sci Rep., 7 (2017) 7097.

[35] Yang CL, Yang HJ, Zhang ZJ, Zhang ZF. Recovery of tensile properties of twinning-induced plasticity steel via electropulsing induced void healing. Scripta Materialia, 147 (2018) 88–92.

[36] Chen Z, Butcher C. Introduction to Ductile Fracture Modelling. In: Chen Z, Butcher C (eds) Micromechanics Modelling of Ductile Fracture. Springer Netherlands, Dordrecht, (2013) pp 1–24

[37] Lubarda VA, Schneider MS, Kalantar DH, et al. Void growth by dislocation emission. Acta Materialia, 52 (2004) 1397–1408.

[38] Qin W, Li J, Liu Y, et al. Effects of grain size on tensile property and fracture morphology of 316L stainless steel, Materials Letters, 254 (2019) 116–119.

Chapter 4 Mechanisms of strain-hardening relief induced by HDPEC

4.1 Introduction

Although the detailed and comprehensive results were obtained in Chapter 3, there are still many unclear issues regarding the microstructure evolution, such as how the dislocations driven and removed by HDPEC and how the GBs change created (e.g., the length of LAGBs was decreased and that of TBs was increased after applying the HDPEC, as presented in Fig. 3.6). Since the mechanical properties and microstructure of the deformed IN718 undergo dramatic changes between the treatment time from 40 ms (sample S1) to 50 ms (sample S2), the microstructure evolution induced by HDPEC during this treatment time range is not clearly demonstrated in Chapter 3. Hence, this chapter aims to study the microstructure evolution induced by HDPEC at the treatment time between 40 ms to 50 ms using the quasi-in-situ EBSD observation.

Moreover, the contributions of thermal and athermal effects on strain-hardening relief caused by HDPEC treatment were also carried out. Since sample S2 in Chapter 3 has achieved the complete recovery of the strain hardening. Hence, two equivalent HDPEC-treated samples regarding the sample S2 with varying current density and duration times were designed, and a rapidly heated sample was also presented to clarify the thermal and athermal effects in strain-hardening relief.

4.2 Experimental approach

For in-situ EBSD observation, two samples at the current conditions of 300 A/mm^2 with 3 pulses were presented. The duration times of 13.33 ms and 15 ms of each pulse were used, respectively, denoted as samples S4 and S5, as given in Table 4-1. Hence, the total heating times of each case are 40 ms and 45 ms, respectively. The same sites

were measured by EBSD before and after HDPEC treatment. Since the surface of the EBSD samples after HDPEC treatment was covered by an oxidation layer, the surface was cleaned by ion milling.

The equivalent samples are denoted as S6, S7, and RA, respectively, as listed in Table 4-1. The equivalent sample means that a similar thermal condition (heating and cooling process) with the target sample S2. Samples S6 and S7 are the equivalent HDPEC-treated samples at the conditions of 100 A/mm^2, 150 ms × 3 pulses, and 50 A/mm^2, 600 ms × 3 pulses, respectively. Sample RA is the rapidly heated sample at 1200 ℃ for 20 s, followed by air cooling, which is the comparative test of samples S2, S6, and S7.

Table 4-1 Samples and treatment conditions used in this chapter.

Sample	Pre-strain	Conditions of HDPEC treatment	Notes
S4	50% ε_p	300 A/mm^2, 13.33 ms × 3 pulses, t_{int} = 1 s	In-situ EBSD observation
S5	50% ε_p	300 A/mm^2, 15 ms × 3 pulses, t_{int} = 1 s	In-situ EBSD observation
S6	50% ε_p	100 A/mm^2, 150 ms × 3 pulses, t_{int} = 1 s	Equivalent to sample S2
S7	50% ε_p	50 A/mm^2, 600 ms × 3 pulses, t_{int} = 1 s	Equivalent to sample S2
RA	50% ε_p	Rapid annealing (1200 ℃, 20 s, Air cooling)	Equivalent to sample S2

First of all, the temperature evaluation of the HDPEC-treated samples was carried out using thermal sensors and FEM simulation, and then their mechanical properties were also investigated. For the in-situ observation, the EBSD observation at the same places was carried out before and after HDPEC treatment. The detailed analysis, such as dislocation motion behavior, grain boundary evolution, and new grains formation, were analyzed. Moreover, the thermal and athermal effects on the strain-hardening characteristics of IN718 were quantitatively analyzed. Finally, the discussion of the effect of HDPEC, such as thermal effect, electron wind force, etc., on the dislocation motion was carried out, and the summary was given.

4.3 Temperature results by measurement and FEM simulation

The temperature-time curves of the HDPEC-treated samples S4 and S5 by measurement and simulation are shown in Fig. 4-1. The current application of samples S4 and S5 contains 3 pulses with a duration time of 13.33 ms and 15 ms, respectively, as shown in Fig. 4-1(a). The temperature-time curves by measuring and simulating were shown in Fig. 4-1(b), and the enlarged figures were shown in Fig. 4-1(c). The measured maximum temperatures at the last pulse of samples S4 and S5 are 885 and 983°C. The simulated results show the same tendency as the measured results. Fig. 4-2 shows the current density and temperature fields of the HDPEC-treated samples. The maximum temperatures of S4 and S5 are 901 and 988°C, respectively.

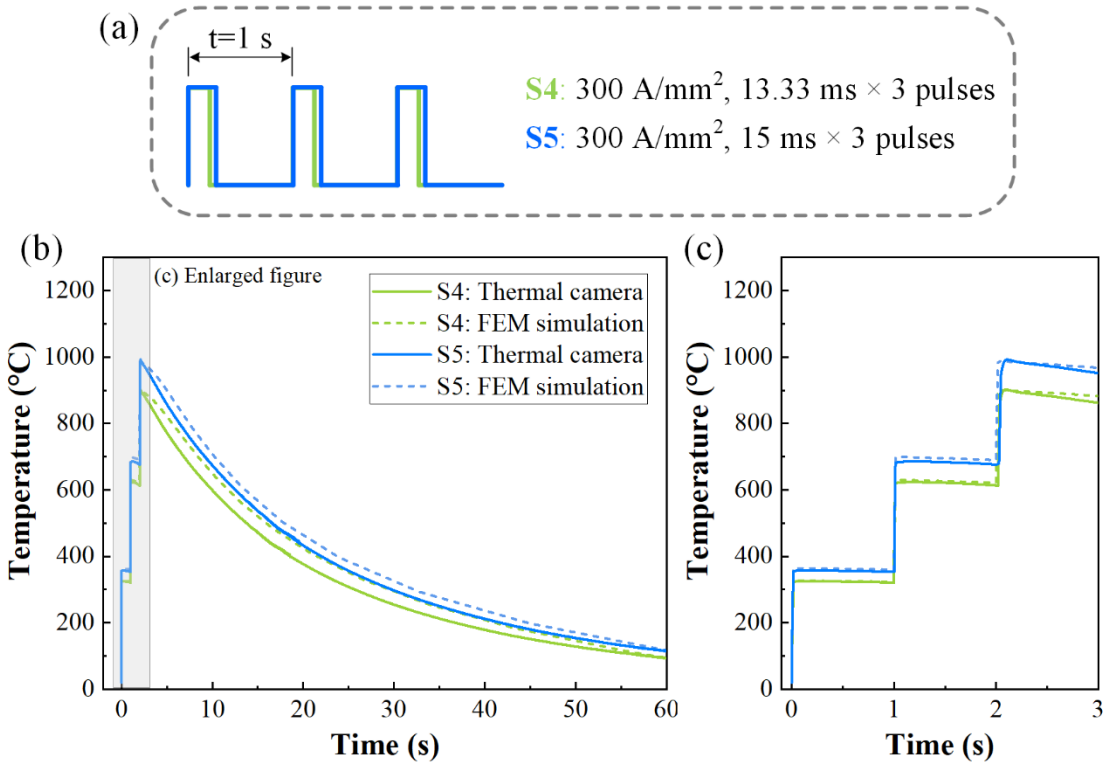

Fig. 4-1 Temperature measurement of HDPEC-treated samples. (a) Schematic diagram of pulsed current, (b) temperature-time curves by thermal sensors and simulation, (c) enlarged figure in (b).

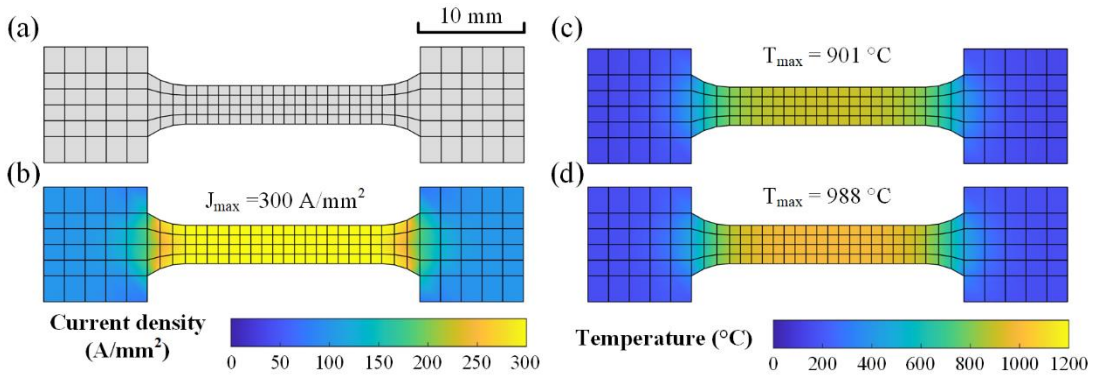

Fig. 4-2 FEM simulation results of each sample. (a) FEM model, (b) current density field, and temperature fields of (c) S4 and (d) S5 at the maximum temperature.

Moreover, for the equivalent samples, the measured and simulated temperature curves of the equivalent HDPEC-treated samples S6 and S7, and rapidly heated sample RA are shown in Fig. 4-3. Similar to sample S2, samples S6 and S7 contain 3 pulses with a duration time of 150 ms and 600 ms, respectively, as presented in Fig. 4-3(a). The temperature-time curves by measuring and simulating were shown in Fig. 4-3(b), and the enlarged figures were shown in Fig. 4-3(c). The measured maximum temperatures of samples S6 and S7 are 1044 and 1029°C, coinciding with sample S2 of 1055°C. The simulated results show the same tendency as the measured results. For the rapid annealing sample RA, a one-dimensional transient heat conduction model was used to estimate the temperature changes with time, as presented in Appendix 3. The temperature-time curve is presented in Fig. 4-3(b,c) as a dashed red line. The maximum temperature of approximately 1061 °C was achieved at the end of the heating (20 s). The heating and cooling curves of sample RA covered the HDPEC-treated samples S2, S6, and S7, as shown in Fig. 4-3(b), indicating the thermal effect of sample RA is larger than the HDPEC-treated samples.

Fig. 4-4 shows the current density and temperature fields of the HDPEC-treated samples. The maximum current density of each sample is 300, 100, and 50 A/mm^2, respectively, and the maximum temperatures are 1071, 1058, and 1049°C.

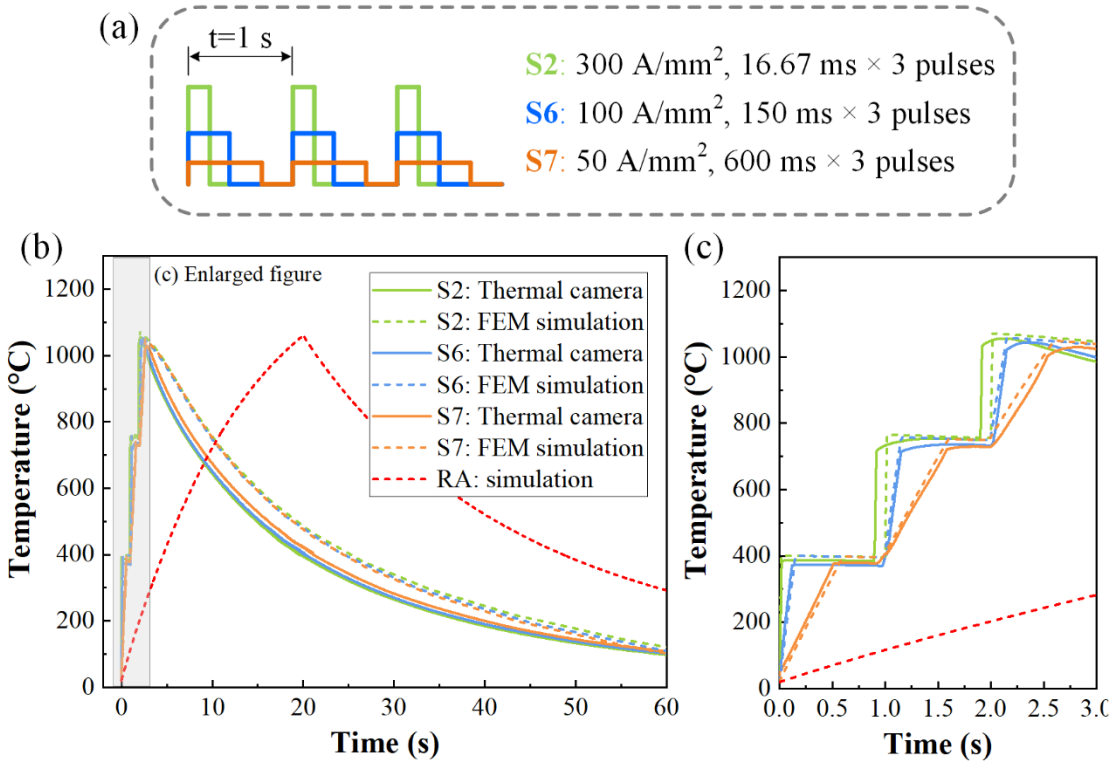

Fig. 4-3 Temperature measurement of HDPEC-treated samples. (a) Schematic diagram of pulsed current, (b) Temperature curves by thermal sensors and simulation, (c) Enlarged figure in (b).

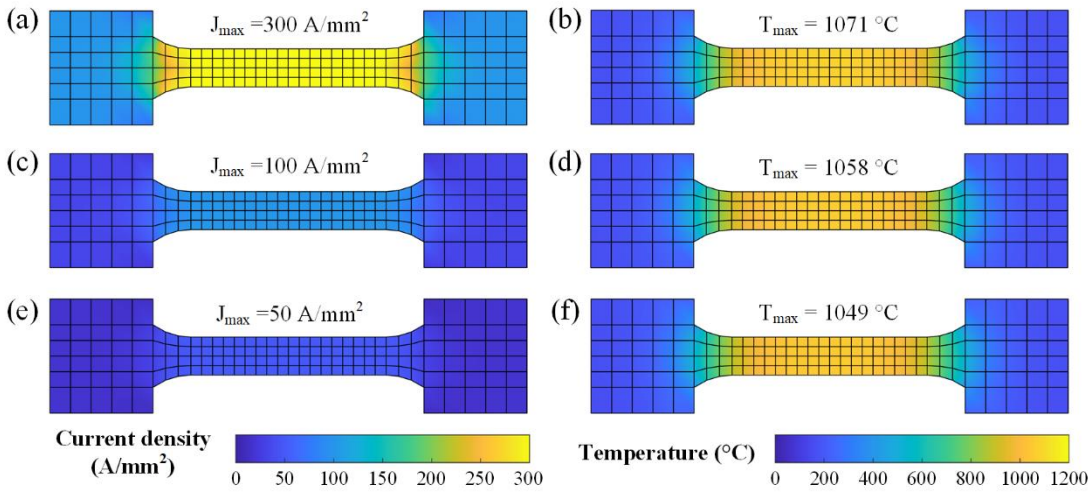

Fig. 4-4 FEM simulation results of each sample. Current density and temperature fields of (a-b) S2, (c-d) S6, and (e-f) S7.

4.4 Mechanical properties

The engineering stress-strain curves of the HDPEC-treated samples S4 and S5 are plotted in Fig. 4-5(a), and the mechanical properties of each sample are shown in Fig. 4-5(b). Compared with sample S2, samples S4 and S5 show the uncomplete strain-hardening relief. The yield strength of samples S4 and S5 are 1005 MPa, 946 MPa, respectively, indicating the strain hardening is not fully removed. As presented in Fig. 4-5(b), the elongations of samples S4 and S5 are accordingly lower than the samples S2 and INT.

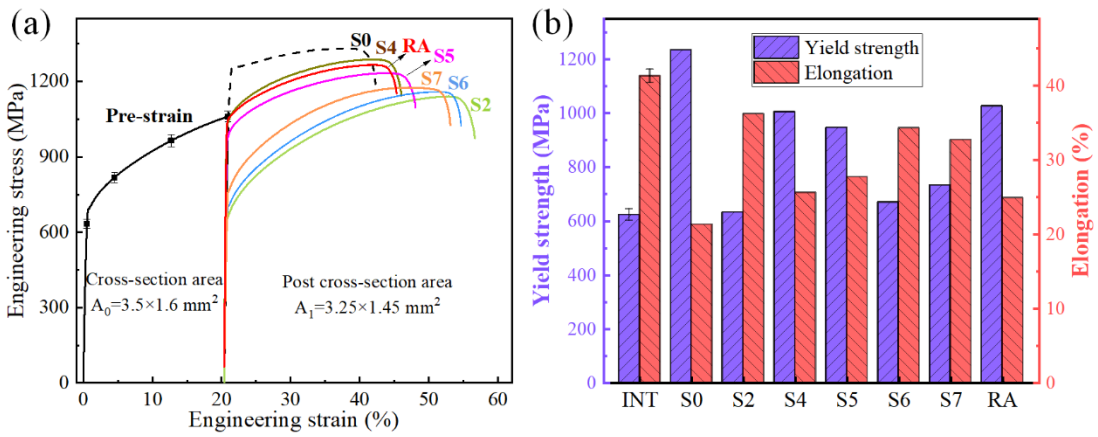

Fig. 4-5 Mechanical properties of each sample. (a) Engineering stress-strain curves and (b) plots of yield stress and elongation of each sample.

Moreover, the engineering stress-strain curves of the equivalent HDPEC-treated samples S6 and S7, and rapidly heated sample RA are also plotted in Fig. 4-5(a), and the mechanical properties of each sample are shown in Fig. 4-5(b). Compared with sample S2, the equivalent samples S6 and S7 also show the uncomplete strain-hardening relief. The yield strength of samples S6 and S7 are 669 MPa, 733 MPa, respectively, which are slightly high than the sample S2 and initial sample INT of 633 MPa and 623 MPa, indicating the strain hardening is not fully removed. Accordingly, the elongations of samples S6 and S7 are smaller than the samples S2 and INT, as

shown in Fig. 4-5(b). For the rapid annealing sample RA, only partial strain hardening was alleviated with a relatively high strength of 1026 MPa and a weak ductility of 24.9%, indicating the rapid annealing is inefficient in strain-hardening removing.

4.5 Microstructure evolution (in-situ observation) induced by HDPEC

4.5.1 Microstructure evolution of sample S4 (300 A/mm^2, 40 ms)

The EBSD observation before and after HDPEC treatment of sample S4 at the condition of 300 A/mm^2, 40 ms (13.33 ms × 3 pulses) are shown in Fig. 4-6. The EBSD maps covered a range of 80 × 60 μm^2 at the scanning step of 0.1 μm.

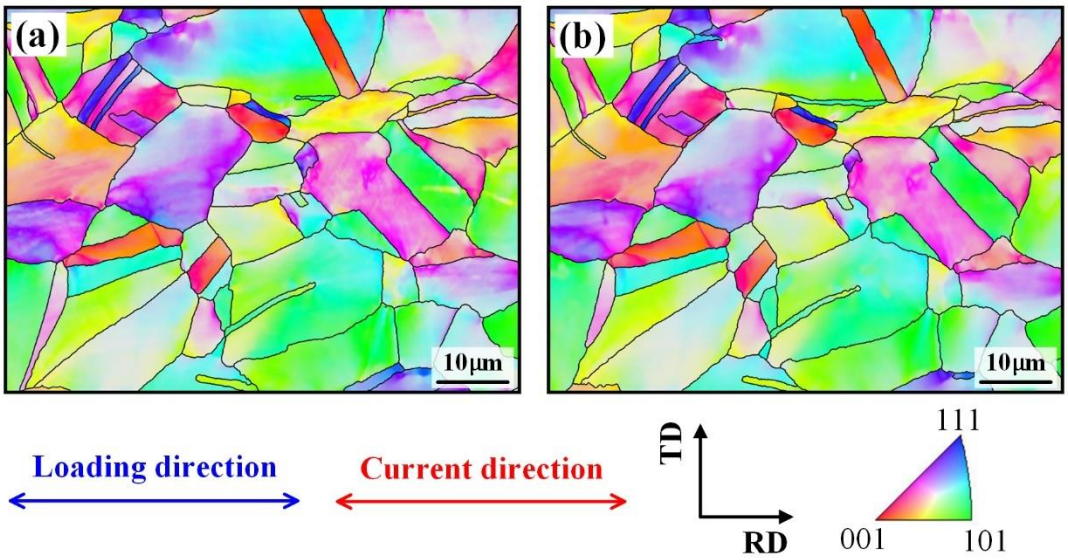

Fig. 4-6 EBSD orientation maps of sample S4 (a-b) before and after HDPEC treatment. The loading and current directions are towards the horizontal. RD and TD represent the rolling and transverse directions. The EBSD maps covered a range of 80×60 μm^2 with a scanning step size of 0.1 μm.

As illustrated in the figure, the microstructure is seldom changed with only several

grains evolution. To examine microstructure evolution in-depth, the GNDs and grain boundary characteristics maps were carried out to study the dislocation motion behavior and grain boundary evolution induced by HDPEC.

1. Dislocation motion behavior

Fig. 4-7 shows the GND maps before and after HDPEC treatment corresponding to the EBSD orientation maps, and the mean GND values are presented. In addition, the line distribution was also given to study the slip band evolution induced by HDPEC.

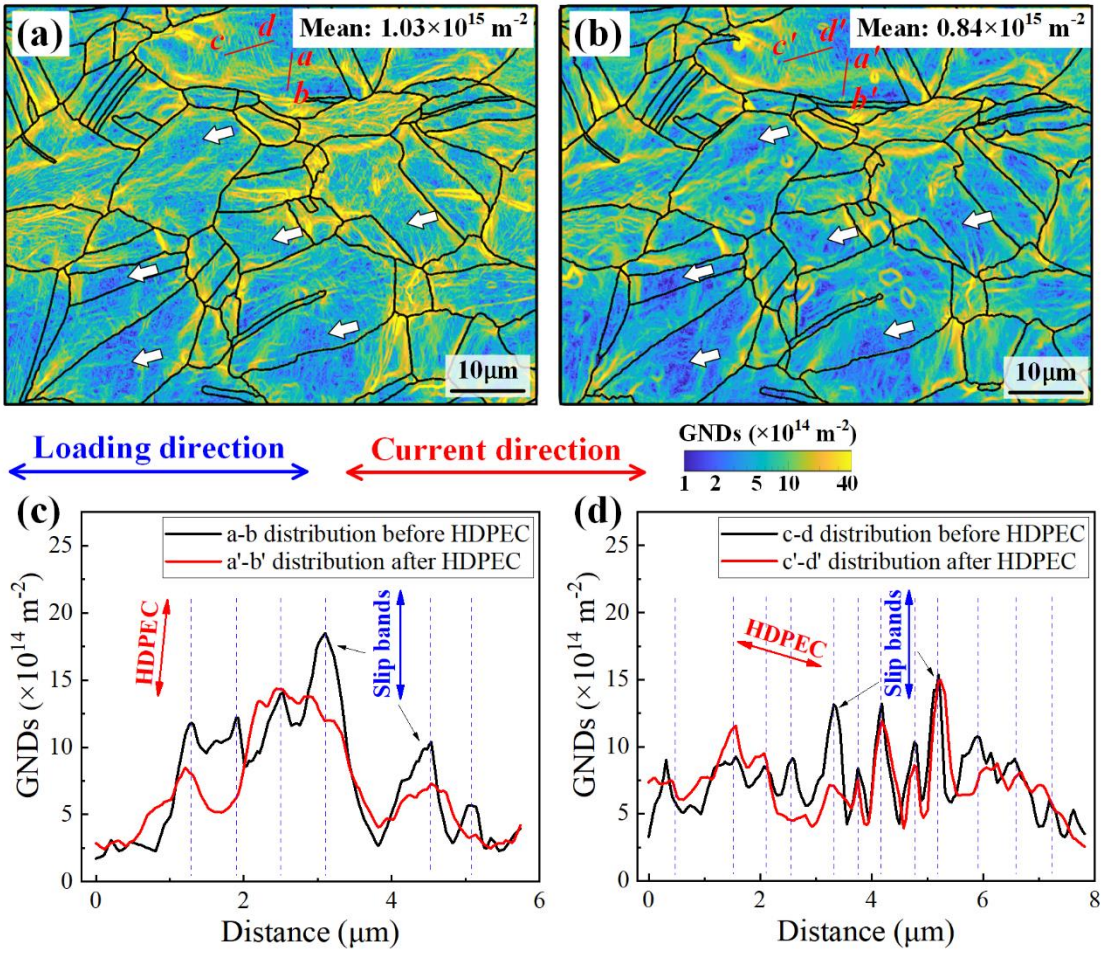

Fig. 4-7 GND maps of sample S4 (a-b) before and after HDPEC treatment at the condition of 300 A/mm^2 and 40 ms, where the loading and current directions are towards the horizontal. Line distributions of GNDs along Line (c) a-b and (d) c-d before and after HDPEC treatment.

As illustrated in the figure, sample S4 before HDPEC treatment shows a colored GND map with a high mean GND value of 1.03×10^{15} m^{-2} due to the pre-deformation, while the mean GNDs value was decreased to 0.84×10^{15} m^{-2} after HDPEC treatment at the condition of 300 A/mm^2, 40 ms. The GND maps before and after HDPEC treatment directly depict that the dislocation was driven and removed in some grains as marked in white arrows, where the color of the GND map changed from yellow to blue (high GND density to low GND density). Moreover, the line distributions of GND density along the Line a-b and c-d, as indicated in Fig. 4-7 (a-b) in red lines, are presented in Fig. 4-7(c-d) before and after HDPEC treatment. The results show that the dislocations on the slip bands along the direction of HDPEC (Fig. 4-7(c)) were partially removed (mean elimination rate reached 31% on some main slip bands), while that of other directions (Fig. 4-7(d)) almost remained (elimination rate approximately 6% on some main slip bands).

2. Grain boundary evolution

To examine the microstructure evolution, the grain boundary characteristics of the sample S4 before and after HDPEC treatment overlapped with band contrast (BC) maps are shown in Fig. 4-8, and the length of each boundary is also given. The sub-grain boundaries (SGBs, related to the dislocation entanglement) with a misorientation of less than 3° were drawn in blue lines with gradient transparency. The grain boundaries (GBs), such as the low angle grain boundaries (LAGBs, 3~15°), high angle grain boundaries (HAGBs, 15°~), and twin boundaries (TBs, 60±5°) were shown in red, black, and yellow lines, respectively.

As shown in Fig. 4-8, the SGBs, related to dislocation entanglement were reduced. Even in some local areas, the SGBs were almost removed, such as in the marked area 1-1', indicating the dislocation was driven and eliminated by HDPEC treatment. As shown in Fig. 4-8(e), the length of SGBs was reduced from 16688 μm to 12204 μm. The results of SGBs (i.e., dislocation entanglement) elimination plays a good

agreement with the dislocation density reduction after HDPEC treatment, as presented in the previous section.

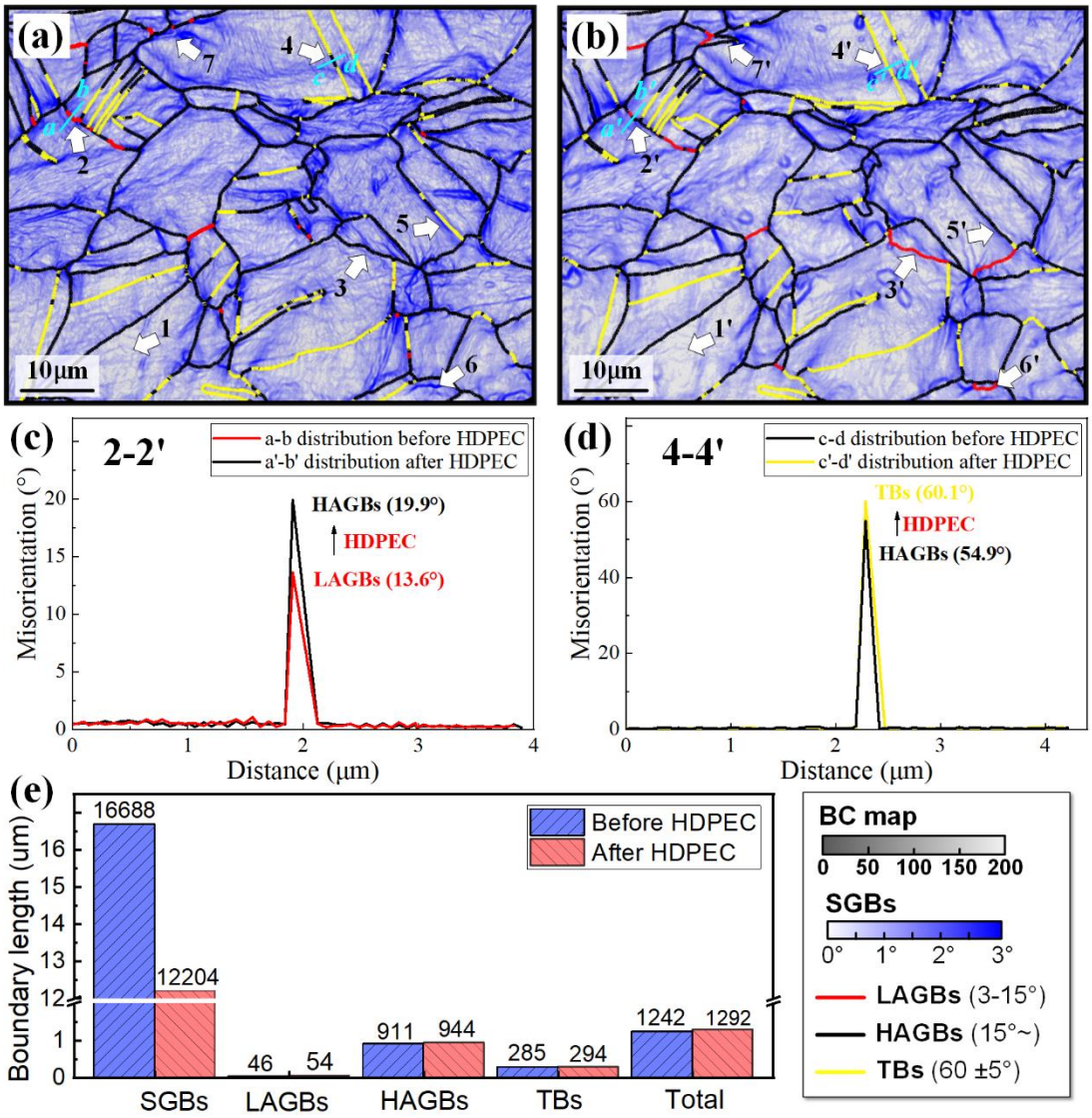

Fig. 4-8 Grain boundary characteristics of sample S4 (a-b) before and after HDPEC treatment with BC maps. Misorientation distributions on Line (c) a-b and (d) c-d before and after HDPEC treatment, and (e) grain boundary length of each sample. SGBs are shown in blue lines with gradient transparency, which means the misorientation range from 0~3°. LAGBs (3~15°) in red, HAGBs (15°~) black, and TBs (60±5°) yellow lines. The arrows marked areas indicate the grain boundary changes due to the HDPEC treatment.

Moreover, the mutual transformations between LAGBs and HAGBs were observed in the local areas of 2-2’ and 3-3’, respectively. The misorientation distribution along Line a-b at the local area of 2-2’ was shown in Fig. 4-8(c), and the grain boundary transformation from LAGBs (13.6°) to HAGBs (19.9°) happened after HDPEC treatment. In addition, the mutual transformations between HAGBs and TBs were also obtained in the local areas of 4-4’ and 5-5’. Also, the transformation from HAGBs (54.9°) to TBs (60.1°) after HDPEC treatment at the local areas of 4-4’ was shown in Fig. 4-8(d). Those mutual transformations may be related to the dislocation entanglement and disentanglement, which are promoted by the HDPEC. Furthermore, the new GBs of LAGBs and HAGBs at the local areas of 6-6’ and 7-7’ were also observed, which formed at the previous SGBs. The new GBs formation may be related to the dislocation entanglement and accumulation at the previous SGBs promoted by HDPEC. In conclusion, those transformations of GBs increase LAGBs, HAGBs, and TBs from 46, 911, 285 μm to 54, 944 and 294 μm, respectively, as shown in Fig. 4-8(e). Moreover, due to the newly formed GBs, the total length of GBs was increased from 1242 μm to 1292 μm, which causes grain refinement.

3. Grain evolution

The grain evolution before and after HDPEC treatment was shown in Fig. 4-9, where the changed areas were marked in white arrows in the EBSD maps. The grain evolution was related to the formation of new GBs, which divided the grains and caused grain refinement. Moreover, grain refinement was achieved due to the new LAGBs and HAGBs from the previous SGBs. The grain divisions (i.e., grain refinement) were marked at the local areas of 1-1’, 2-2’, 3-3’, 4-4’, and 5-5’ using the solid arrows in the EBSD maps, as shown in Fig. 4-9(a,b).

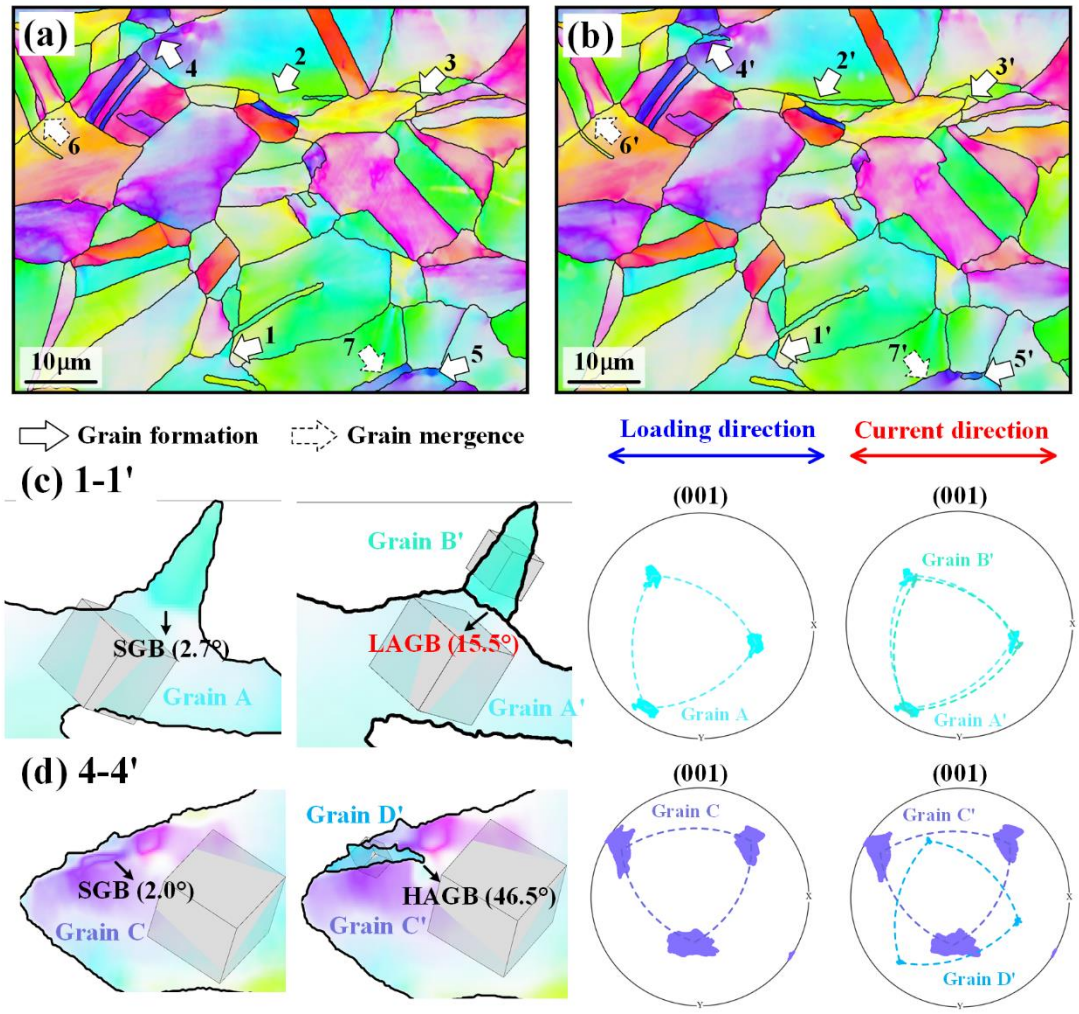

Fig. 4-9 EBSD maps of sample S4 (a-b) before and after HDPEC treatment with arrows representing the grain evolution, where solid arrows represented the grain formation after HDPEC treatment and dashed arrows denote the grain mergence. The loading and current directions are towards the horizontal. (c) Local EBSD maps and pole figures of the new grain formation at the local area 1-1' due to the formation of LAGB. (d) Local EBSD maps and pole figures of the new grain formation at the local area 4-4' due to the formation of HAGB.

Moreover, as presented in Fig. 4-9(c), the formation of Grain B' divided from the previous Grain A was related to the newly formed grain boundary. The pole figure shows that Grain A' and Grain B' have similar orientations, implying the boundary is LAGB with a misorientation of 15.5°. In addition, the formation of Grain D' was due

to the newly formed HAGBs (46.5°), where the orientation of Grain D' is much different with that of Grain C', as shown in the pole figures of Fig. 4-9(d). Furthermore, the newly formed grains contributed to the orientation change or texture evolution induced by HDPEC. Furthermore, the grain emergences were also observed, which were marked using dashed arrows at the local areas of 6-6' and 7-7'. The grain emergences were related to the elimination of grain boundary by HDPEC treatment. To sum up, the total grain number was increased from 77 to 80 grains in this local area, which causes the grain refinement.

4.5.2 Microstructure evolution of sample S5 (300 A/mm^2, 45 ms)

The EBSD observation before and after HDPEC treatment of sample S5 at the condition of 300 A/mm^2, 45 ms (15 ms × 3 pulses) are shown in Fig. 4-10. The EBSD maps covered a range of 80 × 60 μm^2 with a scanning step size of 0.1 μm.

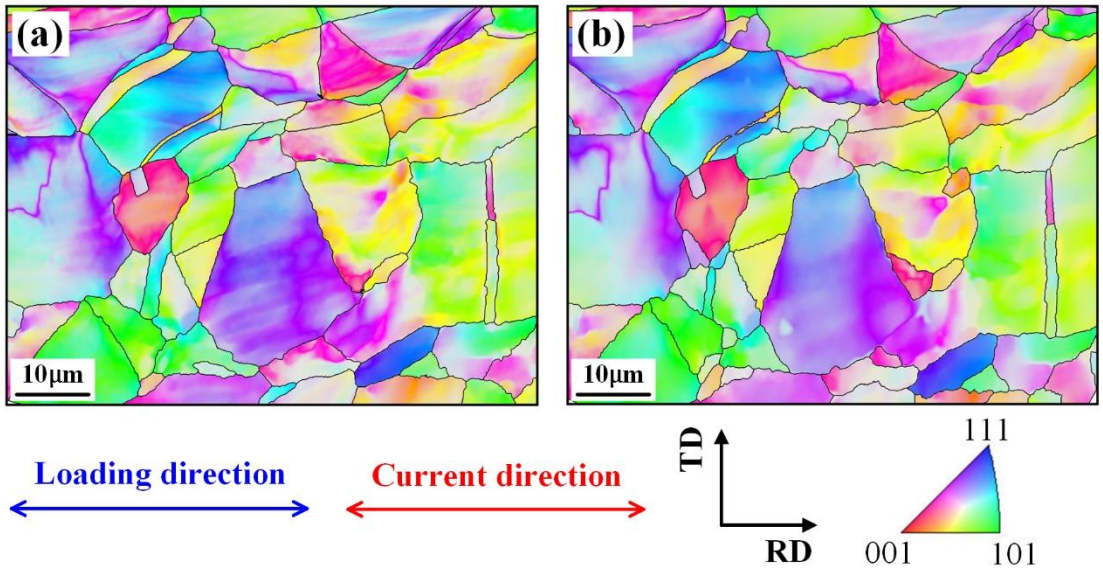

Fig. 4-10 EBSD orientation maps of sample S5 (a-b) before and after HDPEC treatment. The loading and current directions are towards the horizontal. RD and TD represent the rolling and transverse directions. The EBSD maps covered a range of 80×60 μm^2 with a scanning step size of 0.1 μm.

As shown in this figure, some grain evolution was observed. To profoundly investigate microstructure evolution, such as the dislocation and grain boundary evolutions, the GNDs and grain boundary characteristics maps were carried out.

1. Dislocation motion behavior

Fig. 4-11 shows the GND maps before and after HDPEC treatment of sample S5, and their mean GNDs density are also presented. In addition, the line distribution was given to study the slip band evolution induced by HDPEC.

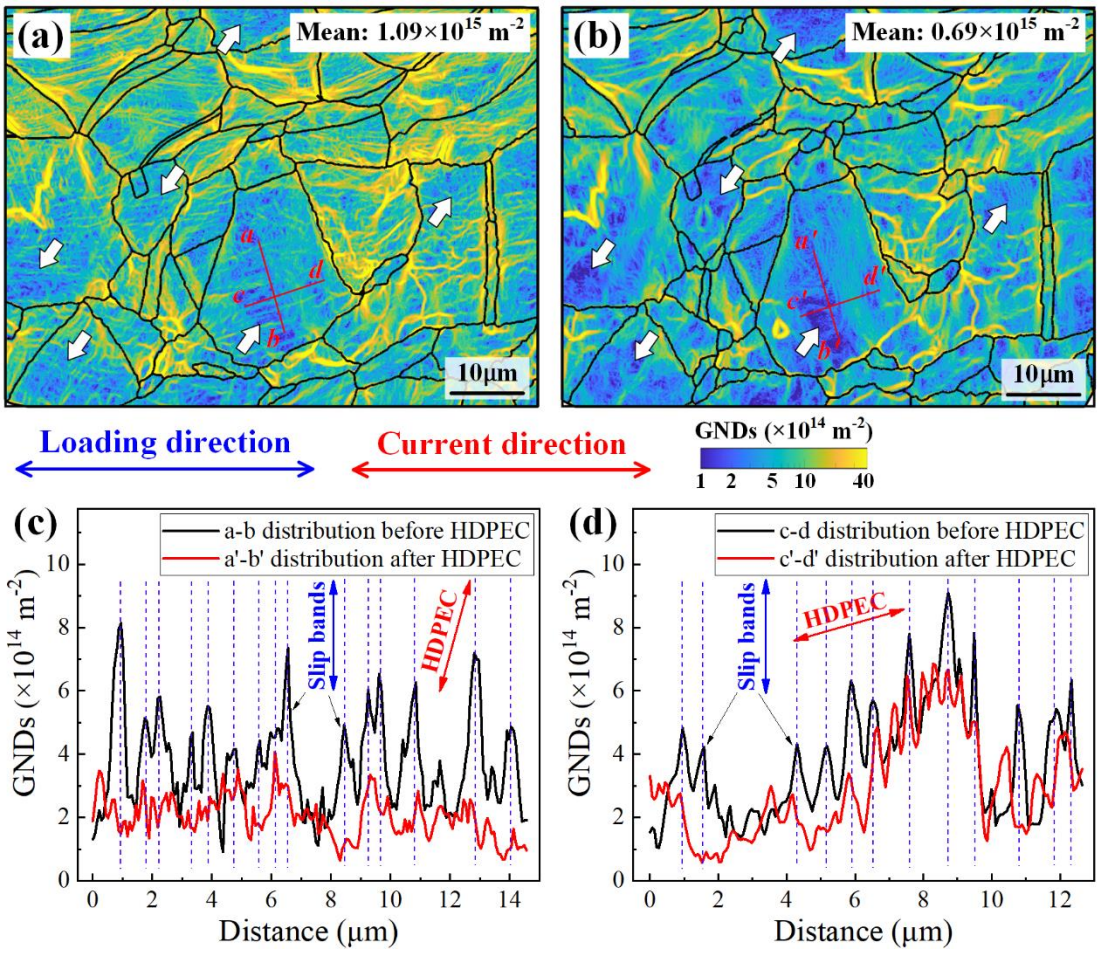

Fig. 4-11 GND maps of sample S5 (a-b) before and after HDPEC treatment at the condition of 300 A/mm^2 and 45 ms, where the loading and current directions are towards the horizontal. Line distributions of GNDs along Line (c) a-b and (d) c-d before and after HDPEC treatment.

As shown in the figure, sample S5 shows a colored GND map with a high value of 1.09×10^{15} m^{-2} before HDPEC treatment due to the pre-deformation, while the mean GNDs value was decreased to 0.69×10^{15} m^{-2} after HDPEC treatment at the condition of 300 A/mm^2, 45 ms, indicating the dislocations were driven and eliminated by HDPEC treatment. The GND maps directly show that the dislocation was driven and removed in some grains as marked in the white arrows, where the color of the GND map changed from yellow to blue (high GND density to low GND density). Moreover, the line distributions of GND density along the Line a-b and c-d, as marked in Fig. 4-11(a-b) in red lines, are presented in Fig. 4-11(c-d) before and after HDPEC treatment. The results illustrated that the dislocations on the slip bands along the direction of HDPEC (Fig. 4-11(c)) were highly removed (mean elimination rate reached approximately 68% on some main slip bands), while that of other directions (Fig. 4-11(d)) was slightly eliminated (elimination rate approximately 29% on some main slip bands). The elimination of dislocations on the slip bands may be attributed to the combination of dipole dislocations promoted by HDPEC. Hence, this observation can be used to explain the slip band healing induced by HDPEC, as presented in Fig. 3-14.

2. Grain boundary evolution

The grain boundary characteristics of the sample S5 before and after HDPEC treatment overlapped with band contrast (BC) maps were shown in Fig. 4-12, and the length of each boundary was also given. The SGBs were evidently reduced, as shown in Fig. 4-12(e), and the length of SGBs was reduced from 18528 μm to 10263 μm. In many local areas, the dislocation entanglement was almost removed by HDPEC treatment, such as in local area 1-1'. The elimination of SGBs (i.e., dislocation entanglement) plays a good agreement with the dislocation density reduction after HDPEC treatment, as presented in the previous section.

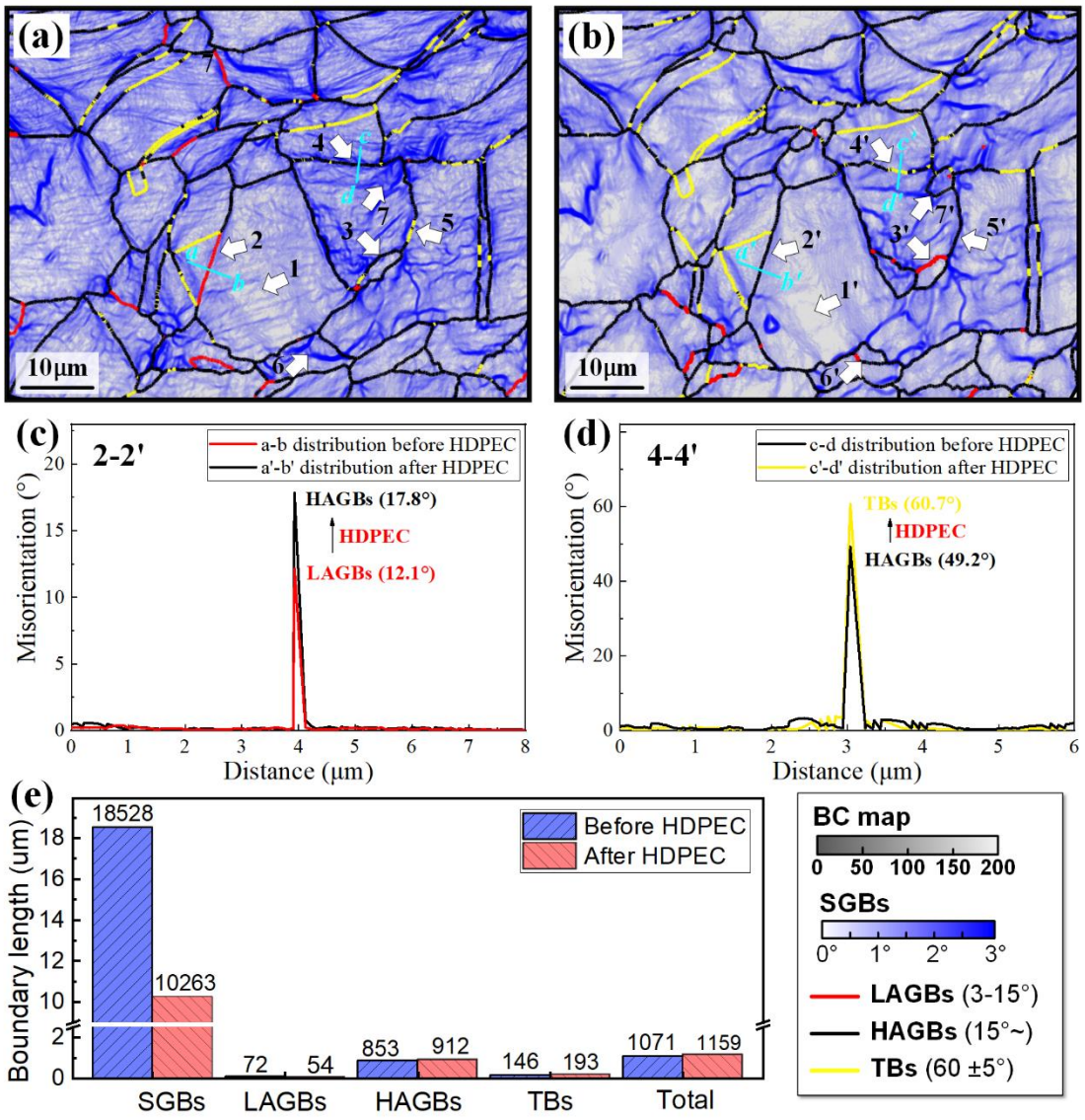

Fig. 4-12 Grain boundary characteristics of sample S5 (a-b) before and after applying HDPEC with BC maps. Misorientation distributions along Line (c) a-b and (d) c-d before and after HDPEC treatment, and (e) grain boundary length of each sample. SGBs are shown in blue lines with gradient transparency, which means the misorientation range from 0~3°. LAGBs (3~15°) in red, HAGBs (15°~) black, and TBs (60±5°) yellow lines. The arrows marked areas indicate the grain boundary changes due to the HDPEC treatment.

Moreover, the mutual transformations between LAGBs and HAGBs, and HAGBs and TBs were also observed in the local areas of 2-2' and 3-3', and 4-4' and 5-5',

respectively. Fig. 4-12 (c-d) illustrated the misorientation distributions along Line a-b and c-d at the local areas of 2-2’ and 4-4’. The misorientation distribution along Line a-b, as shown in Fig. 4-12(c), presented the grain boundary transformation from LAGBs (12.1°) to HAGBs (17.8°) after HDPEC treatment. Also, the transformation from HAGBs (49.2°) to TBs (60.7°) after HDPEC treatment at the local areas of 4-4’was shown in Fig. 4-12(d). Those transformations may be associated with the dislocation entanglement and disentanglement driven by the HDPEC. Furthermore, the new GBs of LAGBs and HAGBs at the local areas of 6-6’ and 7-7’ were also observed, which formed from the previous SGBs. The new GBs were created after the dislocation entanglement and accumulation at the previous SGBs. To sum up, those transformations of GBs result in the decrease of LAGBs from 72 μm to 54 μm, and the increase of HAGBs and TBs from 853, 146 μm to 912 and 193 μm, respectively, as shown in Fig. 4-12(e). Moreover, due to the newly formed GBs, the total length of GBs was increased from 1071 μm to 1159 μm, which causes grain refinement.

3. Grain evolution

The grain evolution before and after HDPEC treatment was shown in Fig. 4-13, where the changed areas were marked in white arrows in the EBSD maps. The grain evolution was related to the formation of new GBs, which divided the grains and caused grain refinement. The representative grain divisions (i.e., grain refinement) were marked at the local areas of 1-1’, 2-2’, 3-3’, 4-4’, 5-5’, 6-6’, 7-7’, and 8-8’ using the solid arrows, as shown in Fig. 4-13(a,b). The grain divisions were achieved and then induced the grain refinement due to the new formation of LAGBs and HAGBs from the previous SGBs, as shown in Fig. 4-9(c,d), the formation of Grain B’ and Grain D’ was due to the newly formed LAGBs (16.3°) and HAGBs (48.1°) from the previous SGBs with a misorientation of 2.1° and 2.3°, respectively. The pole figures were also present at the right side, indicating the orientation change of the newly formed grains with the mother grain. Hence, the newly formed grains contributed to

the orientation change or texture evolution induced by HDPEC. Furthermore, the grain emergences were also observed, which were marked using dashed arrows at the local areas of 9-9' and 10-10'. In conclusion, the total grain number was increased from 69 to 75 grains in this local area, which caused the grain refinement.

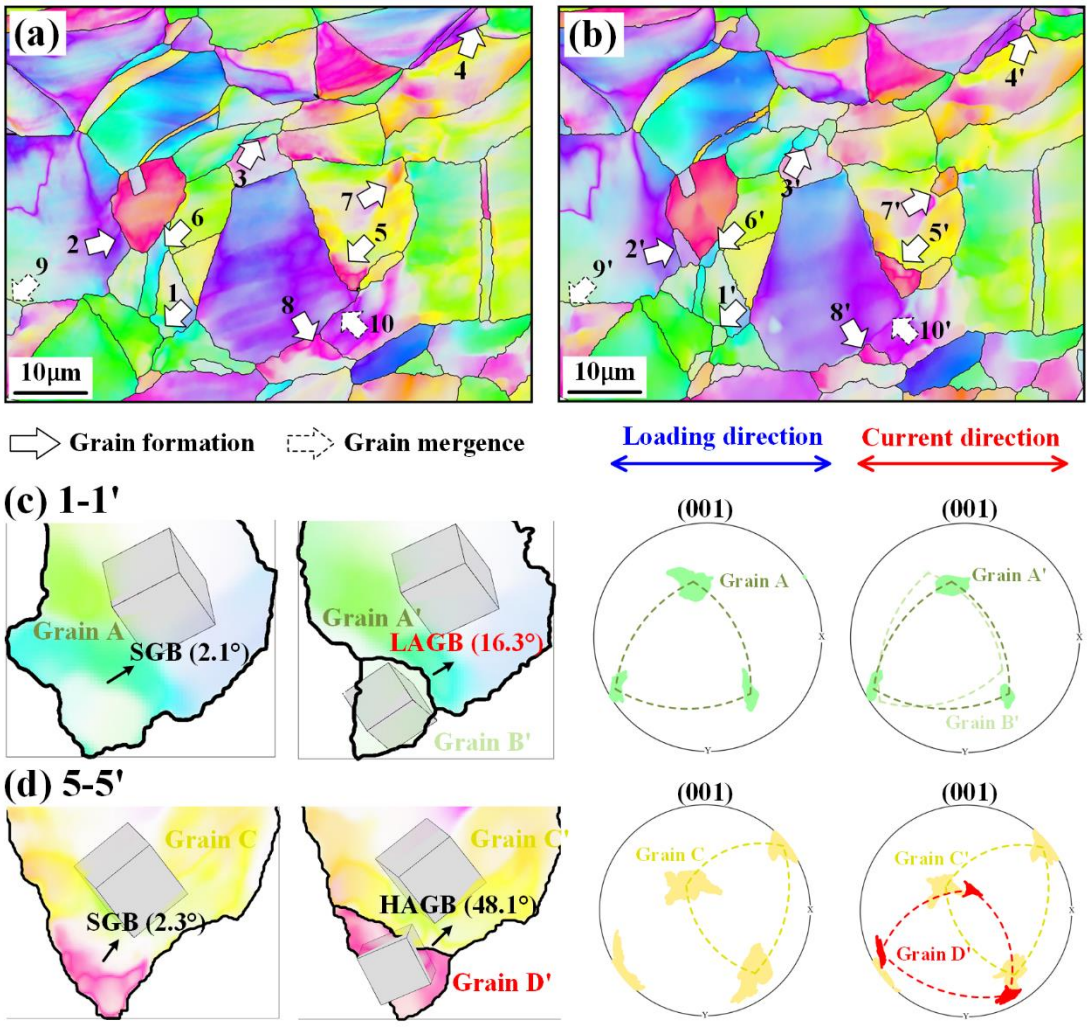

Fig. 4-13 EBSD orientation maps of sample S5 (a-b) before and after HDPEC treatment with arrows representing the grain evolution, where solid arrows represented the grain formation after HDPEC treatment and dashed arrows denote the grain mergence. The loading and current directions are towards the horizontal. (c) Local EBSD maps and pole figures of the new grain formation at the local area 1-1' due to the formation of LAGB. (d) Local EBSD maps and pole figures of the new grain formation at the local area 5-5' due to the formation of HAGB.

4.5.3 The effect of HDPEC on microstructure evolution

As mentioned in Chapter 3, the initial (as-annealed) sample shows low LAGBs and high HAGBs and TBs, which obeying to the natural distributions of GBs in defect-free materials. The fractions of LAGBs, HAGBs, and TBs of the as-annealed sample are 4.4%, 57.9%, and 37.7%, respectively, as shown in Fig. 4-14. After deformation, plenty of SGBs formed due to the dislocation multiplication and entanglement, as shown in Fig. 3-6. And also, the LAGBs tremendously increased due to dislocation entanglement, and it occupied approximately 28.3%. Furthermore, owing to dislocations slip on TBs and entangled at TBs, resulting in the TBs transformed to HAGBs, which caused the fraction of TBs decreased to 15.9%. Hence, due to the increase in LAGBs and decrease in TBs after deformation, the fraction of HAGBs remains almost unchanged, which occupied around 55.8%. After HDPEC treatment at the condition of 300 A/mm^2 and 50 ms, the SGBs were entirely removed, and LAGBs were reduced evidently, indicating the dislocations were eliminated by HDPEC. Moreover, the TBs were recovered due to the entangled dislocations were removed by HDPEC. The fractions of each boundary that were recovered to the initial levels after HDPEC treatment, which are occupied approximately 1.9%, 62.4%, and 35.7%, respectively, as shown in Fig. 4-14.

The microstructure evolution induced by HDPEC was studied in this chapter using the quasi-in-situ EBSD observation. The results show that the dislocation motion can be improved by HDPEC treatment, and the dislocation annihilation was achieved. The elimination of dislocations induced by HDPEC via the combination of dipole dislocations on the slip bands, entanglement at GBs, and entangled at SGBs and then form new GBs of LAGBs and HAGBs, was observed. Moreover, the mutual transformations between LAGBs and HAGBs, and HAGBs and TBs were also observed after HDPEC treatment, as shown in Fig. 4-8 and Fig. 4-12. Those transformations were related to the dislocation entanglement and disentanglement driven by HDPEC. However, the main transformation was towards the right, from

LAGBs→HAGBs→TBs, which causes the decrease in LAGBs and increase of TBs. Finally, a significant reduction in LAGBs and an increase in TBs were achieved, and the natural distribution of GBs was obtained after HDPEC treatment, as shown in Fig. 4-14. Furthermore, the newly formed GBs of LAGBs and HAGBs from the previous SGBs after HDPEC treatment contributed to the increase in GBs and then caused the grain refinement. Meanwhile, the newly formed GBs, especially for the HAGBs, which means significant rotation occurred in crystals and thereby resulting in the orientation changes in materials, namely the changes in texture, as shown in Section 3.5.3. Hence, almost all the microstructure evolution, such as GBs evolution, slip bands healing, grain refinement, and texture evolution, were related to dislocation motion and elimination promoted by HDPEC. The discussion on the driving force for dislocation motion induced by HDPEC was carried out in detail in Section 4.7.

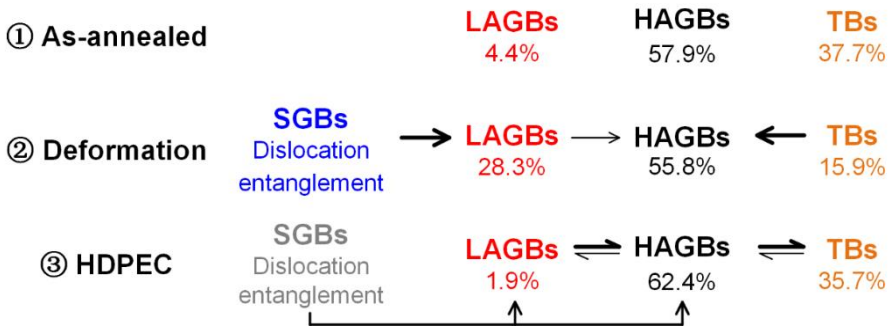

Fig. 4-14 Grain boundary evolution due to the deformation and HDPEC treatment, where the dark and light arrows represent a large or small number of boundary conversions.

4.6 The contributions of thermal and athermal effects on strain-hardening relief

4.6.1 Microstructure evolution of the equivalent samples

The EBSD orientation maps of the equivalent samples S6 and S7 and the rapid

annealing sample RA are shown in Fig. 4-15. T the bar diagram of the mean grain size of each sample is shown in Fig. 4-15(d). Compared with the sample S2, as shown in Fig. 3-5(d) in Chapter 3, the equivalent samples S6 and S7 show more refined grains with a mean grain size of 11.3 and 11.0 μm, respectively, after HDPEC treatment, as shown in Fig. 4-15(a, b). For the rapid annealing sample RA, many small grains formed compared with the sample S0 shown in Fig. 3-5(b), resulting in the grain size decreased to 13.1 μm.

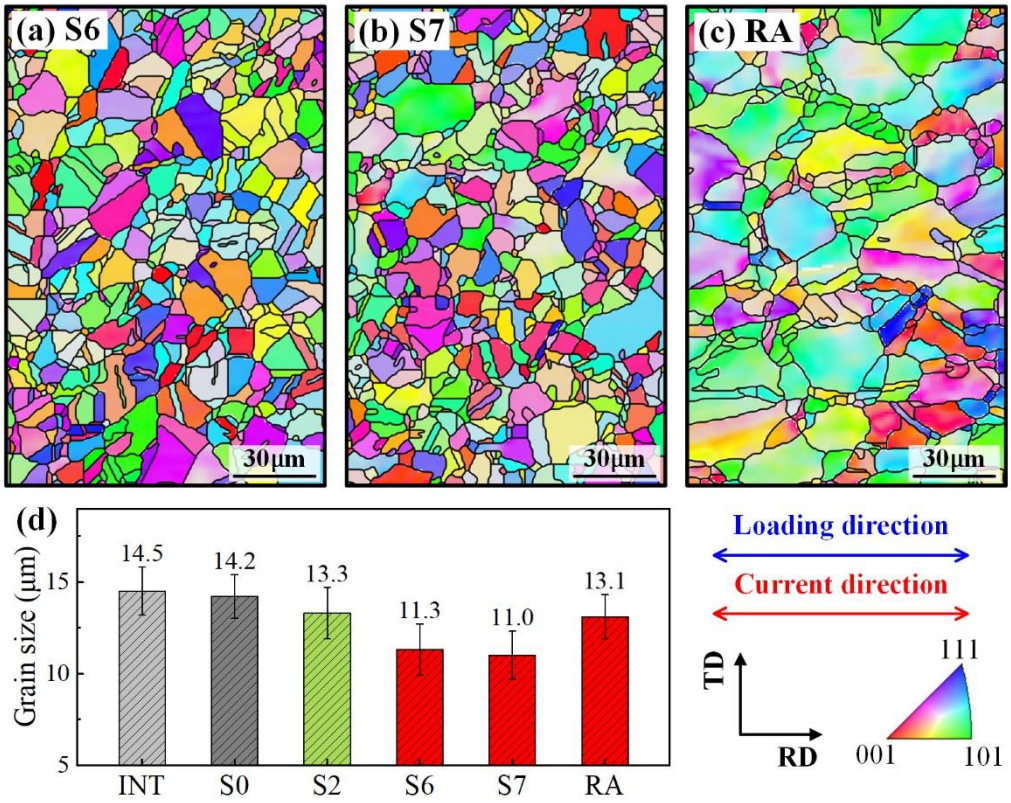

Fig. 4-15 EBSD orientation maps and grain size distributions of (a) S6, (b) S7, (c) RA. (d) Mean grain size of each sample. The loading and current directions are towards the horizontal. RD and TD represent the rolling and transverse directions. The EBSD maps covered a range of 120×180 μm^2 with a scanning step size of 1 μm.

To investigate the local deformation evolution induced by HDPEC treatment, the GND maps corresponding to EBSD orientation maps were presented in Fig. 4-16. As

obtained in Chapter 3, the complete recovery (low GNDs density, 0.24×10^{14} m^{-2}) in sample S2 was obtained, as shown in Fig. 3-10(d). However, samples S6 and S7, as the equivalent samples with sample S2, showed the uncomplete recovery in their microstructure. Some unrecovered areas were observed in S6 and S7, as shown in Fig. 4-16(a, b), and the mean GNDs density is 0.32×10^{14} and 0.47×10^{14} m^{-2}, respectively. For the rapid annealing sample RA, the colored map remained with a relatively high GNDs density of 1.06×10^{14} m^{-2}, indicating the strain hardening was seldom removed by rapid heating.

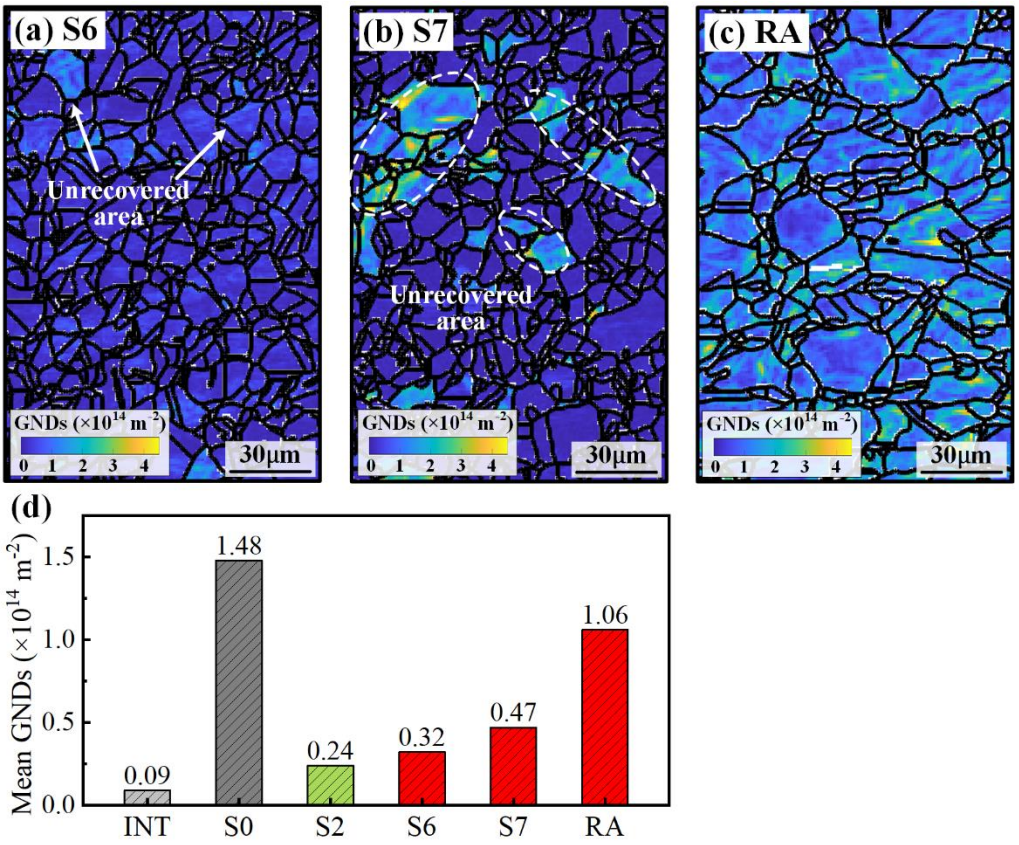

Fig. 4-16 GND maps corresponding to the EBSD orientation maps of (a) S6, (b) S7, (c) RA, and (d) mean GNDs density of each sample.

4.6.2 The effects of thermal and athermal on strain-hardening relief

As presented in Section 4.3, the temperature-time curves of the equivalent HDPEC-treated samples S2, S6, and S7 are similar, as shown in Fig. 4-3(b), indicating that the thermal effect of them during HDPEC treatment is almost the same. Furthermore, the rapid annealing sample RA shows a broader temperature-time curve than that of samples S2, S6, and S7, implying the thermal effect of sample RA is more significant than that of samples S2, S6, and S7. In this chapter, the thermal effect in the HDPEC-treated samples and rapidly heated sample are considered the same. As shown in Fig. 4-17, the schematic diagrams of each sample are presented. The symbol of T with yellow background denotes the thermal effect. The same yellow background in samples S2, S6, S7, and RA indicates the same thermal effect.

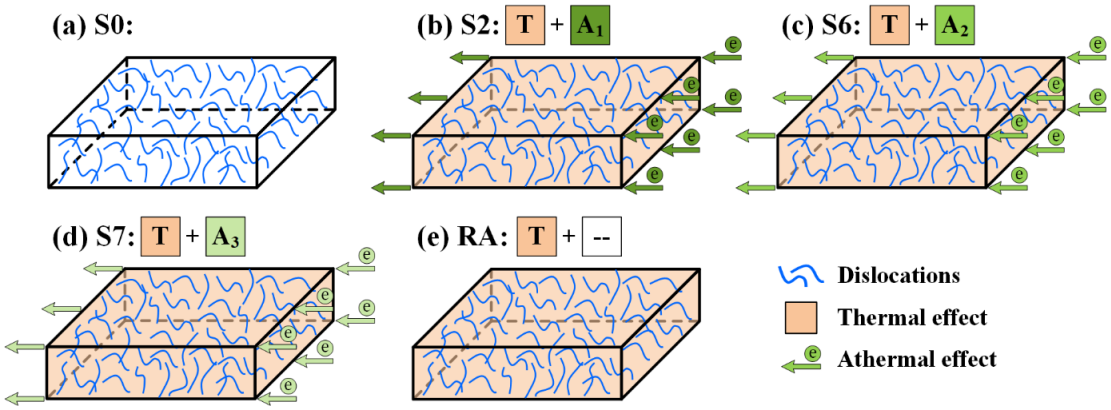

Fig. 4-17 The effect of thermal and athermal on strain-hardening relief. Schematic diagrams of sample (a) S0, (b) S2, (c) S6, (d) S7, and (e) RA, where the curved blue lines represent the dislocations, the symbols of T and A with yellow and green backgrounds represent the thermal and athermal effects, and green arrows represent the electric current flow.

Moreover, the HDPEC-treated samples S2, S6, and S7 possess not only the thermal effect but also the athermal effect, while the rapid annealing sample RA is only subjected to the thermal effect. The athermal effect regarding the electron wind force,

as presented in Section 1.3 and Appendix 1, is proportional to the electric current density. Hence, according to the current density applied on samples S2, S6, and S7 of 300, 100, and 50 A/mm^2, the athermal effects are, in descending order, S2, S6, and S7. Fig. 4-17 shows that the athermal effect is presented using a green background. The intensity of which uses the shades of color, where the dark green represents the high athermal effect, and light green denotes the low athermal effect. Hence, the athermal effects in samples S2, S6, and S7 are A_1, A_2, A_3, and the relationship of which is $A_1>A_2>A_3$. The rapid annealing sample RA does not have the athermal effect. The details are listed in Table 4-2.

Table 4-2 Thermal and athermal effects in each sample.

Samples	Treatments	Effects	
		Thermal	Athermal
S0	--	--	--
S2	300 A/mm^2, 50 ms	T	A_1
S6	100 A/mm^2, 450 ms	T	A_2
S7	50 A/mm^2, 1800 ms	T	A_3
RA	1200 °C, 20 s	T	--

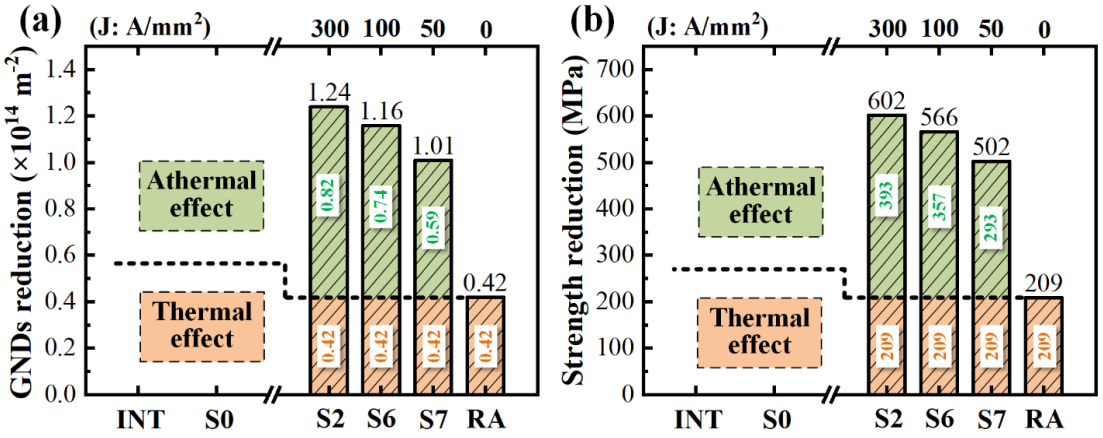

Fig. 4-18 The effects of thermal and athermal on the reduction of (a) GNDs density and (b) yield strength.

Since the dislocation is the main reason that causes the strain hardening, the dislocation density was used as an evaluation indicator for estimating the effects of thermal and athermal on the strain-hardening relief. Furthermore, the strength is also associated with the dislocation density according to Taylor's hardening law, as shown in Eq. (3-1). Hence, the changes in strength after HDPEC treatment can also be treated as an evaluation indicator. The HDPEC and rapid heating that caused the dislocation density and strength reduction is plotted in Fig. 4-18.

For the rapid annealing sample RA, the GNDs density reduced from sample S0 of 1.48×10^{14} m^{-2} to sample RA of 1.06×10^{14} m^{-2}, and the reduction is approximately 0.42×10^{14} m^{-2}. The reduction in yield strength is around 209 MPa from 1235 MPa to 1026 MPa. Since sample RA is only subjected to the thermal effect, the reduction in GNDs density of 0.42×10^{14} m^{-2} and yield strength of 209 MPa is related to the athermal effect. Moreover, as mentioned before, the thermal effect in samples S2, S6, and S7 is less than that in sample RA, which possesses a broader temperature-time curve. Hence, the thermal effect in samples S2, S6, and S7 that caused the reduction in GNDs density and yield strength is less than 0.42×10^{14} m^{-2} and 209 MPa, respectively. For ease of analysis, the thermal effect of the equivalent HDPEC-treated samples is considered the same as sample RA. Hence, the reduction in GNDs density of samples S2, S6, and S7 are 1.24, 1.16, and 1.01×10^{14} m^{-2}, respectively, and among them, the density of 0.42×10^{14} m^{-2} is due to the thermal effect and the other part of 0.82, 0.74, and 0.59×10^{14} m^{-2} are related to the athermal effect. Similarly, the reduction in yield stress of 209 MPa is related to the thermal effect, while the decreases of 393, 357, and 293 MPa are associated with the athermal effect in samples S2, S6, and S7. Therefore, the athermal effect caused the GNDs density reduction of 1.24, 1.16, and 1.01×10^{14} m^{-2} is higher than the thermal effect of 0.42×10^{14} m^{-2}, and the strength reduction of 393, 357, and 293 MPa than that of 209 MPa, implying that the athermal effect is more significant than thermal effect in strain-hardening relief. Moreover, among the HDPEC-treated samples, the higher the electric current density,

the more the GNDs density and strength reduction.

4.7 Discussion

All the microstructure evolution, as mentioned in the above sections, such as grain boundary evolution and grain refinement, was related to the dislocation motion induced by HDPEC. Hence, in this section, the effect of HDPEC (e.g., thermal and athermal effects) on the dislocation motion was analyzed.

First of all, the condition that causes the dislocation motion is that the driving force exerted on dislocations should be larger than the resistance force, as shown in the equation (4-1):

$$f_d > f_r \qquad (4-1)$$

where f_d and f_r represent the driving and resistance force exerted on dislocations. Hence, all the discussions are regarding how the HDPEC affects these two forces: driving and resistance force. The HDPEC effect contains two aspects: thermal and athermal effects, where the thermal effect is related to temperature rising caused by HDPEC treatment, and the athermal effect is mainly associated with electron wind force. The thermal effect may provide the driving force for dislocation climb and help in reducing the resistance force. The athermal effect of EWF mainly provides the driving force for dislocation glide. A detailed discussion was carried out.

4.7.1 Driving force of dislocation motion during HDPEC treatment

1. Thermal effect

As mentioned in Section 1.3 and Appendix 1, the thermal effect not only contributed to softening the materials (reducing the dislocation motion resistance) but also provides the driving force for dislocation climb. The dislocation climb was promoted

by atomic (vacancy) diffusion and finally disappeared at the grain boundary, which is the so-called traditional heat treatment. The driving force for dislocation climb as shown in Eq. (A1-2): $f_{d\_T} = \frac{kT}{b^2}\ln\left(\frac{c}{c_0}\right)$, which is proportional to the temperature.

2. Electron wind force

The estimation of EWF was carried out based on the specific dislocation resistivity in the form of Eq. (A1-3): $F_{EW} = \left(\frac{\rho_d}{N_d}\right) en_e J$. Parameter ρ_d is the electrical resistivity caused by dislocations, as reported in Ref. [1], the electrical resistivity of IN718 was increased from 1.063×10^{-6} Ω•m to 1.092×10^{-6} Ω•m (at the plastic strain of 20%, near the value used in this study, 20.5%). Hence, the electrical resistivity caused by dislocations is approximately $(1.092\text{-}1.063)\times10^{-6} = 0.029\times10^{-6}$ Ω•m. The dislocation density at the plastic strain of 20.5% was 11.4×10^{14} m^{-2}, as shown in Fig. 3-4. Therefore, the specific dislocation resistivity $\frac{\rho_d}{N_d}$ is 2.54×10^{-23} Ω•m^3. Parameter e the electron charge as 1.6×10^{-19} A•s, n_e the electron density 1.8×10^{29} m^{-3}, and J current density 300 A/mm^2. Thus, the EWF estimated using the method of specific dislocation resistivity is approximately $F_{EW} = 2.2 \times 10^{-4}$ N/m. For driving the dislocation moved a unit Burgers length b, it exerted approximately $f_{d\_EWF} = F_{EW}/b = (2.2 \times 10^{-4})/(0.255 \times 10^{-9})$ Pa = 0.86 MPa on dislocation.

In contrast, the evaluation based on Eq. (A1-4), $F_{EW} = \alpha b p_F n_e (v_e - v_d)$, was also presented. Parameter $\alpha \approx 0.25\sim1.0$, b the magnitude of Burgers vector 0.255×10^{-9} m, p_F the Fermi momentum took as 6.33×10^{-6} ev•s/m, $v_e = J/(en_e)$ the velocity of electron and v_d the velocity of dislocation taken as 0 m/s. Hence, the EWF based on the equation of quantum mechanics was around ~4.87×10^{-7} N/m. Based on the $F_{EW} = f_{d\_EWF} b$, the stress exerted on the dislocation was approximately f_{d_EWF} = ~0.002 MPa, which is two orders of magnitude less than the value calculated by the method of specific dislocation resistivity.

The lattice distortions caused by the second phase in IN718 are not taken into account to calculate the Fermi momentum in the quantum mechanical model, which may cause the result of electron wind force is too small. Moreover, for the method regarding the specific dislocation resistivity, the calculation is reasonable due to the realistic dislocation density and its caused increase in resistance was used in this model. Hence, in the following analysis, the result of EWF calculated by the method of specific dislocation resistivity was used.

4.7.2 Effect of HDPEC on resistance force of dislocation motion

As mentioned in Section 1.3 and Appendix 1, thermal has a significant impact on the resistance of dislocation moving. The critical resolved shear stress (CRSS) is generally used to estimate the necessary stress that causes the slip in grains, which means the dislocations are highly activated. The CRSS is associated with the yield of materials, can be obtained using the maximum value of the Schmid factor m, as:

$$f_{r\_CRSS} = m_{max} \cdot \sigma_y(T) \qquad (4-2)$$

The yield stress of IN718 regarding the temperature [2], $\sigma_y(T)$, was shown in Fig. 4-19, and the CRSS, $f_{CRSS} = m \cdot \sigma_y$, depends on the temperature was also presented, where the Schmid factor *m* is roughly chosen as 0.327 [3]. As shown in Fig. 4-19, the activated stress, CRSS, for slip (i.e., dislocation motion) was about 200 MPa within the range of 0 to 500°C, after increasing the temperature, CRSS was rapidly decreased and reached another stable zone of approximately ~ 30 MPa when the temperature over 1000°C. This means that the dislocation can be moved as long as the driving force exceeds 30 MPa when heated the sample above 1000°C.

Here, one thing should be mentioned that the CRSS denotes the observed yield phenomenon, which means that it already has plenty of dislocations being activated. Hence, CRSS has overestimated the true resistance of dislocation motion. The activation stress of the dislocation should be less than the CRSS.

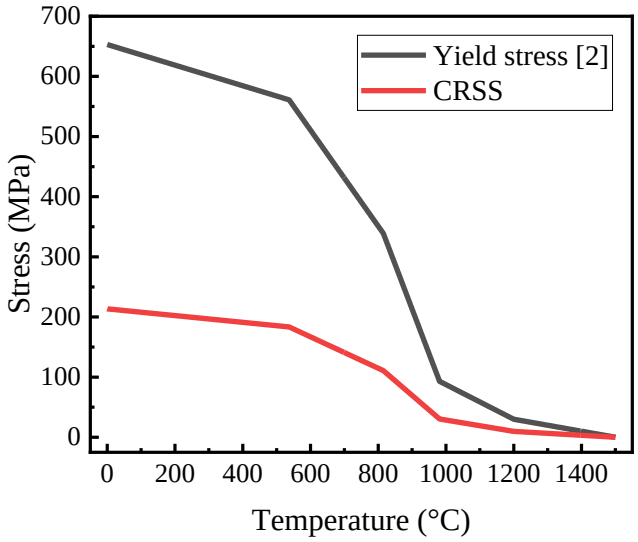

Fig. 4-19 Yield stress and CRSS of solution-treated IN718 depends on the temperature.

Moreover, the Peierls-Nabarro (PN) stress [4,5] depicts that the stress is required to move the individual dislocation. Peierls and Nabarro estimated the energy of the dislocation per length regarding the dislocation position and proposed the shear stress required to move a dislocation as:

$$f_{r\_PN} \approx \frac{2G(T)}{(1-v)} \exp\left(\frac{-2\pi d}{(1-v)b}\right) \qquad (4-3)$$

where $G(T)$ is shear modulus regarding the temperature, v Poisson's ratio can be chosen as 0.3, d interplanar spacing taken as $\sqrt{3}/2b$, and b Burgers vector. Hence, $f_{r\_PN} \approx 1.2 \times 10^{-3} G(T)$ was obtained. This is a theoretical result, which is much larger than the experimental value. Based on many experimental observations, the PN stress should be in the range of 10^{-6} ~ $10^{-5} G(T)$ for FCC metals [6,7]. The shear modulus of IN718 regarding the temperature [2] was shown in Fig. 4-20, and the PN stress regarding the theoretical result of, $f_{r\_PN} \approx 1.2 \times 10^{-3} G(T)$, and experimental result of $f_{r\_PN} \approx 10^{-5}$~$10^{-6} G(T)$ was also presented.

Similar to the CRSS, the stress required to move the individual dislocation was gradually decreased with the temperature in terms of the PN stress regarding the theoretical and experimental analysis, as shown in Fig. 4-20. The value of CRSS and

the theoretical PN stress are in the same order of magnitude from 10^2~10^1 MPa within the range of 0~1500°C. The theoretical PN stress is approximately 38.6 MPa at the temperature of 1000°C. Since the value of CRSS is overestimated to analyze the single dislocation motion as discussed above, the theoretical PN stress is also too conservative, as many reports have mentioned [6,7]. Fig. 4-20 shows that the experimental PN stress is approximately 0.01~1 MPa with temperature change. The experimental PN stress is approximately 0.03~0.32 MPa at the temperature of 1000°C. This result is more plausible since the experiment actually observed the experimental value. Therefore, only the experimental PN stress is used for analysis and discussion.

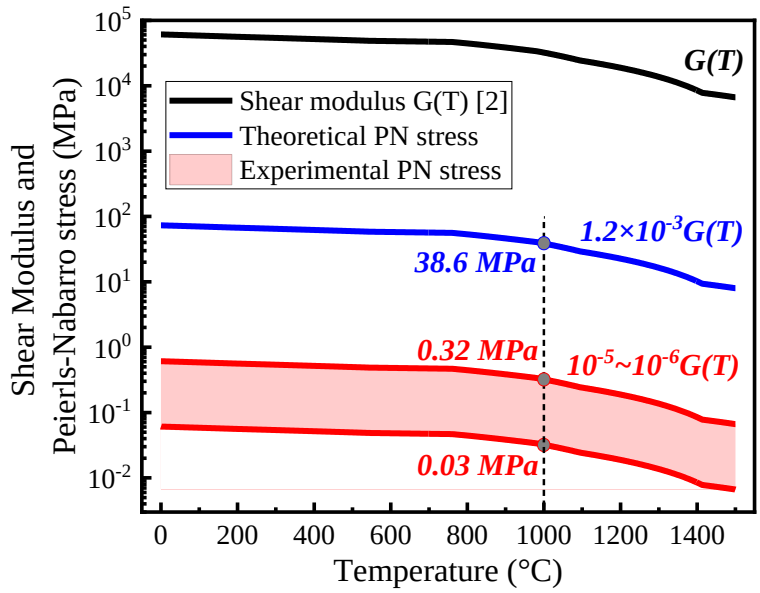

Fig. 4-20 Shear modulus and PN stress regarding theoretical and experimental analysis of solution-treated IN718 depend on the temperature.

4.7.3 Dislocation motion induced by HDPEC

As illustrated in Fig. 4-1, the temperature of HDPEC-treated samples of S4 and S5 was gradually increased during HDPEC treatment. Therefore, the experimental PN stress of the HDPEC-treated samples changes with the duration time of HDPEC. Fig. 4-21 shows that the temperature and experimental PN stress changes after HDPEC

treatment. After 3-pulses of HDPEC treatment, the temperature of samples S4 and S5 was gradually increased and reached the maximum value of 885 °C and 983 °C, respectively. Correspondingly, the experimental PN stress was gradually decreased, and the stress was in the range of 0.03 ~ 0.4 MPa at the maximum temperature. Hence, the driving force should be at the least larger than the 0.03 MPa of samples S4 and S5 to drive the motion of dislocation.

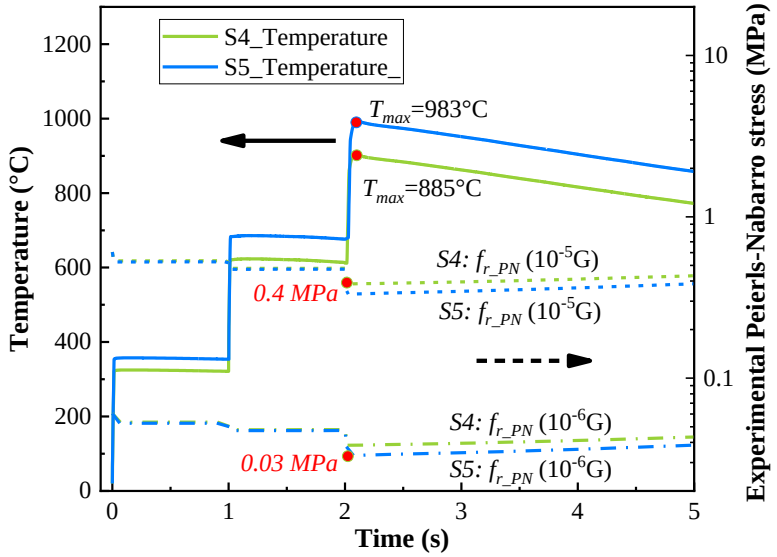

Fig. 4-21 Temperature and experimental PN stress changes of samples S4 and S5 during HDPEC treatment.

In brief, the main driving forces for dislocation motion of samples S4 and S5 were the thermal effect and EWF, as listed in Table 4-3. Due to the maximum temperature induced by HDPEC are different, the thermal effect in samples S4 and S5 is not the same, where the effect in sample S5 is larger than sample S4. Due to the same current density of 300 A/mm^2 being applied in samples S4 and S5, the driving stress caused by EW was the same of 0.86 MPa. For the resistance of dislocation, the experimental PN stress of $f_{r\_PN} \approx 10^{-5}$~$10^{-6}G(T)$ was used, and the value was approximately f_r = 0.03~0.4 MPa at the maximum temperature of samples S4 and S5 during HDPEC treatment. Therefore, the driving force of f_d = 0.86 MPa is larger than the resistance

of f_r = 0.03~0.4 MPa, and the dislocation in samples S4 and S5 can be driven by HDPEC. Due to the longer duration time in sample S5 than sample S4, more dislocation was eliminated.

Table 4-3 Driving and resistance force on dislocation of samples S4 and S5 induced by HDPEC.

Samples	**Driving force f_d**		**Resistance force f_r**
	① **Thermal** $f_{d\_T} = \frac{kT}{b^2}\ln\left(\frac{c}{c_0}\right)$ for dislocation climb.	② **EWF** Based on the specific dislocation resistivity: $f_{d\_EWF} = \left(\frac{\rho_d}{N_d}\right) en_e J/b$, for dislocation glide.	**Thermal:** Experimental PN stress: $f_{r\_PN} \approx 10^{-5}$~$10^{-6}G(T)$ T=25°C: $f_r \approx 0.06$~$0.6\ MPa$ ↓ T=885~983°C: $f_r \approx 0.03$~$0.4\ MPa$
S4: 300 A/mm^2, 40 ms	f_{d_T} (885°C)	f_{d_EWF}=0.86 MPa	
S5: 300 A/mm^2, 45 ms	f_{d_T} (983°C)	f_{d_EWF}=0.86 MPa	

Moreover, due to the EWF is proportional to current density, the driving force on samples S2, S6, and S7 was gradually decreased. The estimation of EWF was carried out based on the specific dislocation resistivity in the form of: $F_{EW} = \left(\frac{\rho_d}{N_d}\right) en_e J$. The EWF exerted on samples S2, S6, and S7 at different HDPEC treatments was approximately 0.86, 0.29, and 0.14 MPa, respectively. The results are given in Table 4-4, as marked using green background.

The resistance force of dislocation motion was estimated using the experimental PN stress of $f_{r\_PN} \approx 10^{-5}$~$10^{-6}G(T)$. Since the temperature rising of samples S2, S6, S7, and RA are similar, as presented in Fig. 4-3, only the curve of sample S7 was used to estimate the changes in resistance during HDPEC treatment, as shown in Fig. 4-22, the gray area denotes the range of resistance stress and the f_r reached the minimum value of 0.03 MPa and 0.28 MPa at the maximum temperature, also listed in Table 4-4 in the gray background.

As shown in Fig. 4-22, the EWF of sample S2 is above the gray resistance range, indicating the dislocation glide can be effectively promoted, while the driving stresses

of samples S6 and S7 are in the resistance range, implying that it may exist some dislocations that can not be driven. The results regarding the mechanical properties and microstructure evolution, as presented in the above sections, also confirm this conclusion. For the rapid annealing sample RA, which only possesses the dislocation climb promoted to thermal activation, the reduction in dislocations was weaker than the HDPEC-treated samples.

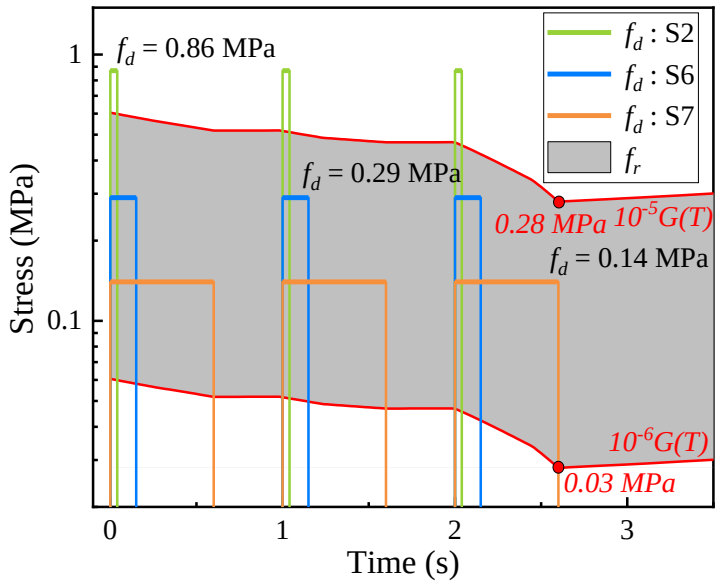

Fig. 4-22 Driving and resistance force of each sample during HDPEC treatment.

Table 4-4 Driving and resistance force on dislocation of samples S2, S6, S7, and RA.

Samples	Driving force f_d		Resistance force f_r
	① **Thermal** $f_{d\_T} = \frac{kT}{b^2}\ln\left(\frac{c}{c_0}\right)$ for dislocation climb.	② **EWF** Based on the specific dislocation resistivity: $f_{d\_EWF} = \left(\frac{\rho_d}{N_d}\right)en_eJ/b$, for dislocation glide.	**Thermal:** Experimental PN stress: $f_{r\_PN} \approx 10^{-5}\sim10^{-6}G(T)$
S2: 300 A/mm^2, 50 ms	f_{d_T}	f_{d_EWF}=0.86 MPa	T=25°C: $f_r \approx 0.06\sim0.6\ MPa$ ↓ T=1050°C: $f_r \approx 0.03\sim0.28\ MPa$
S6: 100 A/mm^2, 450 ms	f_{d_T}	f_{d_EWF}=0.29 MPa	
S7: 50 A/mm^2, 1800 ms	f_{d_T}	f_{d_EWF}=0.14 MPa	
RA: 1200°C, 20 s	f_{d_T}	--	

4.7.4 Dislocation elimination and consequent grain recovery induced by HDPEC

As examined in the previous sections, the dislocation glide can be driven by EWF, which improves the dislocation elimination. The current study has reported that the dislocation elimination caused by HDPEC treatment was realized in two main ways: the combination of dipole dislocations [8] and glide to grain boundary promoted by EWF [9], as shown in Fig. 4-23(b1,b2). These two reasons are also confirmed in this study. First of all, as shown in Fig. 4-7 and 4-11, the GND maps before and after HDPEC treatment show that the dislocations on the slip bands along the HDPEC direction tend to be easily removed while that of other dislocations was relatively difficult to be eliminated. This phenomenon may be attributed to the slip bands along the HDPEC subjected to high EWF, which promotes the dipole dislocations to combine and annihilation. Moreover, the evolution of GBs caused by HDPEC, as shown in Fig. 4-8 and 4-12, may attribute to the dislocation entanglement and disentanglement, which demonstrated the interaction between dislocations and GBs promoted by HDPEC. Although the disentanglement was also observed, the main trend is towards the entanglement, which means more dislocations were glided to GBs. Furthermore, a new way for removing dislocation induced by HDPEC was discovered. The dislocations entangled at the previous SGBs and then formed the new LAGBs or HAGBs, and hence, the dislocation was disappeared, as shown in Fig. 4-23(b3). Although the third way of dislocation elimination is similar to the second one of entangling at the existing GBs, this way is essential because it forms the new GBs, which contributes to grain refinement and causes the evident rotation of grain orientation (texture evolution), as shown in Fig. 4-9 and 4-13.

Moreover, the grain recovery induced by the traditional heat treatment mainly relies on recrystallization involving thermally activated dislocation climb, as illustrated in Fig. 4-23(a). After continuous heating, some nuclei occurred at some high-strain areas (GBs or high dislocation areas) and finally achieved grain recovery after the growth of the nucleations. In contrast, the HDPEC treatment can promote dislocation glide

rather than climb by exerting EWF on dislocation, thereby realizing rapid dislocation motion and consequent elimination through 3 ways, as shown in Fig. 4-23(b), and finally achieving the grain recovery. In addition, Ref. [10] stated: "… Climb is diffusion-controlled, and the movement of dislocations by climb is non-conservative. The process of climb is much more difficult than the glide…". Therefore we can conclude that the EWF induced dislocation glide is more efficient than the dislocation climb caused by heat treatment, which results in the high efficiency of HDPEC treatment in strain-hardening relief.

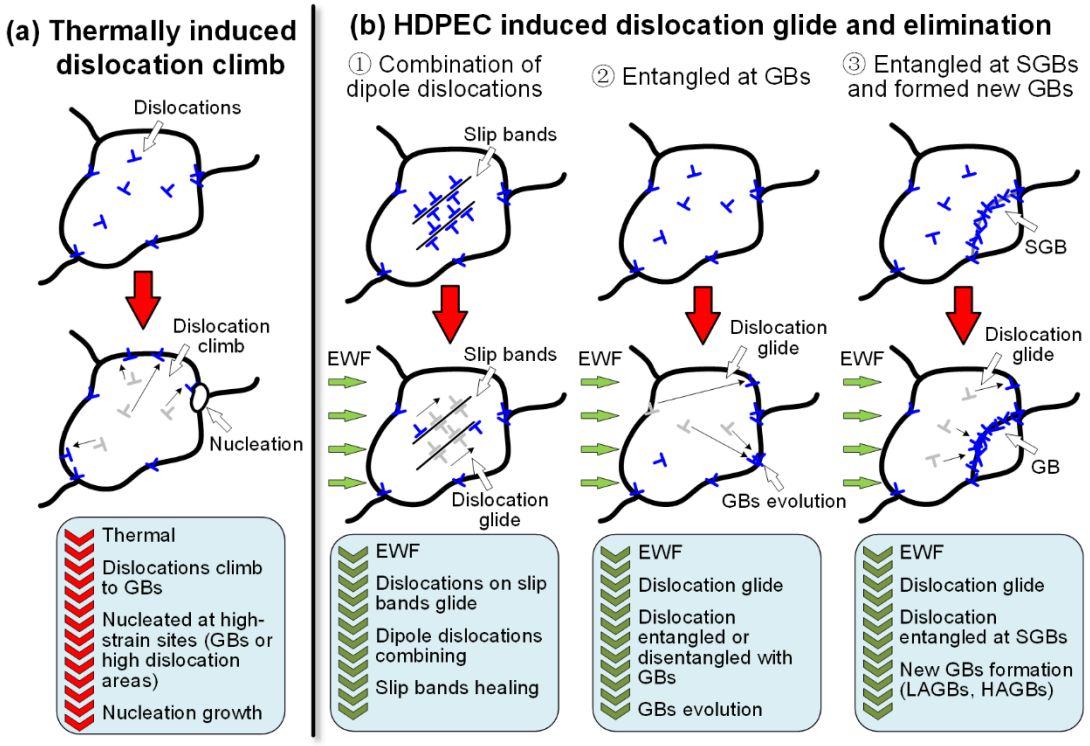

Fig. 4-23 Schematic diagrams of (a) thermal (traditional heat treatment) and (b) HDPEC induced dislocation motion and elimination.

4.8 Summary

This chapter studied the microstructure evolution induced by HDPEC using the quasi-in-situ EBSD observation. Also, the contributions of thermal and athermal effects on

strain-hardening relief in deformed IN718 caused by HDPEC treatment were clarified. The main conclusions are shown below:

1. The reported two ways for dislocation elimination caused by HDPEC: the combination of dipole dislocations on the slip bands and entanglement at GBs, were observed and confirmed by the in-situ EBSD observation. Furthermore, a new way for dislocation elimination induced by HDPEC was found: via EWF-driven dislocations entangled at the previous dislocation walls (i.e., SGBs) and then forming new GBs of LAGBs and HAGBs.
2. The grain refinement caused by HDPEC treatment was attributed to the newly formed GBs. Moreover, the formation of HAGBs results in the evident orientation change in crystals or texture evolution.
3. The mutual transformations between LAGBs and HAGBs, and HAGBs and TBs were also observed, which were related to the dislocation entanglement and disentanglement driven by HDPEC. The main transformation of GBs induced by HDPEC was towards the LAGBs→HAGBs→TBs, which causes the decrease in LAGBs and increase of TBs, resulting in the natural distribution of GBs (a stable state with low boundary energy).
4. The athermal effect plays a dominant role in strain-hardening relief than the thermal effect, indicating that the HDPEC treatment is more efficient in strain-hardening removing than the traditional heat treatment. The reason may be attributed to the EWF-induced dislocation glide is more efficient than the dislocation climb caused by the thermal effect.
5. The results of the equivalent HDPEC-treated samples show that the higher electric current density is more effective in dislocation removal and strength reduction, implying the athermal effect is associated with current density and the higher the current density the more the strain-hardening being removed.
6. The driving force for dislocation motion is proportional to current density and was approximately 0.87, 0.29, and 0.14 MPa in samples S2, S6, and S7, which

were greater than the resistance range 0.03~0.28 MPa of dislocation motion, implying the higher current density is more effective in dislocation motion. The thermal effect also helps in reducing the resistance of dislocation motion.

References

[1] E. Madhi, P.B. Nagy, D.O. Thompson, D.E. Chimenti, On the influence of cold work on resistivity variations with thermal exposure in in-718 nickel-base superalloy, in: Kingston (Rhode Island), (2010): pp. 1325–1332.

[2] E. Mirkoohi, J.R. Dobbs, S.Y. Liang, Analytical modeling of residual stress in direct metal deposition considering scan strategy, Int J Adv Manuf Technol., 106 (2020) 4105–4121.

[3] T.H. Courtney, Mechanical Behavior of Materials, McGraw Hill Education (India) Private Limited, (2012).

[4] R. Peierls, The size of a dislocation, Proc. Phys. Soc., 52 (1940) 34–37.

[5] F.R.N. Nabarro, Dislocations in a simple cubic lattice, Proc. Phys. Soc., 59 (1947) 256–272.

[6] T. Suzuki, S. Takeuchi, Correlation of Peierls-Nabarro Stress with Crystal Structure, Rev. Phys. Appl., 23 (1988) 685–685.

[7] Y. Kamimura, K. Edagawa, S. Takeuchi, Experimental evaluation of the Peierls stresses in a variety of crystals and their relation to the crystal structure, Acta Materialia, 61 (2013) 294–309.

[8] Tang Y., Hosoi A., Iwase Y., Ju Y., Effect of high-density electric current on the microstructure and fatigue crack initiation of stainless steel. Mater Trans., 54 (2013) 2085–2092.

[9] Yuichi I., The effect of high-density electric current on dislocation annihilation and fatigue crack initiation of metallic material. Master thesis, Nagoya University, (2014).

[10] J.S. Zhang, High Temperature Deformation and Fracture of Materials, 1st edition, Woodhead Publishing, Oxford, (2010), pp. 33-34.

Chapter 5 Crack initiation delay induced by HDPEC

5.1 Introduction

The previous chapters studied the effect of HDPEC on strain-hardening (i.e., plastic deformation) relief, and the mechanisms of the strain-hardening relief by HDPEC treatment were also clarified. Similarly, some plastic deformation (i.e., plastic zone) can also occur of notch materials owing to the stress concentration at the notch root during fatigue load. The plastic zone is the critical reason that causes the crack initiation and finally results in fracture of components. Therefore, this chapter aims to heal the plastic deformation ahead of the notch root and realize the enhancement of crack initiation life. The microstructure evolution near the notch root was investigated, and the mechanisms of crack initiation delay were discussed.

5.2 Experimental approach

The critical point in this section is to define the initiation of crack and divide the fatigue life N_f into crack initiation life N_i and crack propagation life N_p. As presented in Section 1.2, a lot of literature has been reported that the crack at the length range from several μm to 1 mm (depending on the size of the sample) is defined as crack initiation. But, most research has concerned that the crack length of several-grain size or several tens of μm is considered as the point of crack initiation. Hence, in this study, the crack at the length of ~ 30 μm (approximately 2-grain size) is regarded as the crack initiation point. Since this chapter aims to heal the plastic deformation at the notch root, the plastic deformation should be pre-introduced into the sample. Meanwhile, the crack should not be introduced prematurely. Hence, the fatigue cycles at 75% of crack initiation life before crack initiation were used to introduce the plastic deformation near the notch root into samples, and after then the HDPEC was applied.

The fatigue tests and HDPEC applications are listed in Table 5-1. The experiment can be separated into three groups of A, B, and C, applying different maximum stress of 350, 300, and 250 MPa, respectively. The stress ratio and frequency of the fatigue test are R=0.1 and f=25 Hz. In each group, four kinds of HDPEC treatment were carried out. The first one is without HDPEC treatment, the second and third ones apply a single HDPEC at the nominal current density of 200 A/mm^2 at different duration times of 180 ms and 240 ms, and the last one is the multi-HDPEC of 200 A/mm^2, 240 ms at every 75% N_i, as shown in Fig. 5-1. The abbreviation names of each case are denoted as A0-A3, B0-B3, and C0-C3, respectively. For each case, repeated tests of at least 2 samples were performed to ensure the credibility of the results.

The effects of HDPEC regarding the current, temperature, and stress distribution on the notch root were analyzed by FEM simulation. Meanwhile, the measurement of temperature was also given. As listed in Table 5-1, the crack initiation life of each case was studied. The changes in the plastic zone after HDPEC treatment were investigated by EBSD measurement. Finally, the summary was presented.

Table 5-1 Experimental plan of fatigue tests and HDPEC applications.

	Fatigue tests	**HDPEC applications**
Group A	σ_{max} = 350 MPa R = 0.1 f = 25 Hz	**A0:** Without HDPEC
		A1: Single pulse of 200 A/mm^2, 180 ms at 75% N_i
		A2: Single pulse of 200 A/mm^2, 240 ms at 75% N_i
		A3: Multi-pulse of 200 A/mm^2, 240 ms at every 75% N_i
Group B	σ_{max} = 300 MPa R = 0.1 f = 25 Hz	**B0:** Without HDPEC
		B1: Single pulse of 200 A/mm^2, 180 ms at 75% N_i
		B2: Single pulse of 200 A/mm^2, 240 ms at 75% N_i
		B3: Multi-pulse of 200 A/mm^2, 240 ms at every 75% N_i
Group C	σ_{max} = 250 MPa R = 0.1 f = 25 Hz	**C0:** Without HDPEC
		C1: Single pulse of 200 A/mm^2, 180 ms at 75% N_i
		C2: Single pulse of 200 A/mm^2, 240 ms at 75% N_i
		C3: Multi-pulse of 200 A/mm^2, 240 ms at every 75% N_i

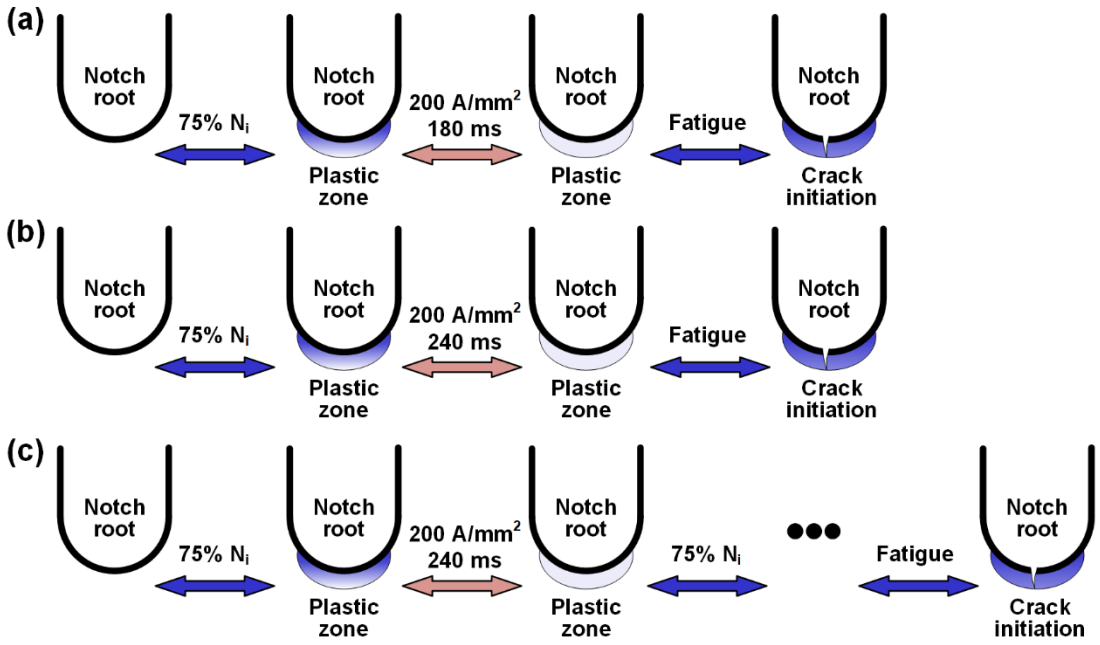

Fig. 5-1 Schematic diagram of crack initiation delay by HDPEC treatment. (a) Single pulse of 200 A/mm^2, 180 ms at 75% N_i, (b) single pulse of 200 A/mm^2, 240 ms at 75% N_i, and (c) multi-pulse of 200 A/mm^2, 240 ms at every 75% N_i.

5.3 FEM simulation results

5.3.1 Current density field

The FEM model and current density field were presented in Fig. 5-2. The model is dispersed using a triangular element; the fine mesh near the notch and coarse mesh at other areas were used to ensure accuracy while saving the simulation time. The FEM model contains 1172 nodes and 2181 elements, as shown in Fig. 5-2(a), and the enlarged figure near the notch root was also presented. Since all the HDEPC treatments use the same current value of 200 A/mm^2, the current density distribution near the notch root should be the same. Hence, the current density field at the current value of 200 A/mm^2 was presented in Fig. 5-2(b), and the enlarged figure at the notch root was also given. The maximum current density near the notch root was approximately 454 A/mm^2.

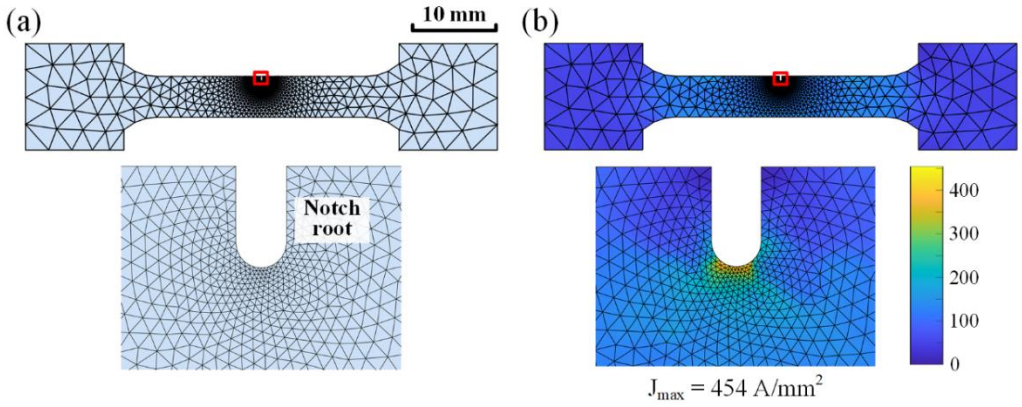

Fig. 5-2 FEM model and current density field of the notched sample. (a) FEM model and enlarged figure near the notch root, and (b) current density field and enlarged figure near the notch root at the current condition of 200 A/mm^2.

5.3.2 Temperature field

The simulated temperature curves at the notch root A and center point B of the HDPEC conditions of 200 A/mm^2 and different duration times of 180 and 240 ms were shown in Fig. 5-3. Due to the concentration behavior of current density at notch root, the heat near the notch root is higher than in other zones. The maximum temperature at the notch root A and center point B by FEM simulation are 787 and 706°C at the HDPEC condition of 200 A/mm^2 and 180 ms, and 1006 and 976°C at the HDPEC condition of 200 A/mm^2 and 240 ms. Meanwhile, the temperature measurement using the thermal sensors was also carried out. Since the thermal sensors detected a large area of the sample and presented the mean temperature of the detected area, the maximum temperature of the measured results is less than the temperature at the notch root by FEM simulation. The maximum temperature of the measured results of those two HDPEC conditions is 699 and 936°C, respectively. As illustrated in Fig. 5-3(c,d), the measured temperature is comparable with the simulated results at center point B and less than the results at notch root A. The temperature field and the enlarged figure at different HDPEC treatments are shown in Fig. 5-3(e,f). The maximum temperature happened near the notch root, and the maximum values

were 787 and 1006°C, respectively.

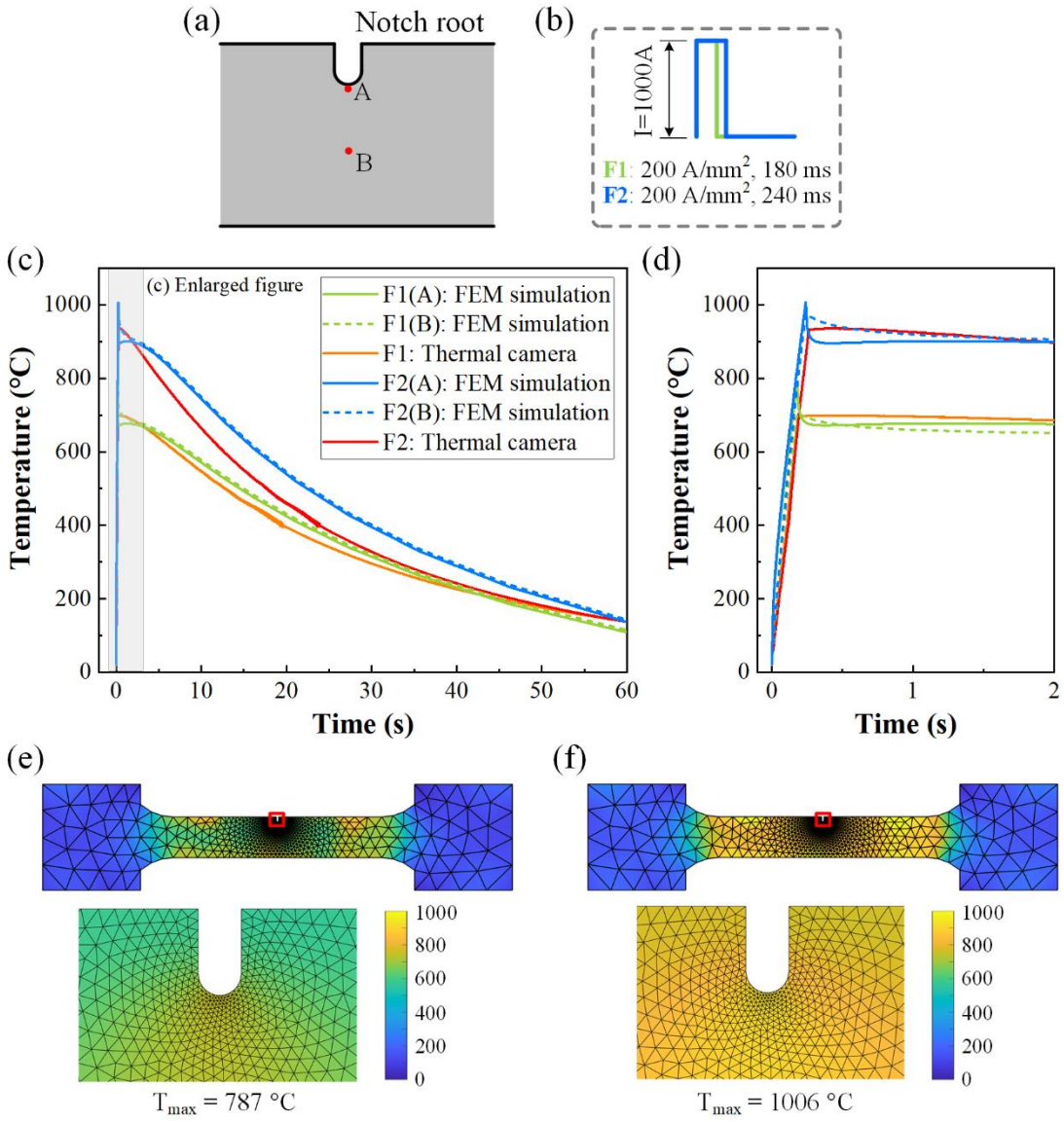

Fig. 5-3 Temperature estimation by FEM simulation and measurement. (a) Schematic diagram of the sample near the notch, (b) conditions of HDPEC treatment, (c) temperature-time curves, and (d) enlarged figure in (c). Temperature field at the maximum value with the enlarged figure of HDPEC treatment at the conditions of (e) 200 A/mm^2 and 180 ms, and (f) 200 A/mm^2 and 240 ms.

5.3.3 Thermal stress field

Since the concentration behavior of current flows at the notch, the over-heating happened near the notch. Due to the thermal gradient, the thermal stress near the notch occurred. Fig. 5-4 shows the thermal compressive stress field at the maximum value of HDPEC conditions of 200 A/mm^2 and different duration times of 180 and 240 ms. The maximum thermal stresses at the notch root of each case are 539 MPa and 752 MPa, respectively.

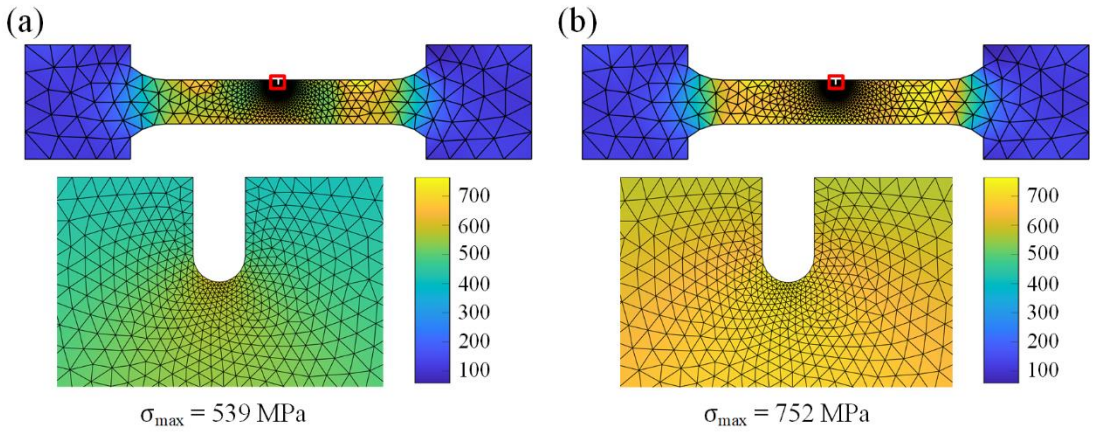

Fig. 5-4 Thermal stress estimation by FEM simulation. Thermal stress field and the enlarged figure at the HDEPC treatment of (a) 200 A/mm^2, 180 ms and (b) 200 A/mm^2, 240 ms.

5.4 Crack initiation delay induced by HDPEC

The crack initiation life of each case is shown in Fig. 5-5, and the S-N curve is also presented. The figure evidently depicted that the crack initiation was prevented by the HDPEC treatment, and the effect tends to increase at the low fatigue stress σ_{max}.

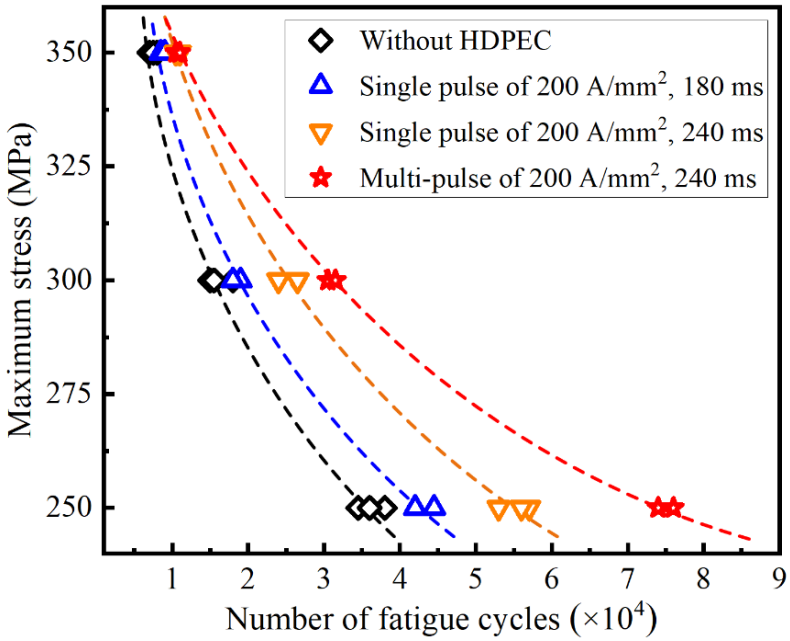

Fig. 5-5 S-N curves and the crack initiation life of notched IN718 with and without HDPEC treatment.

Table 5-2 Crack initiation life of each case.

	HDPEC applications	Crack initiation life (cycles)	Rate of increase (%)
Group A	**A0:** Without HDPEC	7500	--
	A1: Single pulse of 200 A/mm², 180 ms at 75% N_i	8500	13.3%
	A2: Single pulse of 200 A/mm², 240 ms at 75% N_i	10500	40.0%
	A3: Multi-pulse of 200 A/mm², 240 ms at every 75% N_i	10500	40.0%
Group B	**B0:** Without HDPEC	16000	--
	B1: Single pulse of 200 A/mm², 180 ms at 75% N_i	18500	15.6%
	B2: Single pulse of 200 A/mm², 240 ms at 75% N_i	25500	59.4%
	B3: Multi-pulse of 200 A/mm², 240 ms at every 75% N_i	31000	93.8%
Group C	**C0:** Without HDPEC	36000	--
	C1: Single pulse of 200 A/mm², 180 ms at 75% N_i	43000	19.4%
	C2: Single pulse of 200 A/mm², 240 ms at 75% N_i	55500	54.2%
	C3: Multi-pulse of 200 A/mm², 240 ms at every 75% N_i	75000	108.3%

The crack initiation life without HDPEC treatment at the maximum stress σ_{max}=350, 300, and 250 MPa was 7500, 16000, and 36000 cycles, respectively, as presented in

Table 5-2. The crack initiation life was extended to 8500, 18500, and 43000 cycles after the single HDPEC treatment at the condition of 200 A/mm^2 and 180 ms, and increased approximately 13.3%, 15.6%, and 19.4%, respectively. In addition, the longer crack initiation life was realized at the HDPEC condition of 200 A/mm^2 and 240 ms, and the crack initiation life was reached 10500, 25500, and 55500 cycles, respectively. The corresponding increase rates were 40.0%, 59.4%, and 54.2%, respectively. For the multi-pulsed cases at the HDPEC condition of 200 A/mm^2 and 240 ms, the crack initiation life was highly extended to 10500, 31000, and 75000 cycles, and the increase rate reached 40.0%, 93.8%, and 108.3%, respectively. Since the crack was already initiated at the second 75% N_i testing at the maximum stress σ_{max}=350, the crack initiation life of the multi-pulsed and the single pulsed cases at 200 A/mm^2 and 240 ms was the same (10500 cycles, increased 40.0%).

5.5 Microstructure evolution induced by HDPEC

The EBSD measurement was conducted on the Group B of σ_{max}=300MPa, as listed in Table 5-3, to investigate the microstructure evolution near the notch root after HDPEC treatment. Sample S0 is the initial sample without fatigue loading and HDPEC treatment. Sample S1 represents the fatigue-loaded sample at 75% N_i without HDPEC treatment, while sample S2 is fatigue-loaded and then HDPEC-treated at the condition of 200 A/mm^2 and 240 ms. Sample S3 is the fatigue-loaded and HDPEC-treated case, and after then the fatigue loading was carried out till crack initiation.

Table 5-3 Conditions of the samples for EBSD measurement.

Samples	Fatigue tests	HDPEC applications	Notes
S0	--	--	--
S1	75% N_i	--	--
S2	75% N_i	200 A/mm^2, 240 ms	--
S3	75% N_i	200 A/mm^2, 240 ms	To crack initiation

5.5.1 EBSD orientation maps and BC maps

The EBSD orientation maps and corresponding BC maps were presented in Fig. 5-6. The EBSD maps covered a range of 200×100 μm^2 near the notch root with a scanning step size of 0.5 μm. The loading and current directions are towards the vertical. For the initial sample S0, the uniformed microstructure was observed with a mean grain size of 16.3 μm near the notch. After fatigue loading of sample S1, the grain morphology was almost unchanged with a mean grain size of 15.9 μm. The grain size tends to be refined after HDPEC treatment, as shown in Fig. 5-6(c), the grain size was decreased to 14.1 μm. For sample S3, the grain size tends to increase after crack initiation. Several micro-cracks were initiated near the notch root, and the maximum length of which was approximately ~38 μm, as shown in Fig. 5-6(h).

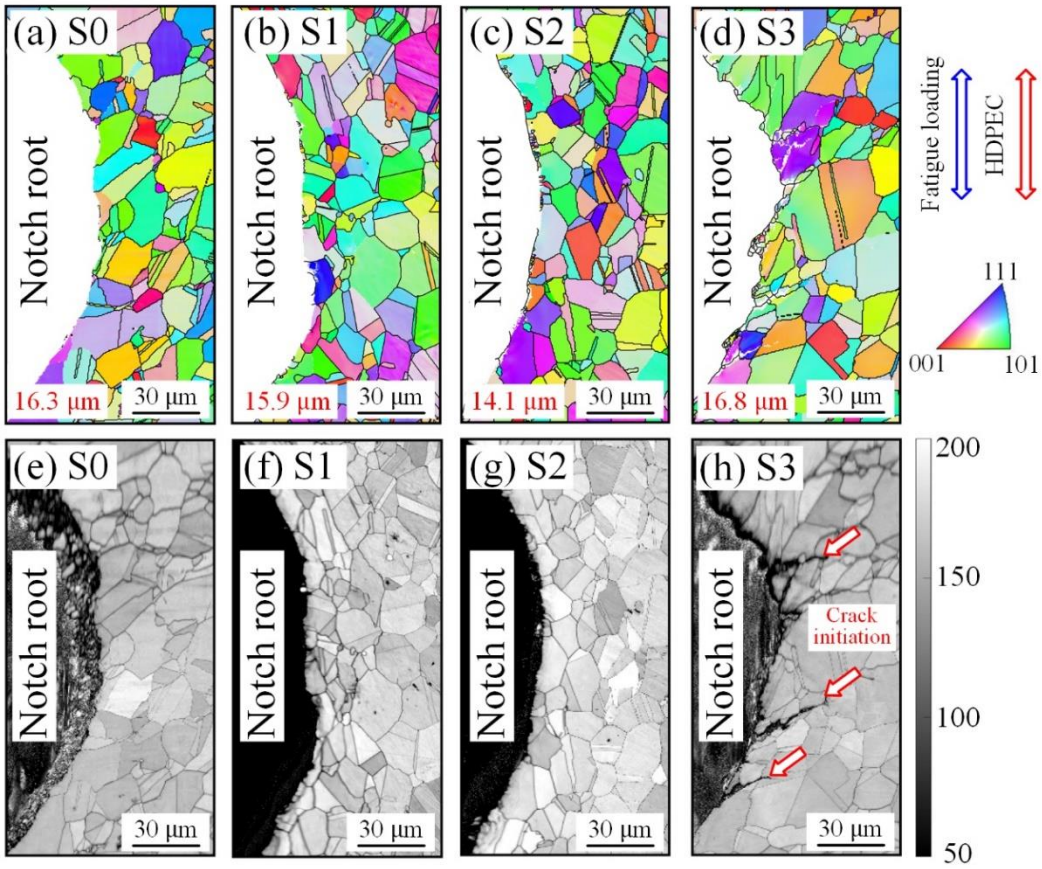

Fig. 5-6 EBSD orientation maps with the mean grain size of (a) S0, (b) S1, (c) S2, and (d) S3. (e-h) Corresponding BC maps of each sample.

5.5.2 GND maps

To investigate the plastic deformation evolution induced by HDPEC treatment near the notch root, the GND maps corresponding to the EBSD maps were presented, as presented in Fig. 5-7. For the initial sample S0, the uniformed GND map (blue color) was observed, and the maximum GND density near the notch root was approximately 2.9 × 10^{14} m^{-2}. After fatigue loading at 75% N_i of the σ_{max}=300MPa case, the GND density near the notch root was increased, and the maximum GND density reached 7.2 × 10^{14} m^{-2}, as illustrated in Fig. 5-7(b). Many high GNDs areas were observed, as marked in Fig. 5-7(b), and the affected area only spanned 1~2 grains. After HDPEC treatment at 200 A/mm^2 and 240 ms, the maximum GND density near the notch root was decreased to approximately 4.4 × 10^{14} m^{-2}, indicating the HDPEC can promote the dislocation elimination near the notch root. After the following fatigue loading till crack initiation, the maximum GND density was increased to 1.06 × 10^{15} m^{-2} near the initiated cracks.

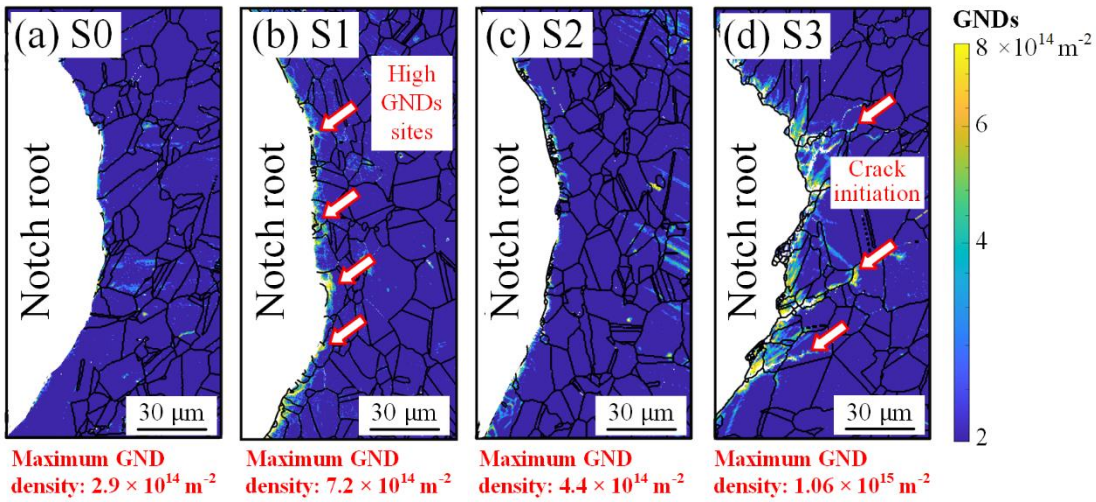

Fig. 5-7 GND maps corresponding to the EBSD orientation maps of (a) S0, (b) S1, (c) S2, and (d) S3 with the maximum GND density.

5.6 Discussion

The crack initiation life was significantly enhanced by HDPEC treatment. For the single HDPEC-treated cases at the condition of 200 A/mm^2 and 180 ms, the average increase in crack initiation life was more than 16%. In contrast, the average increase reached 51.2%, increasing the duration time to 240 ms. For the multi-HDPEC treated cases, the maximum increase rate in crack initiation life was 108.3% at the fatigue stress of σ_{max}=250 MPa. The microstructure characteristics by EBSD measurement show that the fatigue-introduced plastic zone only affected ~ 2-grain area ahead of the notch root, and the dislocations (e.g., plastic deformation) were removed evidently by HDPEC treatment at the condition of 200 A/mm^2 and 240 ms. The crack initiation was delayed correspondingly with releasing the dislocations near the notch root. The healing effect was related to the current concentration near the notch root. The maximum current density of approximately 454 A/mm^2 occurred at the notch root, as illustrated in Fig. 5-2(b). Moreover, the current density field fairly covered the plastic zone, which promoted the dislocation motion and finally resulted in the elimination of dislocations. Furthermore, the simulation results of temperature and thermal stress show that the temperature can reach 1000°C, and the thermal compressive stress near the notch root was 752 MPa at the HDPEC condition of 200 A/mm^2 and 240 ms. Both the thermal and thermal stress during HDPEC treatment may be beneficial to the healing of the potential micro-cracks after 75% N_i of fatigue loading and thereby enhancing the life of crack initiation.

5.7 Summary

The enhancement of crack initiation life by HDPEC treatment was carried out in this chapter. The microstructure evolution near the notch root was observed by EBSD measurement to investigate the mechanisms, and meanwhile, the FEM simulation was also carried out. The main conclusions are presented below:

1 The average increase in crack initiation life at the fatigue stress of σ_{max}=250~350 MPa was more than 16% after HDPEC treatment of 200 A/mm^2 and 180 ms, and that value reached 51.2% with increasing the duration time of HDPEC to 240 ms. For the multi-HDPEC treated cases, the crack initiation life was highly enhanced and the rate of increase reached 108.3% at the fatigue stress of σ_{max}=250 MPa.

2 The GND maps show that the fatigue-introduced plastic zone only affected ~2-grain area ahead of the notch root.

3 The current density field covered the plastic zone, which promoted the dislocation motion and finally eliminated dislocations. The dislocation removal is the main reason that causes the delaying of crack initiation.

4 Moreover, the thermal and thermal stress during HDPEC treatment may also be beneficial to crack initiation delay by healing the potential micro-cracks created after 75% of crack initiation life.

Chapter 6 Conclusions

This dissertation successfully achieved the relief of strain hardening (i.e., plastic deformation) of deformed IN718 by HDPEC treatment and realized formability enhancement. The mechanisms of HDPEC-induced strain-hardening relief (or healing of plastic deformation) and microstructure evolution were clarified. Furthermore, the effect of HDPEC on the recovery of the fatigue-introduced plastic zone (i.e., plastic deformation) ahead of notched materials was also studied, and the delaying of crack initiation was successfully achieved. The main conclusions are shown below.

The strain hardening of the deformed IN718 was rapidly and effectively relieved by HDPEC treatment, and the formability was successfully enhanced. Furthermore, the results show that elimination of dislocation by HDPEC treatment was the dominant reason, while grain size and texture evolution were the side effects in strain-hardening relief. Meanwhile, the residual stress was also alleviated by removing dislocations after HDPEC treatment. The microstructure characteristics show that the grain refinement was achieved after HDPEC treatment and the grain morphology of the HDPEC-treated samples tends to possess random orientation and equiaxed morphology. Moreover, the homogeneous and large dimples were obtained in the HDPEC-treated sample after the tensile test, indicating the formability was enhanced. The slip bands, microvoids, and debonding in the deformed sample were healed after HDPEC treatment.

The microstructure evolution induced by HDPEC was clarified by the quasi-in-situ EBSD observation. The dislocation motion and elimination caused by HDPEC were directly observed in this study. The reported two ways of dislocation elimination caused by HDPEC, i.e., the combination of dipole dislocations on the slip bands and entanglement at GBs, were observed and confirmed. In particular, a new way for dislocation elimination induced by HDPEC was found: via EWF-driven dislocations entangled at the previous dislocation walls (i.e., SGBs) and then forming new GBs of

LAGBs and HAGBs. The newly formed GBs result in grain refinement and the formation of HAGBs contributes to the evident orientation changes in crystals or texture evolution caused by HDPEC treatment. In addition, the mutual transformations between LAGBs and HAGBs, and HAGBs and TBs were also observed, which were related to the dislocation entanglement and disentanglement driven by HDPEC. The net transformations of GBs were towards the direction of LAGBs→HAGBs→TBs, which causes the decrease in LAGBs and increase of TBs and thereby realizes the natural distribution of GBs (a stable state with low boundary energy). Moreover, the thermal and athermal (i.e., EWF) effects as the driving forces for dislocation motion were clarified. The EWF provides approximately 0.86 MPa at the current density of 300 A/mm^2 on dislocation, which is larger than the resistance of dislocation motion of 0.03~0.4 MPa calculated by experimental Peierls-Nabarro stress, implying the dislocation can be driven by EWF.

Moreover, the contributions of thermal and athermal effects on strain-hardening relief in deformed IN718 by HDPEC treatment were elucidated. The results show that the athermal effect plays a dominant role in strain-hardening relief than the thermal effect, indicating the HDPEC treatment is more efficient in strain-hardening eliminating than the traditional heat treatment. The reason may be attributed to the EWF-induced dislocation glide being more efficient than the dislocation climb activated by the thermal effect. Furthermore, the high current density is more effective in dislocation removal than low current density, implying the athermal effect is associated with the electric current density and the higher the current density the larger the EWF created. The high EWF is more easily helps the dislocation to overcome the resistance to move, thereby realizing dislocation annihilation and strain-hardening relief. Moreover, the thermal effect also helps in reducing the resistance of dislocation motion.

The crack initiation life after HDPEC treatment was evidently enhanced. The average increase in crack initiation life at the fatigue stress σ_{max}=250~350 MPa was

more than 16% after HDPEC treatment of 200 A/mm^2 and 180 ms, and that value reached 51.2% with increasing the duration time of HDPEC to 240 ms. For the multi-HDPEC treated cases, the crack initiation life was highly enhanced and the rate of increase reached 108.3% at the fatigue stress σ_{max}=250 MPa. The microstructure characteristics show that the fatigue-introduced plastic zone only affected ~2-grain area ahead of the notch root, and the dislocations at the plastic zone were removed evidently by HDPEC treatment. The current density field near the notch root covered the plastic zone, which promoted the dislocation motion and eliminated dislocations. The dislocation removal is the main reason that finally causes the delaying of crack initiation. Moreover, the thermal and the caused thermal stress during HDPEC treatment may also be beneficial to crack initiation delay by healing the potential micro-cracks created after 75% of crack initiation life.

Hence, due to the fast and efficient features in dislocation elimination and strain-hardening relief, HDPEC treatment can be applied to the metal forming field to realize the rapid forming of metallic materials. Also, the HDPEC treatment is applicable to prevent crack initiation and achieve the long-time durability and reliability of engineered components or structures, and then save resources.

The original contributions of this thesis are summarized below:

1. The strain hardening was successfully eliminated by HDPEC treatment, and the results indicate that the dislocation elimination induced by HDPEC was the dominant reason, while grain size and texture evolution were the side effects in strain-hardening relief.
2. A new way for dislocation elimination induced by HDPEC was found in this thesis: via EWF-driven dislocations entangled at the previous dislocation walls (i.e., SGBs) and then forming new GBs of LAGBs and HAGBs.
3. The athermal effect (i.e., EWF) was confirmed to be more dominant in strain-hardening relief than the thermal effect (i.e., Joule heating). The high electric

current was more effective in reducing dislocation density, which attributes to the large EWF that helps dislocation overcome resistance to motion and realize annihilation.

4. The HDPEC-induced grain recovery relies on EWF-promoted dislocation glide and elimination, which is more efficient than the recrystallization-involved dislocation climb activated by the traditional heat treatment.
5. The crack initiation life was highly enhanced (maximum reached 108.3%) by HDPEC treatment, and the reason mainly relied on dislocation elimination at the plastic zone induced by HDPEC.

Given below is a summary of future work that can be conducted in this field.

1. Since the FEM simulation presented in this thesis does not consider the effect of pre-deformation on the material properties and only takes the thermoelastic model for simulation, a more advanced FEM simulation using realistic material properties and the thermo-elastoplastic constitutive relationship could be conducted.
2. The crystal plasticity finite element method (CPFEM) could be applied to study the strain-hardening behavior and the relief of strain-hardening induced by HDPEC.
3. The in-situ transmission electron microscope (TEM) observation could be carried out to study the individual dislocation motion behavior and establish the EWF-dislocation motion relationships.
4. The in-situ EBSD observation can be conducted in studying the plastic zone evolution of notched materials after fatigue load and the healing process by HDEPC treatment.

Acknowledgments

First of all and most importantly, I would like to express my sincere gratitude to my supervisor Prof. Ju Yang, for his endless support and guidance in every aspect of my Ph.D. student life. His foresight and suggestions towards research have helped me to complete my studies successfully. I appreciate him giving me the freedom in my research to think independently and providing me the opportunity to try different ideas. It is my honor to have him as my supervisor, and I believe working with him will be the most valuable experience in my life.

I would like to express my sincere gratitude to the reviewers, Prof. Umehara Noritsugu and Prof. Okumura Dai, for their valuable comments and suggestions on this dissertation.

I am deeply grateful to Lectr. Toku Yuhki for his assistance at every stage of my research work. His knowledge and expertise are instrumental in helping me accomplish my goals. I would like to extend my appreciation to Assistant Prof. Kimura Yasuhiro for his warm help and collaboration in my experiments. The fruitful exchanges and discussions with him have been of great help to my research.

Many thanks to all colleagues and friends of Ju Lab. for their support. The clash of diverse cultures and fruitful exchanges always lead to innovative ideas. Special thanks to the graduated student Mr. Rui Iwase who selflessly taught me the primary experimental method. Many thanks to Assistant Prof. Cui Yi, who has given many insightful comments and suggestions for my research. Many thanks to Dr. Yoon Sungmin, who has shared many experiences regarding study and life. I also would like to offer my special thanks to visiting scholar Ms. Li Shaoli, Dr. Xie Yiyuan, Dr. Yan Keyi, Dr. Tong Bo, Dr. Zhao Minji, Mr. Wang Zizheng, Mr. Ali Sameh, Ms. Fu Xiaorong, Mr. Mahmud MD Sultan, Mr. Yu Xiaoming, Mr. Marumoto Yuki, Mr. Yan Xinming, Mr. Yuan Jing, who always gave me confidence and encouragement during my Ph.D. life. Also, many thanks to Ms. Ueno Satsuki for helping with the many

complex paperwork.

Many thanks to Mr. Jinno Takaaki and Mr. Nakakimu Tadafumi in the Technical Center of Nagoya University for EBSD measurement and sample processing.

I also gratefully acknowledge the Ministry of Education, Culture, Sports, Science and Technology (MEXT) for supporting my study in Japan.

My sincere thanks to my parents for their tremendous support, encouragement, and love. I wish what I have achieved today can make them feel proud, and I will spend all my life bringing them more honor and happiness.

Shaojie GU

Nagoya University

March, 2022

Appendix 1: Driving force of thermal and athermal effects on dislocation motion

1. Thermal effect (Joule heating)

When electric current flows through materials, Joule heating occurs since the driven electrons collide with atoms that causing an increase in atomic thermal vibrations. The equation shown below is commonly applied to evaluate the temperature rise by electric current [1].

$$\Delta T = \frac{J^2 t}{c\rho\sigma} \qquad (\mathrm{A1}-1)$$

where J is the current density, t the duration time of electric current, c the specific heat capacity, ρ density of the material, and σ electrical conductivity.

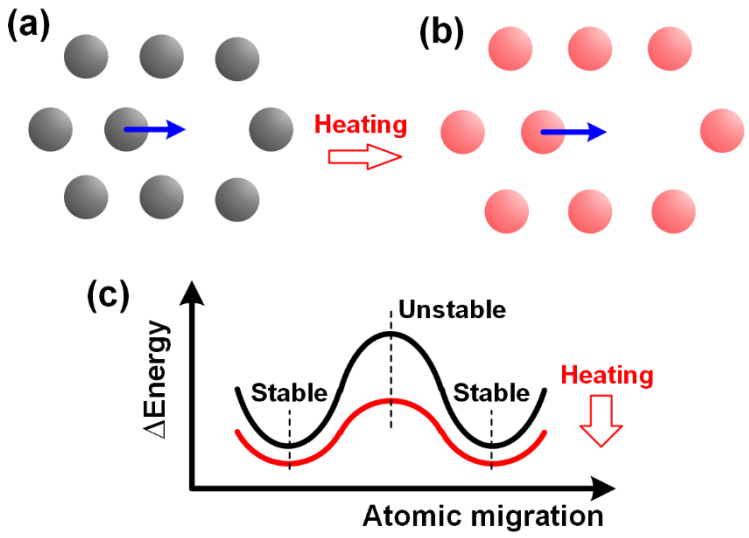

Fig. A1-1 Schematic diagram of thermal effect on atomic migration. Atoms arrangement with a vacancy (a) before and (b) after heating, and (c) migration energy from a stable position to another.

According to Eq. (A1-1), the temperature rise is related to the quadratic of current

density and its duration time, $\Delta T \propto J^2 t$, means the current density is more sensitive to temperature. Moreover, many studies have used this equation to estimate the temperature after electric current treatment. As this equation ignores the dissipation of heat (e.g., heat convection and heat radiation), it results in an overestimation of the result. In addition, the sample is instantaneously heated during electric current treatment, and hence, the thermal effect is a non-directional variable.

The most significant effect of the thermal is to increase the thermal vibration of the atoms and soften the material. Fig. A1-1 illustrated that the energy of moving an atom from a stable position to another stable position is decreased by heating, implying the lattice resistance was reduced by thermal. Hence, the material is softened and is more likely to yield under load. More profoundly, dislocations are more likely to be activated and moved at high temperatures, which means that the thermal effect reduces the resistance force of dislocation movement.

Moreover, the other important effect of the thermal is to promote dislocation climb to annihilation, which provides the driving force for microstructure evolution. For instance, at the elevated temperature, edge dislocation can climb towards the perpendicular direction of their glide direction, as shown in Fig. A1-2, which is promoted by the vacancy diffusion (or atom diffusion). Dislocation climb is diffusion-controlled, and the movement of dislocations by climb is non-conservative. The driving force for dislocation climb was proposed [2] below:

$$f = \frac{kT}{b^2} \ln\left(\frac{c}{c_0}\right) \qquad (\mathrm{A1}-2)$$

where k is the Boltzmann constant, T temperature, b Burgers vector, c and c_0 are the vacancy concentration and thermodynamic equilibrium concentration of vacancy in crystal free of stress.

Hence, according to Eq. (A1-2), with increasing the temperature, the driving force for dislocation climb by thermal activation was enhanced. Due to the dislocation climb is related to the atom diffusion, the dislocation movement is non-directional.

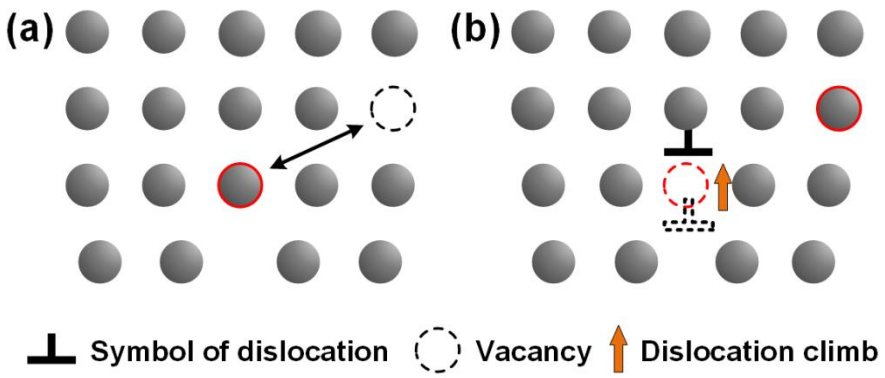

Fig. A1-2 Thermally activated dislocation climb by vacancy diffusion.

2. Athermal effect (electron wind force)

The athermal effect is related to the conducted electrons colliding with the atoms and exerting a force on atoms, which is the so-called EWF. Theoretical estimates of EWF on the dislocation motion can be divided into two general equations: (1) the equation concerning the dislocation resistivity [3] and (2) the other one related to quantum mechanics [4].

Nabarro [3] first proposed the equation of EWF based on the specific dislocation resistivity in the form of:

$$F_{EW} = \left(\frac{\rho_d}{N_d}\right) e n_e J \qquad (A1-3)$$

where ρ_d is the electrical resistivity caused by dislocation, N_d the dislocation density, e the electron charge, n_e the electron density, J the current density.

Moreover, based on the quantum mechanics of energy transformation by electron-atom interaction, Kravchenko [4] first presented the kinetic analysis of the EWF acting on dislocations by conducted electrons.

$$F_{EW} = \alpha b p_F n_e (v_e - v_d) \qquad (A1-4)$$

where α is a constant, b the Burgers vector, p_F the Fermi momentum, $v_e = J/(en_e)$ and v_d are the velocity of electron and dislocation, respectively.

As shown in Eq. (A1-4), electron velocity v_e is related to current density J, and

hence, F_{EW} is associated with the current density. In addition, the equation also considered the moving dislocation (dislocation velocity, v_d), while the Eq. (A1-3) based on the specific dislocation resistivity does not include the dislocation motion. The direction of EWF is along with the direction of electron flow and reverse with the current direction, as shown in Fig. A1-3(a). However, the motion direction of dislocation is the same as the current direction, while is contrary to the electron flow. As shown in Fig. A1-3, when the direction of current towards the right (electron flow is towards the left), all atoms are subjected to an EWF towards the left due to the impact of the electrons on the atoms. The atom to the right of the vacancy, marked in a red circle, can easily move to the left to fill the vacancy. In this case, the dislocation moves one atom's distance to the right, which is contrary to the current direction.

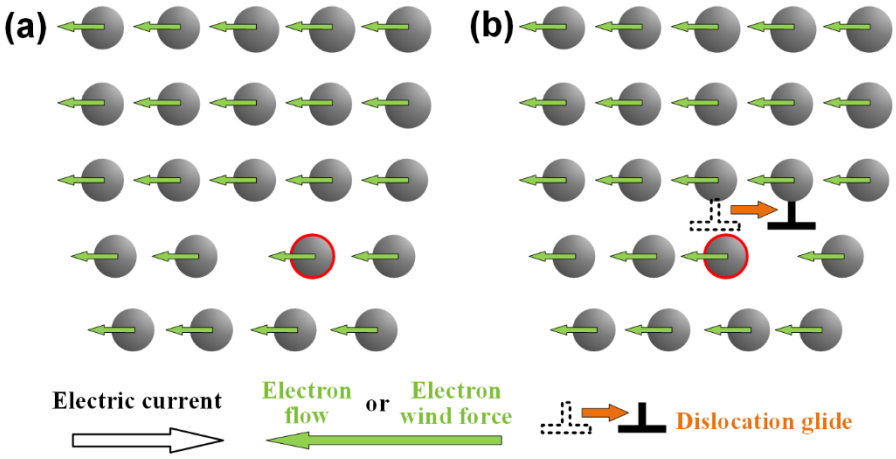

Fig. A1-3 Schematic diagram of electron wind force near dislocation causes the dislocation motion. (a) Before and (b) after dislocation motion induced by electric current treatment.

References

[1] H. Conrad, A.F. Sprecher, The electroplastic effect in metals, in: Dislocations in Solids, Elsevier, (1989): pp. 497–541.

[2] J.-S. Zhang, High Temperature Deformation and Fracture of Materials, 1st edition, Woodhead Publishing, Oxford, (2010).

[3] F.R.N. Nabarro, Theory of Crystal Dislocations, Clarendon Press, Oxford, (1967).

[4] V.Y. Kravchenko, Effect of directed electron beam on moving dislocations, Journal of Experimental and Theoretical Physics, 24 (1967) 1135–1142.

Appendix 2: FEM simulation

After applying the electric current to the metallic materials, it will cause the thermal effect due to the Joule heating, and thermal stress may also be aroused due to the inhomogeneous heating. Thus, the FEM simulation in this study involves three parts: the first one is the electrostatic field analysis since the model is subjected to a simple electric potential without any charges; the second part is the thermal field analysis because the Joule heating happened; and the last one is the stress field analysis, which is caused by the inhomogeneous thermal expansion especially for the notched samples contain the geometric discontinuity. First of all, the governing equations of each part are presented. Furthermore, the procedure was developed on the commercial software MATLAB based on the FEM theory (governing equations), and the graphical user interface (GUI) was also presented for easy access.

1. Electric field analysis

1.1 Governing equations

The governing equation of the static electric problem contains the conservation equation of current density, Ohm's law, and the relationship between electric field and electric potential [1,2], as shown below:

$$\nabla \cdot \boldsymbol{J} = 0 \qquad (\mathrm{A2}-1)$$

$$\boldsymbol{J} = \sigma_{EC}\boldsymbol{E} \qquad (\mathrm{A2}-2)$$

$$\boldsymbol{E} = -\nabla\Phi \qquad (\mathrm{A2}-3)$$

where parameters ∇, $\boldsymbol{J}$, σ_{EC}, $\boldsymbol{E}$, and Φ are Nabla operator ($\nabla = \partial/\partial x\boldsymbol{i} + \partial/\partial y\boldsymbol{j}$), electric current density (A/mm^2), electric conductivity (S/m), electric field (V/m) and electric potential (V), respectively.

From the above Eq. (A2-1, A2-2, A2-3), the equation for the static electric problem

can be obtained as:

$$-\nabla \cdot (\sigma_{EC} \nabla \phi) = 0 \qquad (A2-4)$$

Since the model is two-dimensional, the equation can be rewritten as:

$$\sigma_{EC} \frac{\partial^2 \phi}{\partial x^2} + \sigma_{EC} \frac{\partial^2 \phi}{\partial y^2} = 0 \qquad (A2-5)$$

1.2 Boundary conditions

Fig. A2-1 shows the application of the electric current, where current flows along the horizontal with a current density of J_0. The boundary conditions can be expressed in mathematical equations, as:

$$\begin{cases} \nabla \phi|_{\Gamma_1} = \dot{\phi}^0 = -J_0/\sigma_{EC} \\ \nabla \phi|_{\Gamma_2} = 0 \end{cases} \qquad (A2-6)$$

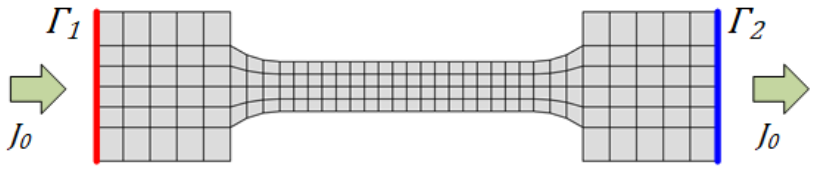

Fig. A2-1 Boundary conditions of electric field analysis.

1.3 Element normalization and shape functions

The normalized quadrilateral elements were usually used to facilitate matrix assembly and numerical integration, as shown in Fig. A2-2. A two-dimensional Jacobian coordinate transformation matrix J_a of the planar two-dimensional element was used for the normalization, as shown in Eq. (A2-7).

$$J_a = \frac{\partial(\boldsymbol{x}, \boldsymbol{y})}{\partial(\boldsymbol{\xi}, \boldsymbol{\eta})} \qquad (A2-7)$$

For the normalized quadrilateral elements, a second-order shape function was

chosen [2,3], as:

$$N_i = \frac{1}{4}(1+\xi_i\xi)(1+\eta_i\eta) \qquad (A2-8)$$

So, the electric potential ϕ can be expressed as:

$$\phi = N_1\phi_1 + N_2\phi_2 + N_3\phi_3 + N_4\phi_4 = N_i\phi_i = N\phi^e \qquad (A2-9)$$

where, $N_1 \sim N_4$ and $\phi_1 \sim \phi_4$ are the shape function and electric potential at the 4 nodes of the normalized quadrilateral element.

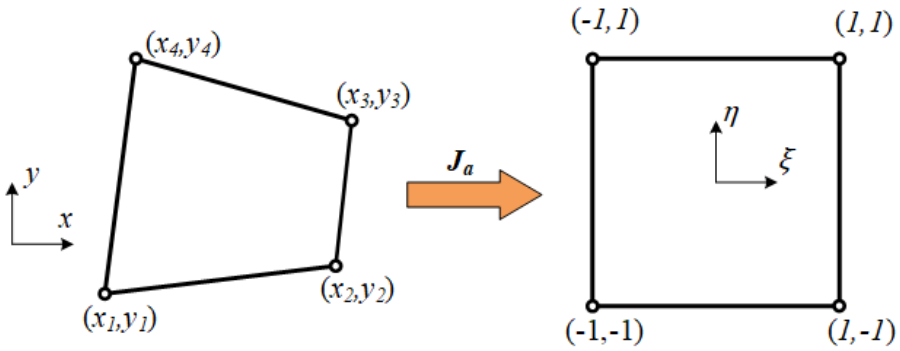

Fig. A2-2 The normalization of the quadrilateral element.

1.4 Finite element discretization and variational principle

Based on the Galerkin principle, we can construct the total potential energy of the system containing the boundary conditions [2,3], as:

$$\Pi(\phi) = \iint_D \left\{ \frac{\varepsilon}{2}\left[\left(\frac{\partial\phi}{\partial x}\right)^2 + \left(\frac{\partial\phi}{\partial y}\right)^2\right] - \varepsilon\left[\frac{\partial\phi}{\partial x}\dot{\phi}_x^0 + \frac{\partial\phi}{\partial y}\dot{\phi}_y^0\right]\right\} dxdy \qquad (A2-10)$$

where ε is the permittivity.

Substitute the Eq. (A2-7) and (A2-9) to Eq. (A2-10), and we can obtain,

$$\Pi(\phi) = \sum_e \iint_{D^e} \left\{ \frac{\varepsilon}{2}\left[\left(\frac{\partial N}{\partial x}\phi^e\right)^2 + \left(\frac{\partial N}{\partial y}\phi^e\right)^2\right] - \varepsilon\left[\phi^{eT}\frac{\partial N}{\partial x}\dot{\phi}_x^0 + \phi^{eT}\frac{\partial N}{\partial y}\dot{\phi}_y^0\right]\right\} |J_a| d\xi d\eta \qquad (A2-11)$$

And, the variable ϕ^e can be transformed from the local to the global coordinate system by ϕ^e=$G\phi$. Hence,

$$\Pi(\phi) = \frac{1}{2}\phi^T \cdot \sum_e \iint_{D^e} \varepsilon \left[G^T \left(\frac{\partial N}{\partial x}\frac{\partial N^T}{\partial x} + \frac{\partial N}{\partial y}\frac{\partial N^T}{\partial y} \right) G \right] |J_a| d\xi d\eta \cdot \phi -$$

$$\phi^T \cdot \sum_e \iint_{D^e} \varepsilon \left[G^T \left(\frac{\partial N}{\partial x}\dot{\phi}_x^0 + \frac{\partial N}{\partial y}\dot{\phi}_y^0 \right) \right] |J_a| d\xi d\eta \qquad (\mathrm{A2}-12)$$

It can be rewritten as:

$$\Pi(\phi) = \frac{1}{2}\phi^T K \phi - \phi^T P \qquad (\mathrm{A2}-13)$$

where,

$$K = \sum_e \iint_{D^e} \varepsilon \left[G^T \left(\frac{\partial N}{\partial x}\frac{\partial N^T}{\partial x} + \frac{\partial N}{\partial y}\frac{\partial N^T}{\partial y} \right) G \right] |J_a| d\xi d\eta \qquad (\mathrm{A2}-14)$$

$$P = \sum_e \iint_{D^e} \varepsilon \left[G^T \left(\frac{\partial N}{\partial x}\dot{\phi}_x^0 + \frac{\partial N}{\partial y}\dot{\phi}_y^0 \right) \right] |J_a| d\xi d\eta \qquad (\mathrm{A2}-15)$$

Solving of the total potential energy of $\Pi(\phi)$ is to find the minimal value of $\Pi(\phi)$. The result (extreme value) exists when the partial derivative of $\Pi(\phi)$ equals 0, as:

$$\delta\Pi(\phi) = 0 \qquad (\mathrm{A2}-16)$$

Finally, we can obtain,

$$K\phi - P = 0 \qquad (\mathrm{A2}-17)$$

Variable *K* and *P* can be obtained from Eq. (A2-14) and (A2-15). For solving the large systems of linear equations of Eq. (A2-17), the conjugate gradient method was used for rapid convergence of the result [3]. After obtaining the electric potential field ϕ, the current field can be calculated by $\boldsymbol{J} = -\sigma_{EC}\nabla\phi$.

2. Thermal field analysis

2.1 Governing equations

The governing equation of the two-dimensional transient heat transfer problem in a control volume at an instant time was presented, which included the energy stored in the control volume, thermal conduction, thermal convection (energy dissipation), and generation of thermal by electric current (Joule heating) [2-4], as shown in the following equations:

$$c\rho_D t_n \frac{\partial T}{\partial t} = -\nabla \cdot \boldsymbol{q} t_n + q_{conv} + q_{gene} t_n \quad (\mathrm{A2}-18)$$

$$\boldsymbol{q} = -k\nabla T \quad (\mathrm{A2}-19)$$

$$q_{conv} = -2h(T - T_0) \quad (\mathrm{A2}-20)$$

$$q_{gene} = \frac{|\boldsymbol{J}|^2}{\sigma_{EC}} \quad (\mathrm{A2}-21)$$

where c, ρ_D, t_n, T, t, $\boldsymbol{q}$, q_{conv}, q_{gene}, k, h, and T_0 are specific heat coefficient (J/kg·K), density (kg/m^3), the thickness of the sample (m), temperature (K), time (s), the flux of thermal conduction (W/m^3), the flux of thermal convection (W/m^2), thermal flux generated by electric current (W/m^3), thermal conductivity coefficient (W/m·K), thermal convection coefficient (W/m^2·K) and initial temperature (K), respectively.

2.2 Boundary conditions

For the thermal conduction problem of this study, the boundary conditions were shown in Fig. A2-3, and the equation was given in Eq. (A2-22).

$$\boldsymbol{q} \cdot \boldsymbol{n}|_{\Gamma_1 \,\&\, \Gamma_2} = q_0 \quad (\mathrm{A2}-22)$$

where q_0 is the heat dissipation due to the electrodes.

And, the initial condition of temperature was shown as,

$$T|_{t=0} = T_0 \quad (\mathrm{A2}-23)$$

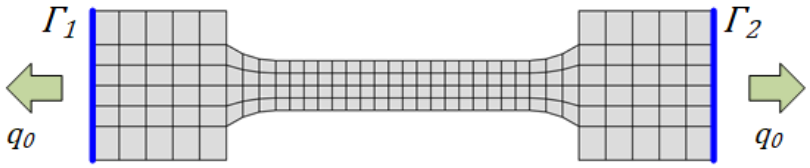

Fig. A2-3 Boundary conditions of thermal field analysis.

2.3 Finite element discretization and variational principle

Similar to the electric analysis in the previous section, the total potential energy of the system containing the boundary conditions was established based on the Galerkin principle [2,3], shown as:

$$\Pi(T) = \iint_D \left\{ \frac{kt_n}{2}\left[\left(\frac{\partial T}{\partial x}\right)^2 + \left(\frac{\partial T}{\partial y}\right)^2\right] + c\rho t_n \frac{\partial T}{\partial t}T + h\left(\frac{1}{2}T - T_0\right)T - \frac{|\boldsymbol{J}|^2}{\sigma_{EC}} t_n T \right\} dxdy \qquad (A2-24)$$

The same shape function Eq. (A2-8) was also used here, and then the variable of T can be expressed, as:

$$T = N_1T_1 + N_2T_2 + N_3T_3 + N_4T_4 = N_iT_i = NT^e \qquad (A2-25)$$

where, $T_1 \sim T_4$ are the temperatures of the 4 nodes of the normalized quadrilateral element.

Hence, the Eq. (A2-24) can be rewritten by substituting the Eq. (A2-7) and (A2-25),

$$\Pi(T) = \sum_e \iint_{D^e} \left\{ \frac{kt_n}{2}\left[\left(\frac{\partial N}{\partial x}T^e\right)^2 + \left(\frac{\partial N}{\partial y}T^e\right)^2\right] + T^{eT}c\rho t_n \frac{\partial T^e}{\partial t}NN^T + \frac{1}{2}h(NT^e)^2 - T^{eT}hT_0N - T^{eT}\frac{|\boldsymbol{J}|^2}{\sigma_{EC}} t_n N \right\} |J_a| d\xi d\eta \qquad (A2-26)$$

And, the T^e can be transformed from the local to the global coordinate system by $T^e = GT$. Hence,

$$\Pi(T) = \frac{1}{2}T^T \cdot \sum_e \iint_{D^e} kt_n G^T \left[\frac{\partial N}{\partial x}\frac{\partial N^T}{\partial x} + \frac{\partial N}{\partial y}\frac{\partial N^T}{\partial y}\right] G|J_a| d\xi d\eta \cdot T + \frac{1}{2}T^T$$
$$\cdot \sum_e \iint_{D^e} hG^T NN^T G|J_a| d\xi d\eta \cdot T + T^T$$
$$\cdot \sum_e \iint_{D^e} G^T c\rho t_n NN^T G|J_a| d\xi d\eta \cdot \frac{\partial T}{\partial t} - T^T \cdot \sum_e \iint_{D^e} hT_0 NG|J_a| d\xi d\eta$$
$$- T^T \cdot \sum_e \iint_{D^e} \frac{|\boldsymbol{J}|^2}{\sigma_{EC}} t_n NG|J_a| d\xi d\eta \qquad (A2-27)$$

The above equation can be rewritten as:

$$\Pi(T) = \frac{1}{2}T^T(K+H)T + T^T\left(C\dot{T} - P_H - P_Q\right) \qquad (A2-28)$$

where,

$$K = \sum_e \iint_{D^e} kt_n G^T \left[\frac{\partial N}{\partial x}\frac{\partial N^T}{\partial x} + \frac{\partial N}{\partial y}\frac{\partial N^T}{\partial y}\right] G|J_a| d\xi d\eta \qquad (A2-29)$$

$$H = \sum_e \iint_{D^e} hG^T NN^T G|J_a| d\xi d\eta \qquad (A2-30)$$

$$C = \sum_e \iint_{D^e} G^T c\rho t_n NN^T G|J_a| d\xi d\eta \qquad (A2-31)$$

$$P_H = \sum_e \iint_{D^e} hT_0 NG|J_a| d\xi d\eta \qquad (A2-32)$$

$$P_Q = \sum_e \iint_{D^e} \frac{|\boldsymbol{J}|^2}{\sigma_{EC}} t_n NG|J_a| d\xi d\eta \qquad (A2-33)$$

Solving of the total potential energy of the system $\Pi(T)$ is to find the minimal value of $\Pi(T)$. The extreme value exists when the partial derivative of $\Pi(T)$ equals 0.

$$\delta\Pi(T) = 0 \qquad (A2-34)$$

Finally, we can obtain,

$$C\dot{T} + (K+H)T - P_H - P_Q = 0 \qquad (A2-35)$$

The matrixes $C, K, H, P_H,$ and P_Q can be obtained from Eq. (A2-29) to (A2-33). For solving this first-order ordinary differential equation, a direct integration method was used with a small enough time-step [3].

3. Stress field analysis

3.1 Governing equations

The governing equation of the thermoelastic problem included the equilibrium equation, geometric equation, and physical equation, which are listed as follows [2,3]:

$$\nabla \cdot \sigma + \boldsymbol{f} = \boldsymbol{0} \qquad (A2-36)$$

$$\boldsymbol{\varepsilon} = \frac{1}{2}(\nabla \boldsymbol{u} + (\nabla \boldsymbol{u})^T) \qquad (A2-37)$$

$$\boldsymbol{\sigma} = D(\boldsymbol{\varepsilon} - \varepsilon_0) \qquad (A2-38)$$

where $\boldsymbol{\sigma}$ is stress (Pa), $\boldsymbol{f}$ surface force (N/m^2), $\boldsymbol{\varepsilon}$ strain, $\boldsymbol{u}$ displacement (m), D elastic constant. ε_0 is the thermal strain, which is given as $\varepsilon_0 = \alpha(T - T_0)[1\ 1\ 0]^T$. where α is thermal expansion coefficient (K^{-1}) and T_0 the initial temperature (K).

3.2 Boundary conditions

The boundary conditions of this stress analysis were nearly the free boundary, as shown in Fig. A2-4, and the equations were given in Eq. (A2-39).

$$\begin{cases} u_x|_A = 0 \\ u_y|_{A\,\&\,B} = 0 \end{cases} \qquad (A2-39)$$

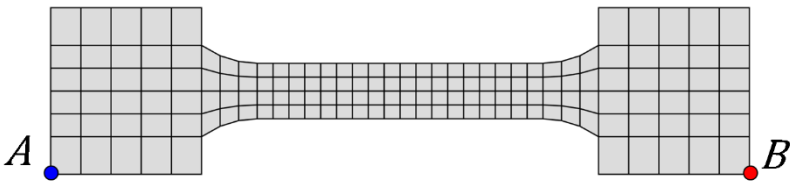

Fig. A2-4 Boundary conditions of stress field analysis.

3.3 Finite element discretization and variational principle

Based on the minimum potential energy principle, we can construct the total potential energy of the system containing the boundary conditions [2,3], shown as:

$$\Pi(\boldsymbol{u}) = \iint_D \frac{1}{2}\boldsymbol{\varepsilon}^T D\boldsymbol{\varepsilon} t_n dxdy - \iint_D \boldsymbol{\varepsilon}^T D\varepsilon_0 t_n dxdy \qquad (\mathrm{A2}-40)$$

The same shape function of Eq. (A2-8) was used in this section, and then the variable of $\boldsymbol{u}$ can be expressed as:

$$\boldsymbol{u} = N_1 u_1 + N_2 u_2 + N_3 u_3 + N_4 u_4 = N_i \boldsymbol{u_i} = N\boldsymbol{u^e} \qquad (\mathrm{A2}-41)$$

where, $u_1 \sim u_4$ are the displacement at the 4 nodes of the normalized quadrilateral element. And,

$$\boldsymbol{\varepsilon} = L\boldsymbol{u} = LN\boldsymbol{u^e} \qquad (\mathrm{A2}-42)$$

where, L is the differential operator, as shown below,

$$L = \begin{bmatrix} \frac{\partial}{\partial x} & 0 \\ 0 & \frac{\partial}{\partial y} \\ \frac{\partial}{\partial y} & \frac{\partial}{\partial x} \end{bmatrix} \qquad (\mathrm{A2}-43)$$

Hence, the total potential energy of the system $\Pi(\boldsymbol{u})$ can be rewritten as

$$\Pi(\boldsymbol{u}) = \sum_{e} \iint_{\boldsymbol{D^e}} \frac{1}{2} \boldsymbol{u^{e}}^{T} (LN)^{T} D (LN) \boldsymbol{u^e} t_n |J_a| d\xi d\eta$$

$$- \sum_{e} \iint_{\boldsymbol{D^e}} \boldsymbol{u^{e}}^{T} (LN)^{T} D \varepsilon_0 t_n |J_a| d\xi d\eta \qquad (\mathrm{A2}-44)$$

where D is the elastic matrix, as shown in the following,

$$D = \frac{E}{1-v^2} \begin{bmatrix} 1 & v & 0 \\ v & 1 & 0 \\ 0 & 0 & \dfrac{1-v}{2} \end{bmatrix} \qquad (\mathrm{A2}-45)$$

where E is elastic modulus (Pa), and v is the Poisson's ratio.

And, the $\boldsymbol{u^e}$ can be transformed from the local to the global coordinate system by $\boldsymbol{u^e} = G\boldsymbol{u}$.

$$\Pi(\boldsymbol{u}) = \frac{1}{2} \boldsymbol{u}^{T} \cdot \sum_{e} \iint_{\boldsymbol{D^e}} G^{T} (LN)^{T} D (LN) G t_n |J_a| d\xi d\eta \cdot \boldsymbol{u} -$$

$$\boldsymbol{u}^{T} \cdot \sum_{e} \iint_{D^e} G^{T} (LN)^{T} D \varepsilon_0 t_n |J_a| d\xi d\eta \qquad (\mathrm{A2}-46)$$

The above equation can be rewritten as:

$$\Pi(\boldsymbol{u}) = \frac{1}{2} \boldsymbol{u}^{T} K \boldsymbol{u} - \boldsymbol{u}^{T} P \qquad (\mathrm{A2}-47)$$

where,

$$K = \sum_{e} \iint_{D^e} G^{T} (LN)^{T} D (LN) G t_n |J_a| d\xi d\eta \qquad (\mathrm{A2}-48)$$

$$P = \sum_{e} \iint_{D^e} G^{T} (LN)^{T} D \varepsilon_0 t_n |J_a| d\xi d\eta \qquad (\mathrm{A2}-49)$$

Solving of the total potential energy of the system $\Pi(\boldsymbol{u})$ is to find the minimal value of $\Pi(\boldsymbol{u})$. The extreme value exists provided that its partial derivative is zero.

$$\delta \Pi(\boldsymbol{u}) = \mathbf{0} \qquad (\mathrm{A2}-50)$$

Finally, we can obtain,

$$K\boldsymbol{u} - P = \mathbf{0} \qquad (\mathrm{A2}-51)$$

Variable K and P can be obtained from Eq. (A2-48) and (A2-49). For solving the large systems of linear equations of Eq. (A2-51), the conjugate gradient method was used for rapid convergence of the solution [3]. After obtaining the field of displacement, the thermal stress can be calculated by $\boldsymbol{\sigma} = D(\boldsymbol{\varepsilon} - \varepsilon_0) = D(L\boldsymbol{u} - \varepsilon_0)$.

4. Procedure and GUI development based on MATLAB

To realize the above calculation, a self-developed finite element procedure was performed based on the commercial software MATLAB. In addition, the GUI interface named Electric Thermal and Mechanics Analysis (ETMA) was presented for easy access. The interface contains Geometry, Mesh, Loading, Boundary conditions, Material properties, Solve, and Post-processing. The basic functions of each part are described below.

4.1 Geometry and Mesh

Fig. A2-5 shows how to build the sample geometry and discretize the FEM model. One can build the model according to the given geometry, and it is also possible to customize the model by loading one's own data. The software offers additional options to accommodate the geometric model with notches, such as U-type, V-type, and self-defined notches. Moreover, V-shaped and self-defined cracks are also available for modeling the cracked geometry.

This interface provided two kinds of elements, triangular elements and quadrilateral elements, to discretize the model. Here need to mention, the meshing method of the triangular element is performed using an open-source procedure MATLAB code

DistMesh [5,6]. The quadrilateral discretization is performed using the author's self-developed procedures with methods of model partitioning and sweeping. The quadrilateral element has higher accuracy than the triangular element, but less flexibility and adaptability. Hence, the author recommends that the regular FEM model without a notch or crack adopt the quadrilateral elements, otherwise using the triangular elements.

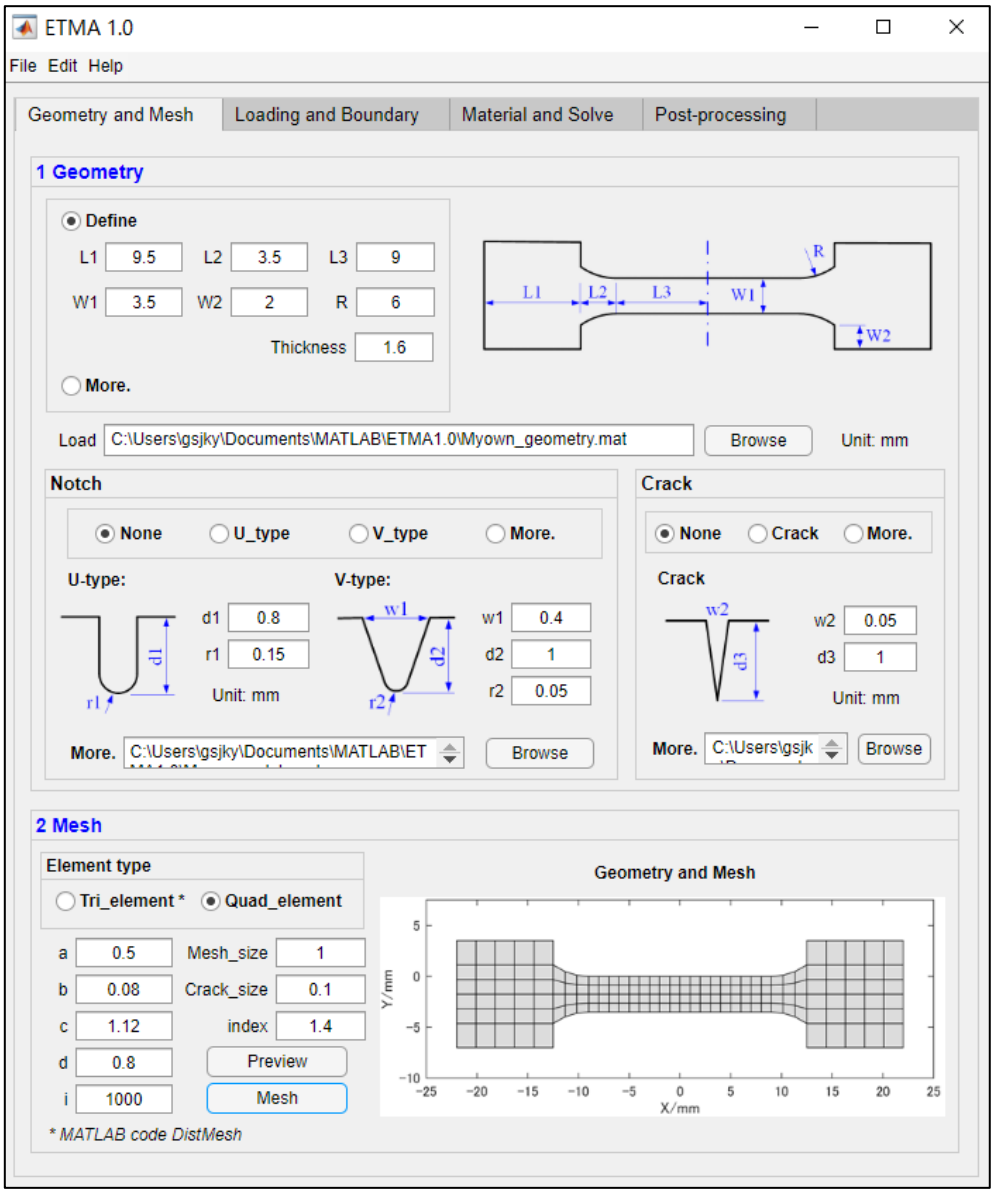

Fig. A2-5 GUI interface of Geometry and Mesh.

4.2 Loading and Boundary conditions

The GUI provides two kinds of current load: pulse-shaped and sine-shaped, as shown in Fig. A2-6. One can adjust the parameters for both types of load, such as current density, duration time, interval time, repeat times, etc. In addition, the self-defined current load is also available. The division of simulation time (heating and cooling) is also provided, and the unequal division is designed to save simulation time on the basis of ensuring the accuracy of the results.

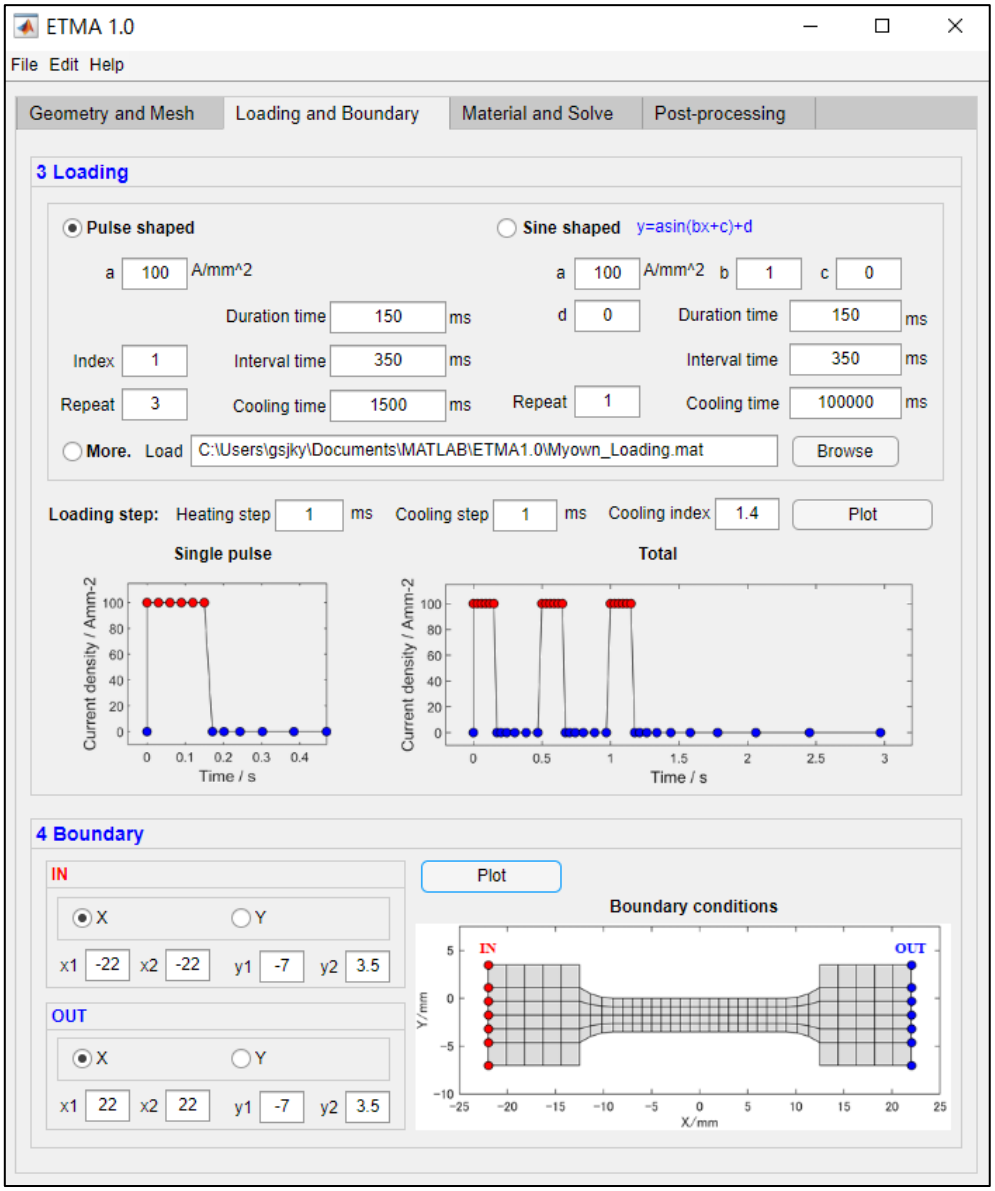

Fig. A2-6 GUI interface of Loading and Boundary.

The Boundary module of this interface provides the functions to set the loading areas and directions of the load. The boundary conditions are imposed on the nodes in this interface, as shown in Fig. A2-6.

4.3 Material properties and Solving

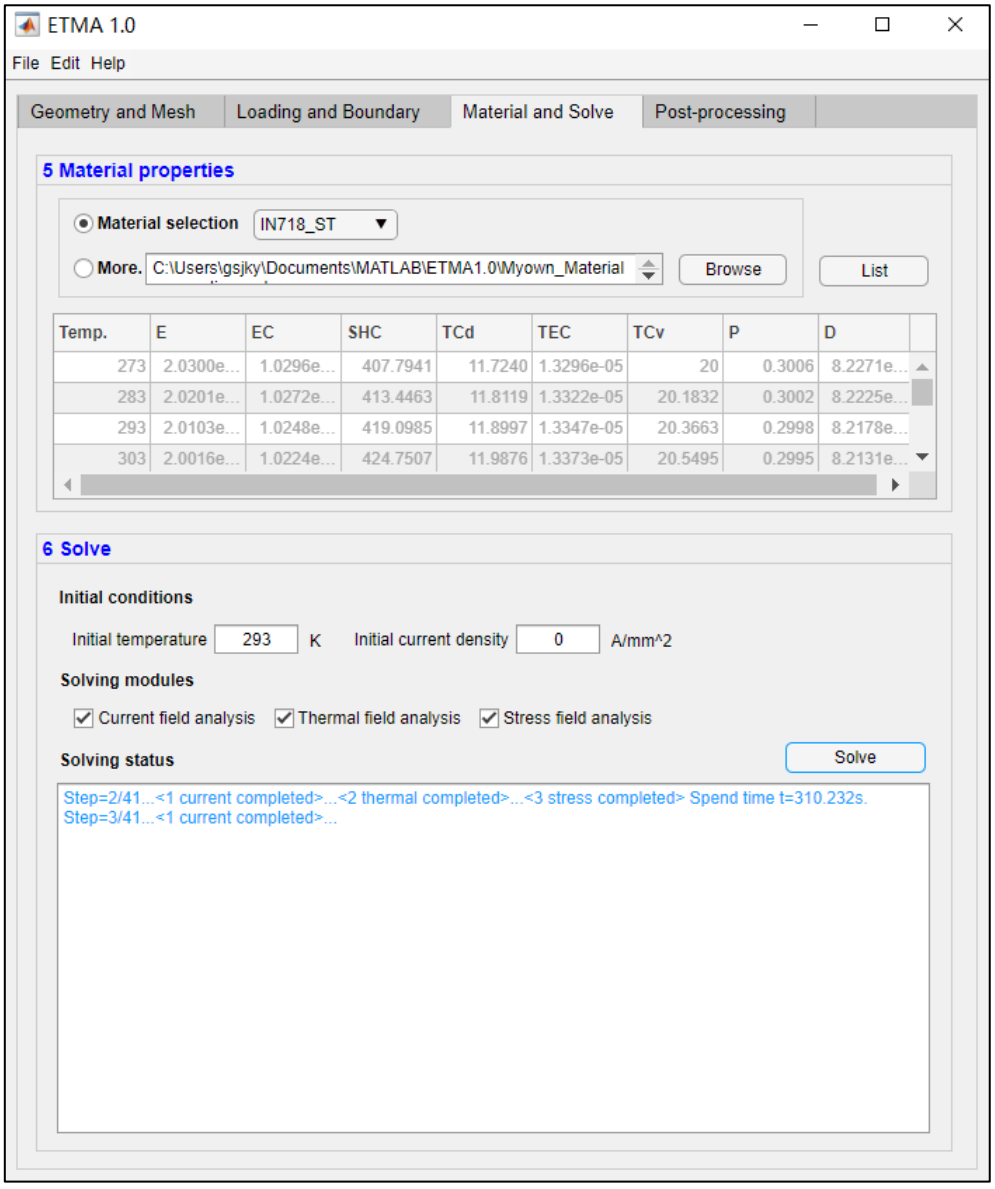

Fig. A2-7 GUI interface of Material properties and Solve.

The temperature-dependent material properties are used in this procedure, as shown in Fig. A2-7. The material properties listed in the table are temperature and the

corresponding material properties (Young's modulus, electrical conductivity, specific heat capacity, thermal conductivity, thermal expansion coefficient, thermal convection, Poisson's ratio, and density). Apart from the built-in material properties, one can also load their own material properties.

The Solve module provides a start button. Before then, one can set the initial conditions and choose the solution field of interest, such as Current field analysis, Thermal field analysis, and Stress field analysis. Once set up, it is ready to start solving. The solution statuses for each load step are displayed in the text box below.

4.4 Post-processing

Fig. A2-8 shows the Post-processing of this interface. Firstly, the geometry of the FEM model is presented again to help the user locate the exact place of interest. Hence, the developer has added the original point A and the auxiliary lines X-X and Y-Y. Moreover, the maximal and minimal points are also marked out.

The time load map is also intended to facilitate the user to quickly identify the load step of interest. The last heating step and the total load steps are also presented. One can select specific load steps or all load steps.

The interface offers three ways to select an area of interest: Node, Line, and Plane. One can select the Node of interest directly by the coordinates or number. For the mode of Line, one can select a line segment within an area or select a line between nodes. The mode of Plane means all the models have been selected. And finally, one can plot the figure by choosing the output of interest, such as the Current field, Temperature field, and Stress field, etc. The example image in Fig. A2-8 shows the temperature field of the model at the time step of 31.

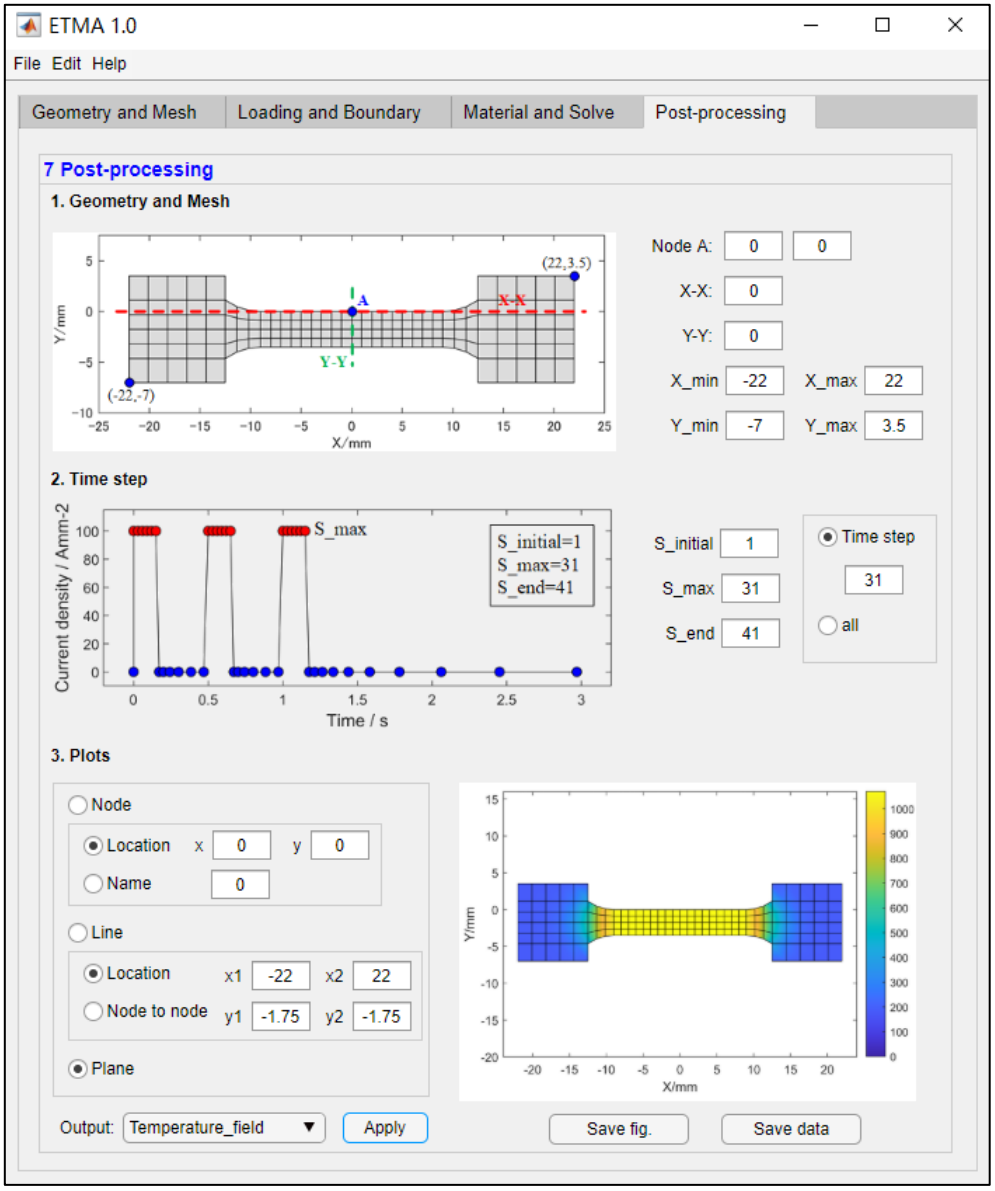

Fig. A2-8 GUI interface of Post-processing.

References

[1] D.K. Cheng, Field and Wave Electromagnetics, Reading, Mass, (1989).

[2] Zienkiewicz, R.L. Taylor, The finite element method, 5th ed, Butterworth-Heinemann, Oxford ; Boston, (2000).

[3] M.C. Wang, Finite Element Method, Tsinghua University Press Ltd., (2003). (in

Chinese)

[4] F.P. Incropera, F.P. Incropera, eds., Fundamentals of heat and mass transfer, 6th ed, John Wiley, Hoboken, NJ, (2007).

[5] P.-O. Persson, G. Strang, A Simple Mesh Generator in MATLAB. SIAM Review, 46 (2) (2004) 329-345.

[6] P.-O. Persson, Mesh Generation for Implicit Geometries. Ph.D. thesis, Department of Mathematics, MIT, (2004).

Appendix 3: One-dimensional transient heat conduction model

To estimate the temperature of the rapidly heated sample, a one-dimensional transient heat conduction model was used, as shown in Fig. A3-1. The thermal circuits, which were commonly used to model heat flow, were also presented. Hence, the equations of heating and cooling with boundary conditions are shown below [1]:

Rapid heating:

$$\begin{cases} \dfrac{T_B - T_A}{\dfrac{L_h}{2k_h} + R''_{t,c} + \dfrac{L_s}{k_s}} + h(T_{sur} - T_A) + \varepsilon\sigma(T_{sur}^4 - T_A^4) = \rho c L_s \dfrac{dT}{dt} \\ T_B|_{t\geq 0} = T_{sur}|_{t\geq 0} = T_{furnace} \\ T_A|_{t=0} = 293 \end{cases} \quad (\mathrm{A3}-1)$$

Air cooling:

$$\begin{cases} \dfrac{T_A - T_B}{\dfrac{L_h}{2k_h} + R''_{t,c} + \dfrac{L_s}{k_s}} + h(T_A - T_{sur}) + \varepsilon\sigma(T_A^4 - T_{sur}^4) = -\rho c L_s \dfrac{dT}{dt} \\ T_B|_{t\geq 0} = T_{sur}|_{t\geq 0} = 293 \\ T_A|_{t=0} = T_{furnace} \end{cases} \quad (\mathrm{A3}-2)$$

where, T_A is the temperature of the sample at the center point of the upper surface, T_B is the temperature of the holder, T_{sur} is the surrounding temperature and $T_{furnace}$ is the temperature of the furnace. L_s and L_h are the thickness of the sample and holder. k_s and k_h are the thermal conductivity of the sample and holder. $R''_{t,c}$ is the resistance of thermal contact. h is the heat convection coefficient of air. ε is a radiative property of the surface termed the emissivity, taken as 0.9 in this study. σ is the Stefan–Boltzmann constant. ρ the density of the material, and c specific heat capacity of the sample. q''_1 and q''_2 are the conductive heat flux of the holder and sample. q''_{conv} is the convective heat flux of air and q''_{rad} is the heat flux of radiation.

For solving the first-order ordinary differential equation of Eq. (A3-1) and (A3-2),

the central differential method [2] was used. To ensure the convergence of the solution, a small-time step of $\Delta t = 0.001s$ was utilized.

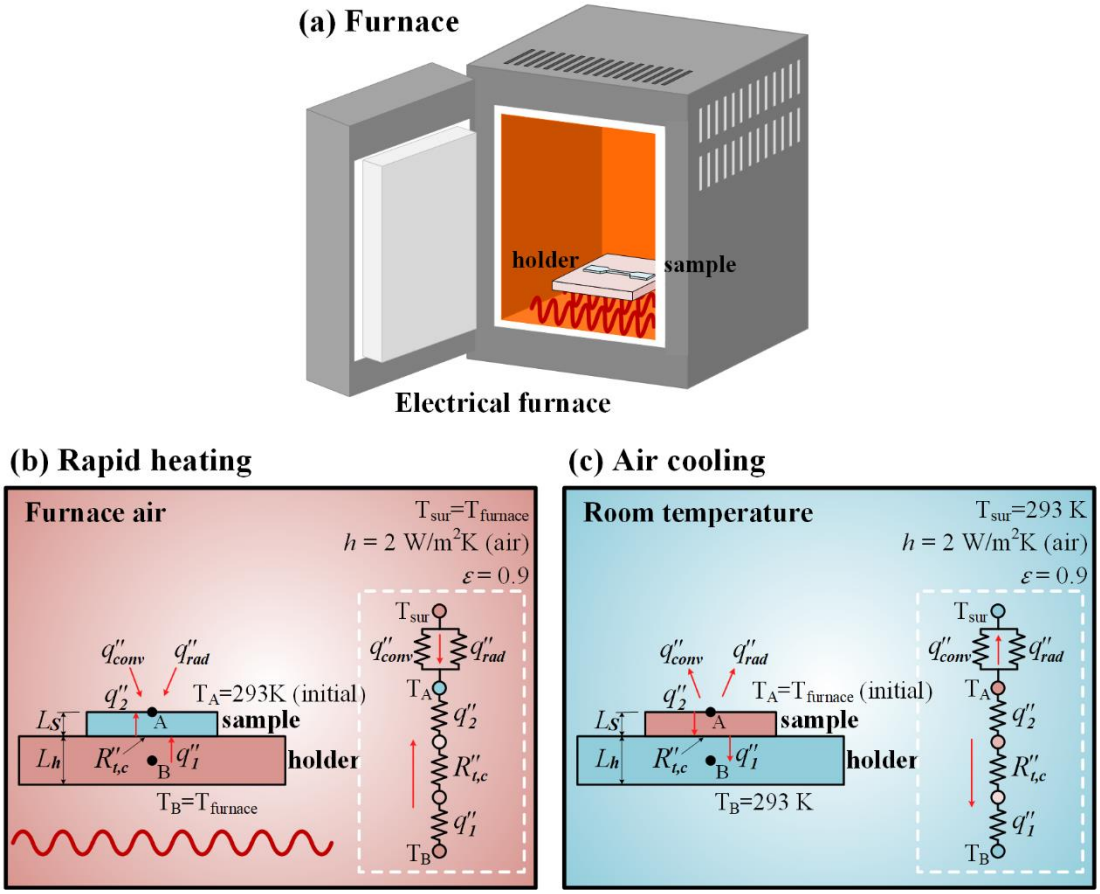

Fig. A3-1. Temperature simulation of the rapidly heated sample. (a) Schematic diagram of the furnace, (b) rapid heating, and (c) air cooling of the sample.

References

[1] F.P. Incropera, F.P. Incropera, eds., Fundamentals of heat and mass transfer, 6th ed, John Wiley, Hoboken, NJ, (2007).

[2] H. Jeffreys, Methods of Mathematical Physics, Third Edition, 3rd ed., Cambridge University Press, Cambridge, U.K. ; New York, (2000).